GSI

Dipl. 2008 - 08
June

Setup of a carbon-cluster laser ion source for high-precision mass spectrometry

Christian Smorra

(Diplomarbeit der Johannes Gutenberg-Universität Mainz)

Gesellschaft für Schwerionenforschung mbH
Planckstraße 1 · D-64291 Darmstadt · Germany
Postfach 11 05 52 · D-64220 Darmstadt · Germany

Setup of a carbon-cluster laser ion source for high-precision mass spectrometry

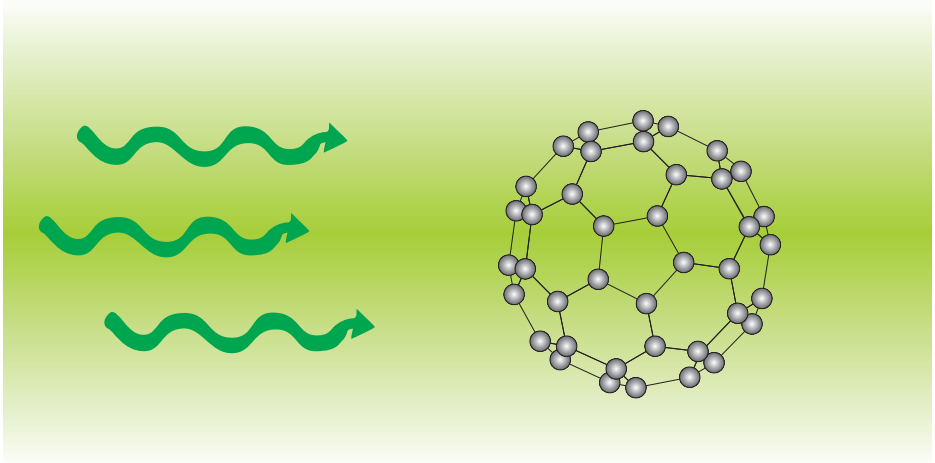

Christian Smorra

Institut für Physik
Johannes Gutenberg-Universität Mainz

Diplomarbeit von

Christian Smorra

Institut für Physik
Johannes Gutenberg-Universität Mainz

Setup of a carbon-cluster laser ion source for high-precision mass spectrometry

22. Januar 2008

Contents

List of Tables

List of Figures

Chapter 1

Introduction

The mass being a fundamental property in nature enters in many fields of science as an important input parameter [Bla06]. The nuclear mass for instance is directly related to the binding energy of the nucleus, as expressed by Einstein's famous equation $E = mc^2$. The binding energy is reflecting all interactions, namely the electromagnetic, the weak and the strong interaction, which can be studied by measuring the mass values.

High-precision mass spectrometry experiments aim for the precise determination of the masses of the about 3200 known nuclides [Aud03]. In Tab. 1.1 different applications and the required relative mass uncertainty $\delta m/m$ are listed. Nowadays the highest precision in mass spectrometry is achieved with stored particles in Penning traps. Mass values are obtained by detection of the cyclotron frequency of the stored ions, which is linked to the mass-to-charge ratio m/q of the ion via the magnetic field B:

$$\nu_c = \frac{1}{2\pi}\frac{qB}{m}. \tag{1.1}$$

Relative uncertainties $\delta m/m$ of 10^{-8} [Bol01, Her03, Kel03] for radioactive nuclides and even down to 10^{-11} [Rai04, Van04, Shi05] for stable isotopes can be reached.

field of application	mass uncertainty
chemistry: identification of molecules	10^{-5}–10^{-6}
nuclear physics: shells, sub-shells, pairing	10^{-6}
nuclear fine structure: deformation, halos	10^{-7}–10^{-8}
astrophysics: r-process, rp-process, waiting points	10^{-7}
nuclear models and formulae: IMME	10^{-7}–10^{-8}
weak interaction studies: CVC hypothesis, CKM unitarity	$\leq 10^{-8}$
atomic physics: binding energies, QED tests	10^{-9}–10^{-11}
metrology: fundamental constants, CPT tests	$\leq 10^{-10}$

Table 1.1: Fields of application and the generally required relative uncertainty on the measured mass $\delta m/m$, which is required to probe the associated physics [Bla06].

The research group MATS (Measurements with Advanced Trapping Systems) at the University of Mainz, Institute of Physics, is involved in four Penning trap

mass spectrometry experiments, three of them are in operation (ISOLTRAP at ISOLDE / CERN [Bla03b, Bla05], Geneva, SHIPTRAP at GSI, Darmstadt [Rah06] and SMILETRAP in Stockholm [Ber02]). The fourth experiment, where the current thesis was carried out on, is presently under construction and located at the research reactor TRIGA Mainz and is named TRIGA-TRAP [Ket06, Fer07]. The aim of the latter experiment is mass measurements on heavy nuclides from uranium to californium and also on neutron-rich fission products produced by the reasearch reactor TRIGA Mainz. Special to this experiment is the use of a non-destructive detection method, i.e. the use of a narrow-band resonance detection technique (narrow-band Fourier-transformation ion-cyclotron-resonance detection Ft-ICR) for the measurement of the cyclotron frequency of the stored ions [Ket06]. Furthermore, the experiment uses a double-trap system within one superconducting magnet: the *purification trap* used for cooling and bunching of the captured ions and the *precision trap* for the actual frequency measurement [Web04, Fer07]. In Chap. 2 of this thesis the basic principles of Penning traps and the mass measurement procedures are discussed in detail.

One challenging part of the mass determination is the measurement of the magnetic field, which has to match the following requirements:

- The precision of the magnetic field measurement has to be at least as precise as the determination of the cyclotron frequency to avoid a limitation of the achieved precision. Thus, a relative uncertainty on a level of 10^{-8} down to 10^{-11} has to be reached, depending on the application. For TRIGA-TRAP a relative uncertainty $\leq 10^{-8}$ has to be reached.

- Since the homogeneous region of the superconducting magnet has typically only a size of 1 cm^3 with a homogeneity of 0.1 ppm, the mass measurement has to be carried out with motional amplitudes of the stored ions as small as possible. Thus, the magnetic field has to be measured at the center of the Penning trap.

- Due to fluctuations and drifts of the field of the superconducting magnet the magnetic field determination is carried out as close as possible in time to the cyclotron frequency measurement of the ion of interest.

The only possiblity to match these requirements is to calibrate the magnetic field by measuring the cyclotron frequency of a reference ion with a well-known mass[1]. Presently, only a few nuclides have been measured with sufficient precision ($\leq 10^{-9}$), only 23 of about 3200 known nuclides [Aud03]. Due to the mass uncertaintly of the reference ion, the obtained results are usually given as cyclotron-frequency ratios:

$$r = \nu_c^{ref}/\nu_c, \tag{1.2}$$

[1]The calibration measurements are usually carried out before and after the determination of the cyclotron frequency of the ion of interest, and the magnetic field at the moment of the measurement is interpolated. In order to monitor the fluctuations of the magnetic field in parallel to the actual measurement a five Penning trap system is under construction [Geo07], where two traps will be used for monitoring the magnetic field with reference ions and three for the measurement procedure itself.

measurements of these kind are therefore called relative mass measurements[2]. The aim of this work is to develope a tool for TRIGA-TRAP to enable absolute mass measurements. This is a laser ion source providing carbon clusters for these calibration purposes. The availablity of carbon clusters, which are molecules of multiple bound carbon atoms, improves also the achieved precision of TRIGA-TRAP, which will be explained in the following.

Since the uncertainty of the calibration mass contributes directly to the uncertainty of the mass of interest, the best choice for a calibration is to use the definition of the atomic mass unit, which is defined as follows:

The unified atomic mass unit (u) is defined to be one twelfth of the mass of an unbound atom of the carbon-12 nuclide, at rest and in its ground state. [Emi95, NIS06]

Thus, if ^{12}C is used as reference mass, the uncertainty of the calibration mass is zero by definition and the mass value of the obtained nuclide is directly measured in atomic mass units [Bla02]. But ^{12}C as the only calibration nuclide is not sufficient, since systematic uncertainties occur in dependence of the reference ions in use [Bol90], which is discussed in detail in Sect. 2.3. The magnitude of these systematic uncertainties increases with the difference between the mass of the ion of interest and the mass of the reference ion (m_{ion} - m_{ref}). Since TRIGA-TRAP aims for the investigations of nuclides up to californium, calibration nuclides are required all over the nuclide chart. To this end carbon clusters are the ideal choice. An ion source for carbon cluster ions provides reference ions in steps of 12 atomic mass units with a negligible uncertainty over the whole nuclear chart. The remaining uncertainty occurs due to the binding energy of the clusters, which is negligible for measurements on radio-nulides on a level of $\delta m/m \approx 10^{-9}$. Thus, the carbon cluster ions allow to achieve higher precision in mass spectrometry experiments by elemination of systematic errors in mass calibration. For this reason, a carbon cluster source has been developed for the TRIGA-TRAP experiment.

In Chap. 3 different kinds of ion sources are discussed. The conclusion is that the most suitable method to produce carbon cluster ions is by ablation with a pulsed laser. Laser ion sources of that kind are already in use for high-precision mass spectrometry at the facilities ISOLTRAP at ISOLDE / CERN [Bla02] and SHIPTRAP at GSI / Darmstadt [Cha07]. The laser ion source for TRIGA-TRAP, which was developed and tested as part of this work, is described in Sect. 3.3.

The setup of the double Penning trap mass spectrometer TRIGA-TRAP is described in detail in Chap. 4. To optimize the ion transport into and from the traps simulation studies have been performed, resulting in optimal voltage settings for the electrodes of the ion optics. Furthermore, simulation studies to identify ion species produced by the laser ion source in a test setup have been performed. The results of these studies are presented in Chap. 5.

In Chap. 6 the preparations of samples for the laser ion source are described. The analysis of the production of carbon cluster ions with different samples concerning the available cluster sizes for calibration purposes are presented. In addition to that, gadolinium samples were investigated, since gadolinium has similar chemical prop-

[2]With the cyclotron-frequency ratio r, the mass of the reference ion m_{ref} and the electron mass m_e, the mass value of the ion of interest m determined by $m = r(m_{ref} - m_e) + m_e$.

erties as californium, which is one of the nuclides of interest for mass measurements at the TRIGA-TRAP mass spectrometer.

Chapter 2

Penning trap mass spectrometry

Penning traps are the tools of choice for high-precision mass measurements [Bla06]. To understand the measurement procedure, first the basic principles of a Penning trap are discussed. Afterwards two different methods of obtaining a mass value m, namely the time-of-flight ion-cyclotron-resonance (TOF-ICR) detection technique and the Fourier-transformation ion-cyclotron resonance (FT-ICR) detection technique, are presented. Finally, the importance of mass calibration for such an experiment will be explained and how the mass calibration can be done.

2.1 Principles of Penning traps

A charged particle of mass m and charge q in a homogenous magnetic field with strength $\vec{B} = B\hat{e}_z$ experiences a Lorentz-force. Thereby it is forced to a circulating motion: in the plane perpendicular to the magnetic field, the particle moves on a circular orbit with the cyclotron frequency (see Eq. 1.1). The motion parallel to the magnetic field is not affected. Thus, by using a magnetic field, a particle can be "confined" in two dimensions. To obtain a confinement of a charged particle in all three dimensions, the so called Penning-trap configuration is used, which superposes a strong magnetic field with an additional weak quadrupolar electrostatic field for axial confinement. The trap is named after F.M. Penning, who published his work on increasing the sensitivity of vacuum gauges by using an axial magnetic field perpedicular to the momentum of the charged particles in the 1930s [Pen36]. For his important experiments with the Penning trap Hans Dehmelt was rewarded the Nobel prize in physics in 1989 [Deh90], together with Wolfgang Paul for the Paul trap [Pau90].

The quadrupolar electric field is created by hyperbolically shaped electrodes, two endcaps and a ring electrode. In the ideal case their surfaces match the following equation:

$$\frac{r^2}{r_0^2} - \frac{z^2}{z_0^2} = \pm 1, \tag{2.1}$$

where r_0 is the inner radius of the ring electrode and z_0 is half of the distance between the two endcaps (see Fig. 2.1(a)). For positively charged ions a positive potential V_0 is applied to the endcaps in respect to the ring electrode, to add a force

in axial direction, which drives the particles back to the trap center. Thereby the electrostatic potential is given by:

$$\phi(x, y, z) = \frac{V_0}{d^2}(z^2 - \frac{x^2 + y^2}{2}), \tag{2.2}$$

where

$$d^2 = z_0^2 + \frac{1}{2}r_0^2 \tag{2.3}$$

is a characteristic trap dimension. Nowadays two types of Penning traps are in use, hyperbolical and cylindrical traps, see Fig. 2.1.

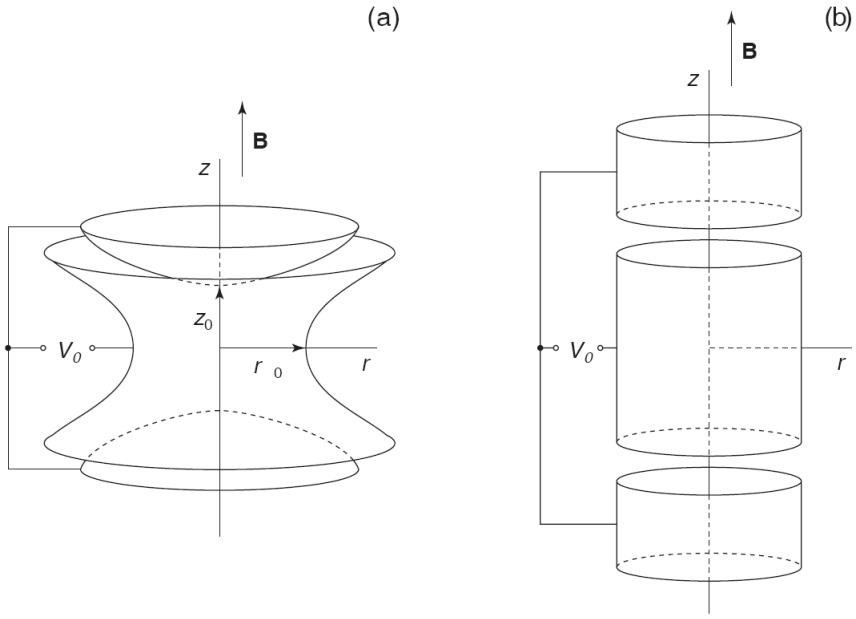

Figure 2.1: Penning trap electrode configuration for a hyperbolic trap (a) and a cylindrical trap (b). Both consist of a ring electrode in the center and two endcaps. To confine positivly charged particles, additionally to the magetic field a positive voltage is applied to the endcaps in respect to the ring electrode.

Since the electrodes in a real Penning trap cannot fullfil Eq. (2.1) due to finite trap dimensions, holes for injection and ejection of particles, slits for the segmentation of the electrodes, and possible misalignments, a Penning trap usually has correction electrodes to maintain a potential which is as close as possible to the quadrupolar potential created by the ideal hyperbolic electrodes.

The motion of a charged particle inside a Penning trap is discussed in detail in [Bro86] and [Gho95]. The particle experiences an electric force, due to the potential given in Eq. (2.2), and a magnetic force from the magnetic field $\vec{B} = B\hat{e}_z$, which can be obtained from the following vector potential:

$$\vec{A}(\vec{r}) = \frac{1}{2}\vec{B} \times \vec{r}. \tag{2.4}$$

The equations of motion are derived by the Euler-Lagrange equations from the Lagrange function. For a time-independent magnetic and electric field the Lagrange function is given by:

$$L(\vec{r},\dot{\vec{r}}) = \frac{m}{2}\dot{\vec{r}}^2 + \frac{q}{c}\dot{\vec{r}}\cdot\vec{A} - q\phi. \tag{2.5}$$

The potentials in Eq. (2.2) and (2.4) lead to the following expression:

$$L(x,y,z,\dot{x},\dot{y},\dot{z}) = \frac{m}{2}(\dot{x}^2+\dot{y}^2+\dot{z}^2) + \frac{q\,B}{2\,c}(x\dot{y}-y\dot{x}) - \frac{qU}{d^2}(2z^2-x^2-y^2). \tag{2.6}$$

Applying the Euler-Lagrange equations, one obtains:

$$\ddot{x} = \omega_c\dot{y} + \frac{1}{2}\omega_z^2 x \tag{2.7}$$

$$\ddot{y} = -\omega_c\dot{x} + \frac{1}{2}\omega_z^2 y \tag{2.8}$$

$$\ddot{z} = -\omega_z^2 z, \tag{2.9}$$

where $\omega_c = 2\pi\nu_c$ is the cyclotron frequency already given in Eq. (1.1) and ω_z is the axial frequency:

$$\omega_z = \sqrt{\frac{qU}{md^2}}. \tag{2.10}$$

Since the equations of the x- and y-component are coupled, we define $u = x + iy$. The equation for u can be solved with the ansatz $u = e^{-i\omega t}$, leading to the following solutions for ω:

$$\omega_+ = \frac{\omega_c}{2} + \sqrt{\frac{\omega_c^2}{4} - \frac{\omega_z^2}{2}} \tag{2.11}$$

$$\omega_- = \frac{\omega_c}{2} - \sqrt{\frac{\omega_c^2}{4} - \frac{\omega_z^2}{2}}. \tag{2.12}$$

ω_+ is called the reduced cyclotron frequency and ω_- the magnetron frequency. If the particle shall be trapped, the condition $\frac{\omega_c^2}{4} > \frac{\omega_z^2}{2}$ has to be fullfiled, or expressed in terms of the magnetic and electric field:

$$B > \sqrt{\frac{2mU}{qd^2}}. \tag{2.13}$$

The motion of the trapped particle is a superposition of three independent oscillations inside the trap: One oscillation mode in z-direction between the two endcaps with the eigenfrequency ω_z, and two in the radial plane: the slow oscillating magnetron motion with eigenfrequency ω_-, and the fast oscillating modified cyclotron

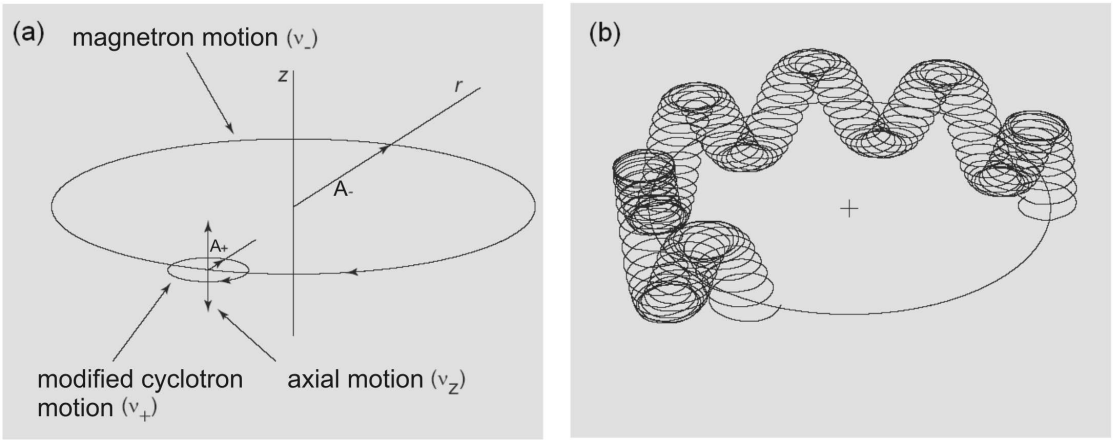

Figure 2.2: Ion motion inside a Penning trap. The motion is a superposition of three eigenmotions: the magnetron, the modified cyclotron, and the axial motion (a). Superposition of all three eigenmotions leads to a trajectory as shown in (b).

motion with the eigenfrequency ω_+. Fig. 2.2 illustrates the motional modes of a trapped particle.

For the magnitude of these eigenfrequencies the following rule applies:

$$\omega_c \approx \omega_+ > \omega_z > \omega_-. \tag{2.14}$$

The diffence is thereby several orders of magnitude. As an example, for a singly-charged caesium ion ($m = 133$ u) in a trap with $d = 26.8$ mm, $B = 7$ T and $U = 20$ V: $\omega_+ = 802.9$ kHz, $\omega_z = 31.90$ kHz, $\omega_- = 633.6$ Hz. Futhermore, the following relations exist for the eigenfrequencies, which will be of interest later, when the mass measurement procedures are discussed:

$$\omega_c = \omega_+ + \omega_- \tag{2.15}$$

$$\omega_c^2 = \omega_+^2 + \omega_z^2 + \omega_-^2 \tag{2.16}$$

$$\omega_- \approx \frac{U}{2d^2B}. \tag{2.17}$$

The first equation will be of interest for the coupling of the magnetron and modified cyclotron motion, the second is known as the invariance thoerem [Bro86], since this equation is also valid for a Penning trap with imperfections, e.g. where the magnetic field is tilted against the trap axis and a misalignment of the electrodes contributes to a quadrupolar potential [Bro82]. The last equation is obtained by a serial expansion of Eq. (2.12), taking Eq. (2.14) into account. Thus, the magnetron frequency is in first order independent from the mass of the particle.

As a next step, the contribution of these eigenmotions to the total energy of the system will be investigated. Therefore the Hamilton function of the system is calculated with the canonical momentum $p_i = \frac{dL}{d\dot{x}_i}$:

$$H = \frac{1}{2m}(p_x^2 + p_y^2 + p_z^2) - \frac{\omega_c}{2}(xp_y - yp_x) + \frac{\omega_1^2}{2}(x^2 + y^2) + \frac{1}{2}m\omega_z^2 z^2,$$

where $\omega_1 = \sqrt{\frac{\omega_c^2}{4} - \frac{\omega_z^2}{2}}$. The Hamiltonian contains cross terms. To simplify, the following canonical transformation can be applied:

$$q_\pm = \frac{1}{\sqrt{2}}(Cx \mp \frac{p_y}{C}) \tag{2.18}$$

$$p_\pm = \frac{1}{\sqrt{2}}(\pm Cy + \frac{p_x}{C}) \tag{2.19}$$

$$q_z = Dz,\ \tilde{p}_z = \frac{p_z}{D} \tag{2.20}$$

where $C = \sqrt{m\omega_1}$ and $D = \sqrt{m\omega_z}$. Applying this transformation one obtains:

$$H = \frac{1}{2}\omega_+(p_+^2 + q_+^2) - \frac{1}{2}\omega_-(p_-^2 + q_-^2) + \frac{1}{2}\omega_z(\tilde{p}_z^2 + q_z^2). \tag{2.21}$$

Now, the Hamiltonian is similar to one of the three uncoupled harmonic oscillators, except that the contribution by the magnetron motion to the energy of the system is negative. An increase of the magnetron radius lowers the energy of the system, so that the particle will hit the electrodes after a certain time. The time scale for this process is fortunately large enough to perform experiments on stored ions for several days in a good vacuum [Gho95]. Therefore this system can be called metastable.

2.2 Mass measurement procedure

The mass measurement procedure at TRIGA-TRAP consists of the following steps:

- An ion bunch is delivered from an ion source, containing typically multiple nuclides.
- This bunch is captured in the purification trap, where it is cooled with the mass-selective buffer-gas cooling technique [Sav91]. Thereby unwanted nuclides are removed and the ions of interest are transfered into the precision trap.
- The mass of the ion can be measured with two different techniques in the precision trap: the destructive time-of-flight ion-cyclotron-resonance (TOF-ICR) technique [Gra80, Koe95] or the non-destructive Fourier-transformation ion-cyclotron resonance (FT-ICR) method.

Both of these detection procedures require an excitation of the stored ions by irradiation of a radio-frequency(rf) field. In this section, the ion excitation, the buffer-gas cooling, and finally the TOF-ICR and FT-ICR techniques are discussed.

2.2.1 Excitation of the ion motion

By irradiation with an rf-field, the eigenmotions of the stored ions can be manipulated. Therefore, the ring electrode of the traps are four-fold segmented. This allows an application of a dipolar excitation, for manipulating the amplitude of a single eigenmotion, as well as a quadrupolar excitation, which couples two eigenmotions.

For a dipolar excitation (see Fig. 2.3(a)) [Bla03b], the x-component of the driving field is given in Eq. (2.22), and applied to two opposing segments with a phase shift of 180°.

$$E_x(x, y, z, t) = \frac{U_d}{a} \cos(\Omega_d t + \varphi_d), \tag{2.22}$$

where U_d is the amplitude of the rf-signal, measured on a circle with radius a, and Ω_d the frequency of the excitation signal. If Ω_d matches an eigenfrequency of the stored ions, the amplitude of this eigenmotion can be increased.

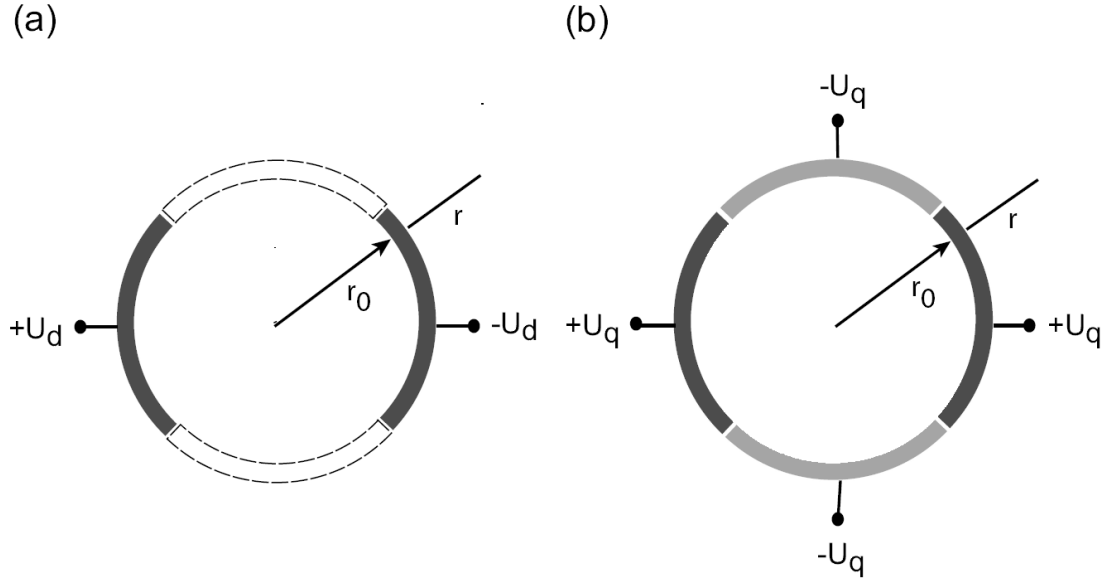

Figure 2.3: Illustration of the electrode configuration for a dipolar and a quadrupolar excitation with an amplitude U_d and U_q, respectively. For a dipolar excitation (a) a rf-field is applied to two ring electrode segments opposite to each other with a phase shift of 180°. For a quadrupolar excitation (b) the rf-field is applied to all four ring electrode segments, where the pase shift between to neighbouring electrodes is 180°.

A quadrupolar excitation is required for the buffer-gas cooling (Sect. 2.2.2) and the TOF-ICR detection (Sect. 2.2.3). With this kind of excitation the magnetron and the modified cyclotron frequency can be coupled, meaning that during the irradition the amplitudes of these two eigenmotions are converted periodically into each other [Bol90]. Therefore, the frequency of the excitation signal has to match the sum of the two eigenfrequencies, which is in that case ω_c (see Eq. 2.15). The x- and y-components of the irradiated electric field are given by the following equations:

$$E_x(x, y, z, t) = \frac{2U_q}{a^2} \cos(\Omega_q t + \varphi_q) y \tag{2.23}$$

$$E_y(x,y,z,t) = -\frac{2U_q}{a^2}\cos(\Omega_q t + \varphi_q)x \tag{2.24}$$

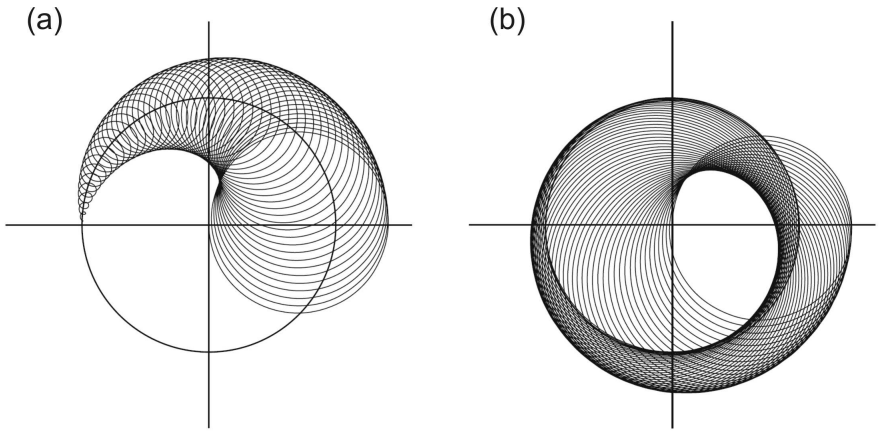

Figure 2.4: Simulation of the conversion of the magnetron motion into the modified cyclotron motion by quadrupolar excitation with the cyclotron frequency $\omega_c = \omega_+ + \omega_-$. (a) shows the first part of the conversion. The initial magnetron radius is depicted, and the cross marks the center of the trap. (b) shows the further development to a full conversion.

A full conversion of the magnetron into the modified cyclotron motion is illustrated in Fig. 2.4. The time for a complete conversion is expressed by [Bol90]:

$$T_{conv} = \pi\frac{m}{q}\frac{a^2}{2U_q}(\omega_+ - \omega_-) \approx \pi\frac{a^2}{2U_q}. \tag{2.25}$$

The radial energy $E_r \propto r_+^2\omega_+^2 - r_-^2\omega_-^2$ is changed with a period of $2T_{conv}$, leading to a maximum, if the motion is completely converted into the cyclotron motion, and a minimum, in case of a pure magnetron motion. This will be especially of importance for the TOF-ICR measurement (Sect. 2.2.3).

2.2.2 Buffer-gas cooling and cleaning

An ion source usually produces a variation of different nuclides for a mass measurement experiment, especially when it is connected to an on-line radioactive beam facility. Since only one species at a time is wanted for a high-precision mass measurement, a mass-selective cooling technique has to be applied. To decrease the number of impurities and also to reduce the energy distribution and location of the ions, buffer-gas cooling is performed in the purification trap. A gas of low atomic mass number, usually helium, is leaked into the trap. Due to collisions with the buffer-gas, a damping force to the ions results:

$$\vec{F} = -\delta m\vec{v}, \tag{2.26}$$

where $m\vec{v}$ is the momentum of the ion and δ a damping constant:

$$\delta = \frac{q}{m}\frac{1}{K_{ion}}\frac{p/p_N}{T/T_N}. \tag{2.27}$$

K_{ion} is the reduced ion mobility, p the pressure and T the temperature of the buffer-gas in units of the normal pressure p_N and normal temperature T_N. The damping force cools all three eigenmotions of the ions, which decreases the amplitude of axial and modified cyclotron motion, but increases the amplitude of the magnetron motion, since the ions with larger magnetron radius have less energy, as discussed above. Therefore, all ions will be lost after a certain time. However, the increase in magnetron radius is typically orders of magnitude slower than the decrease in cyclotron radius. To avoid losing the ions of interest, the magnetron motion can thus be coupled to the modified cyclotron motion by applying a quadrupolar radio-frequency excitation (see Chap. 2.2.1) with the cyclotron frequency given in Eq. (1.1) [Sav91]. Since the cyclotron frequency depends on the q/m-value of the ion, the coupling is mass dependent. Thus, only for the resonant ion species a coupling between the magnetron and the modified cyclotron motion is achieved. This results in a decrease of the amplitudes of both eigenmotions (see Fig. 2.5). The ions are then isobarically purified, cooled and centered in the trap. Finally this bunch of ions is ejected and transported to the precision trap where a mass measurement can be performed.

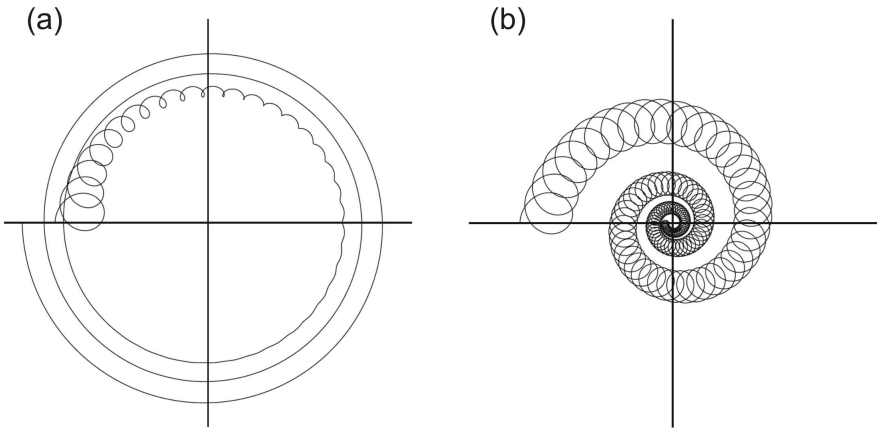

Figure 2.5: Simulations of the orbit for a buffer-gas cooled ion. In (a) without and in (b) with resonant quadrupolar excitation at ω_c. As (a) illustrates, the buffer-gas increases the magnetron radius much slower than the cyclotron radius decreases. If the excitation is applied, the magnetron motion is converted into the cyclotron motion, and therefore both amplitudes are decreasing, as shown in (b).

2.2.3 Destructive TOF-ICR detection

Since frequencies are the physical values which can be measured with highest precision, the mass of an ion is determined by measuring the cyclotron frequency. One way to measure the cyclotron frequency is the destructive time-of-flight ion-cyclotron resonance (TOF-ICR) method. Destructive means that an ion can be used only for a single measurement, after which it is no longer stored in the trap.

The measurement cycle is as follows: at first the cooled ions are excited in the trap by applying a phase-locked dipolar rf-field with the magnetron frequency for

a certain time, so that all ions are located on the same magnetron radius in the trap performing a coherent motion [Bla03b]. Afterwards a quadrupolar excitation with the cyclotron frequency is applied, thereby converting the magnetron motion into the modified cyclotron motion, which increases the radial energy by orders of magnitude (see discussion above and Eq. (2.14)). If the duration T_{rf} and amplitude U_{rf} of the excitation are correct, the conversion of one eigenmotion into the other is complete, but only if the excitation frequency matches ν_c. In that case, the gain of radial energy is maximal.

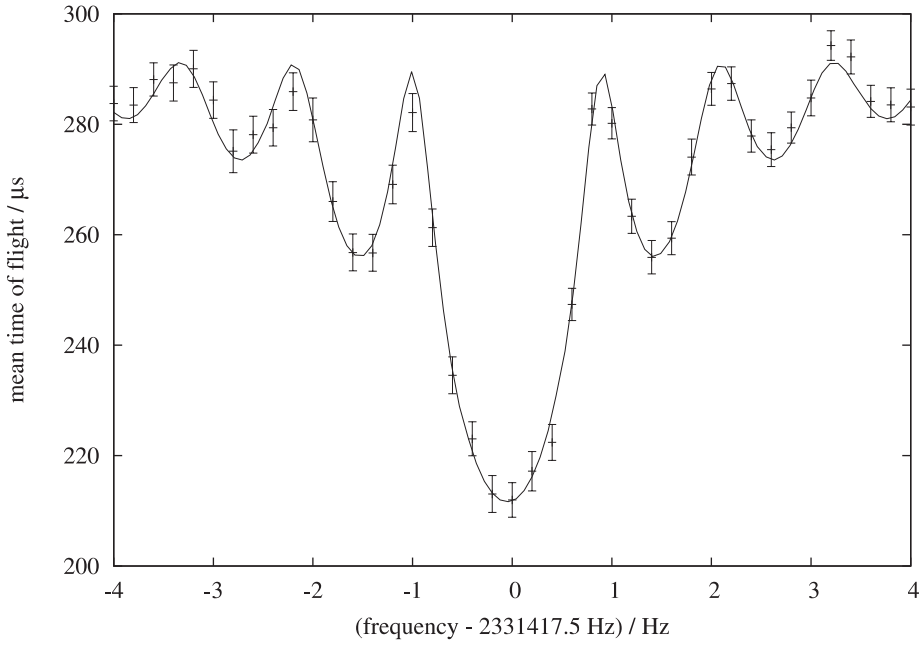

Figure 2.6: A TOF-ICR resonance of $^{85}Rb^{+}$ with an excitation time of 900 ms taken at ISOLTRAP / CERN. The time of flight is plotted as a function of the detuning of the excitation frequency from the cyclotron frequency of $^{85}Rb^{+}$. The shortest time of flight is achieved in case the excitation frequency matches the cyclotron frequency.

The ions are ejected afterwards from the precision trap towards a particle detector. During their drift to the detector the ions encounter a strong magnetic field gradient in the fringe field region of the superconduction magnet. The field gradient converts the radial kinetic energy into axial energy, causing the ions with the highest radial energy to reach the detector faster than all other ions. Comparing the time-of-flight values for different excitation frequencies results in a TOF-ICR resonance as shown in Fig. 2.6 for the case of $^{85}Rb^{+}$ ions. The cyclotron frequency can be obtained by fitting the theoretical line-shape to the data points, which is well understood [Koe95]. The precision of the determination of ν_c is determined by the width of the obtained resonance $\Delta\nu \approx 1/T_{rf}$, where T_{rf} is the exciation time.

The last remaining parameter to obtain a mass or a q/m value is the magnetic field strength B. To achieve the highest possible precision, the magnetic field strength has to be known at least as precise as the obtained cyclotron frequency, which requires a relative precision in the order of 10^{-8} to 10^{-11} [Bla06], depending on the nuclide of interest and the field of application. How the determination of B

is done will be discussed in section 2.3.

2.2.4 Non-destructive FT-ICR detection

The FT-ICR detection is based on the detection of the image current induced by a circulating charge in the ring electrode segments of a Penning trap. This method is called non-destructive, because a particle remains inside the Penning trap during a measurement. Therefore an ion can be used for multiple measurement cycles. The time in which the ion is accessible for a mass measurement is only limited by the storage time and by the lifetime of the nuclide of interest. The number of ions required for a mass determination of a nuclide with good statistics is therefore much smaller than for the destructive TOF-ICR technique, which is an advantage for the investigation of nuclides with low production yields and rather long half-lives, as e.g. for heavy and superheavy elements.

The induced current can be calculated by assuming an oscillating ion between two detection electrodes, which are approximated by infinite plates perdendicular to the ion motion with distance d. If these plates are connected via an external circuit, the power $P = Ui(t)$ induced into the circuit can be expressed by $q\vec{v}\vec{E}$, and therefore [Sch91]:

$$i(t) = \frac{2\pi q \nu_{ion}}{d} r_{ion}(t). \tag{2.28}$$

The current can be converted into a voltage drop with an external circuit. Here, different approaches are possible.

For the analysis of an ion cloud with multiple ions, a broad-band FT-ICR detection is possible, since the current of a large ion ensemble is sufficient to be detected with conventional amplifiers. Therefore the ions have to be excited to a coherent motion, using a dipolar excitation of the eigenfrequency of the motion of interest. Thereby the induced current is also increased, since the amplitude of this eigenmotion also increases (see Eq. (2.28)). Then the induced current can be amplified and converted via Fourier transformation from time into frequency space.

Single ion detection requires a different approach. Since the induced current is in the order of 100 fA or less, a large and noise free amplification of the signal is necessary. For a tuned circuit the resistance has a sharp maximum at the resonance frequency ω. In resonance the resistance can be expressed by $R = \frac{Q}{\omega C}$, where Q is the quality factor of the resonance circuit and C the associated capacity. The voltage drop from the induced current has its maximum, in case the circuit is in resonance with the ion motion, and it can be expressed by:

$$U_{signal} = RI_{eff} = \frac{1}{\sqrt{2}} \frac{r_{ion}}{D} q \frac{Q}{C}, \tag{2.29}$$

where D is the effective electrode distance (modified since hyperbolic electrodes are used). This signal has to be significantly larger than the thermal noise:

$$U_{noise} = \sqrt{4 k_B T R \Delta\nu}. \tag{2.30}$$

k_B is the Boltzmann constant, T the temperature of the detection system, R the resistance in resonance, and $\Delta\nu$ is the spectral band-width. The signal-to-noise ratio can therefore be expressed as:

$$\frac{S}{N} = \frac{\sqrt{\pi}}{2}\frac{r_{ion}}{D}q\sqrt{\frac{\Delta\nu}{\nu}}\sqrt{\frac{Q}{k_B T C}}. \tag{2.31}$$

To optimize the signal-to-noise ratio, a circuit with a large Q-value is required and the detection system can be cooled down to cryogenic temperatures (4 K) to reduce the thermal noise.

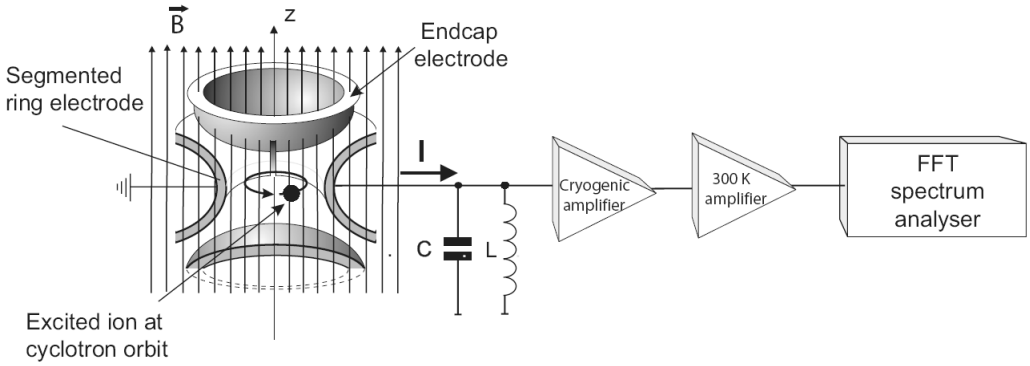

Figure 2.7: Detection scheme for the non-destructive FT-ICR detection. A tuned circuit with a high Q-value is used to increase the signal-to-noise ration. The signal is amplified before it is analysed by an FFT spectrum analyser.

A measurement cycle consists of the following steps: The ions are captured in the Penning trap. A dipolar excitation (see Sect. 2.2.1) is applied to increase the amplitude of the eigenmotion, which should be detected. The induced signal is amplified and read out by a FFT spectrum analyser (see Fig. 2.7 for a typical detection scheme) to obtain the frequency of the ion motion. Since energy is dissipated due to the resistance of the connected ciruit, the amplitude of the ions will decrease again until the ions are centered in the trap (this process is also known as resistive cooling). Then the ions can be excited again and the detection procedure can be repeated in case the ion remains trapped.

Thus, the three eigenfrequencies ν_+, ν_- and ν_z are accessible via this method. To obtain a mass value, the invariance theorem given in Eq. (2.16) can be used to calculate the true cyclotron frequency. The precision of the frequency determination is limited by the recording time T_r, the line width is determined by the Fourier limit: $\Delta\nu \approx 1/T_r$.

Nevertheless, both approaches (TOF- and FT-ICR) require that the magnetic field strength B is known with high precision. In case of the FT-ICR measurement in the TRIGA-TRAP setup, only ν_+ is determined to obtain the mass value of the stored ions. Therefore, even the trapping potential U and the characteristic trap dimension d have to be known with high precision. Thus, these parameters have to be obtained by a mass calibration with a well-known reference mass, which is discussed in the following section.

2.3 Mass calibration

As previously discussed, the TOF-ICR and the FT-ICR mass measurement methods both require a high-precision determination of the magnetic field strength, if possible much better than the obtained value for ν_c or ν_+. Ideally this has to be done simultaneously to the frequency measurement since the superconducting magnet, providing the magnetic field for the Penning traps, underlies field fluctuations and drifts. These are either caused by external conditions like temperature or pressure variations in the experimental hall, or internal limitations since the current is slightly decreasing in the superconducting coils due to the flux-creep phenomenon [And62, And64]. The latter are depending on the magnet in use in the order of $\frac{\delta B}{B}\frac{1}{\delta T} = -10^{-8}$ h^{-1} to -10^{-8} h^{-1} [Ber02, Kel03].

Thus, the only way to measure the magnetic field, without making large systematic errors, is to calibrate the frequency measurements with nuclides with a well-known mass as reference ions inside the precision trap. Usually, the magnetic field is calibrated directly before and after a mass measurement, so that the field strength is extrapolated to the moment of the measurement of the ion of interest. Furthermore, it would be of advantage, if the reference ion moves on the same orbit as the ion of interest, since these two ions experience then the same magnetic field during a measurement, because the region, where the field is homogenouos, is quite small. In the case of TRIGA-TRAP, a homogeneity of 0.1 ppm is reached within 1 cm^3 in the center of the precision trap. Thus, reference ions with a mass as close as possible to the ions of interest are favored.

For the TOF-ICR method, the mass value of the ion of interest m_{ion} is obtained by calibration with one kind of reference ions. With m_{ref} as mass, q_{ref} as charge and $\nu_{c,ref}$ as cyclotron frequency of the reference ion, m_{ion} can be expressed as:

$$m_{ion} = \frac{\nu_{c,ref}}{\nu_{c,ion}}\frac{q_{ion}}{q_{ref}}m_{ref}. \tag{2.32}$$

For the FT-ICR detection of ν_+ two reference masses are required, since two parameters need to be calibrated. From Eq. (2.11) the following equation can be obtained for the mass value, in case ν_+ is of relevance:

$$m_{ion} = q_{ion}\frac{\nu_+ a + b}{\nu_+^2}, \tag{2.33}$$

where the parameter a depends on the magentic field strength B, and b on the trap potential V_0 and the trap dimensions d:

$$a = \frac{B}{2\pi} \tag{2.34}$$

$$b = \frac{V_0}{8\pi^2 d^2}. \tag{2.35}$$

Using two reference ions, m_{ion} can be expressed by the masses, m_1 and m_2, and the reduced cyclotron frequencies, $\nu_{+,1}$ and $\nu_{+,2}$, of the reference ions, where the indicies

"1" and "2" label the first and the second reference ion. To simplify the result, the same charge state is assumed for all ions. From Eq. (2.33), the mass value is then given by:

$$m_{ion} = \frac{\nu_{+,1}^2(\nu_{+,ion} - \nu_{+,2})}{\nu_{+,ion}^2(\nu_{+,1} - \nu_{+,2})} m_1 + \frac{\nu_{+,2}^2(\nu_{+,1} - \nu_{+,ion})}{\nu_{+,ion}^2(\nu_{+,1} - \nu_{+,2})} m_2. \tag{2.36}$$

Nuclide	A	m / μu	δm / μu	δm / m / ppb
^{1}n	1	1008664.91574	0.0006	0.5552
^{1}H	1	1007825.03207	0.0001	0.0992
^{2}H	2	2014101.77785	0.0004	0.1787
^{3}H	3	3016049.27767	0.0025	0.8190
^{3}He	3	3016029.31914	0.0026	0.8621
^{4}He	4	4002603.25415	0.0001	0.0150
^{12}C	12	12000000	0.0000	definition of u
^{13}C	13	13003354.83778	0.0010	0.0754
^{14}C	14	14003241.98870	0.0041	0.2914
^{14}N	14	14003074.00478	0.0006	0.0443
^{15}N	15	15000108.89823	0.0008	0.0500
^{16}O	16	15994914.61956	0.0002	0.0100
^{20}Ne	20	19992440.17542	0.0019	0.0960
^{22}Ne	22	21991385.11300	0.0180	0.8185
^{23}Na	23	22989769.28087	0.0029	0.1274
^{24}Mg	24	23985041.69900	0.0130	0.5420
^{28}Si	28	27976926.53246	0.0019	0.0693
^{29}Si	29	28976494.70000	0.0220	0.7592
^{36}Ar	36	35967545.10500	0.0280	0.7785
^{39}K	39	38963706.68000	0.2000	5.1000
^{40}Ar	40	39962383.12251	0.0029	0.0716
^{85}Rb	85	84911789.73700	0.0120	0.1413
^{87}Rb	87	86909180.52600	0.0120	0.1381
^{133}Cs	133	132905451.93200	0.0230	0.1731
^{134}Cs	134	133906718.47500	0.0280	0.2091

Table 2.1: Nuclides with an uncertainty in their atomic mass of 1 ppb or less. Only 23 of more than 3200 nuclides have been measured with such a precision [Aud03]. ^{39}K is included, since it is frequently used as a calibration mass.

In both cases, the error of the reference mass has to be as small as possible. Unfortunately, there are only a few nuclides out of more than 3200 nuclides known so far with sufficient precision (see Tab. 2.1). Nuclides frequently used for mass calibration are ^{12}C, ^{23}Na, ^{39}K, ^{85,87}Rb and ^{133}Cs. ^{12}C is an obvious choice since the unified atomic mass unit is defined as 1/12 of the mass of ^{12}C and thus has no uncertainty. The other ions are available from a surface ionisation source and therefore of high interest (although ^{39}K has an relative mass uncertainty of 5 ppb).

Concerning the error in mass, the best choice is to use ^{12}C or carbon clusters as reference ions, the latter are molecules of multiple carbon atoms. Thus, the atomic masses can be directly be measured in u, i. e. absolute mass measurements can be performed, if carbon clusters are used as a reference. Thereby, the error of the calibration mass is eleminated by definition. An uncertainty occurs only due to the binding energy of the carbon clusters, which is a few eV per atom and can even be corrected. However, in case of mass measurements on short-lived nuclides the error in the $^{12}C_n$ binding energy can be neglected compared to the relative uncertainty of typically 10^{-9} for radionuclides. Since a large number of carbon clusters are stable, the whole nuclide chart can be covered with reference masses with gaps of only 12 atomic mass units (see Fig. 2.8). The use of carbon clusters for mass calibration has been recently applied at ISOLTRAP (ISOLDE / CERN) [Bla02, Bla03b], in order to get the systematic errors in mass determination as small as possible for all available nuclides. In the following, a few systematic uncertainties shall be discussed which are related to the discussion on the choice of the reference mass.

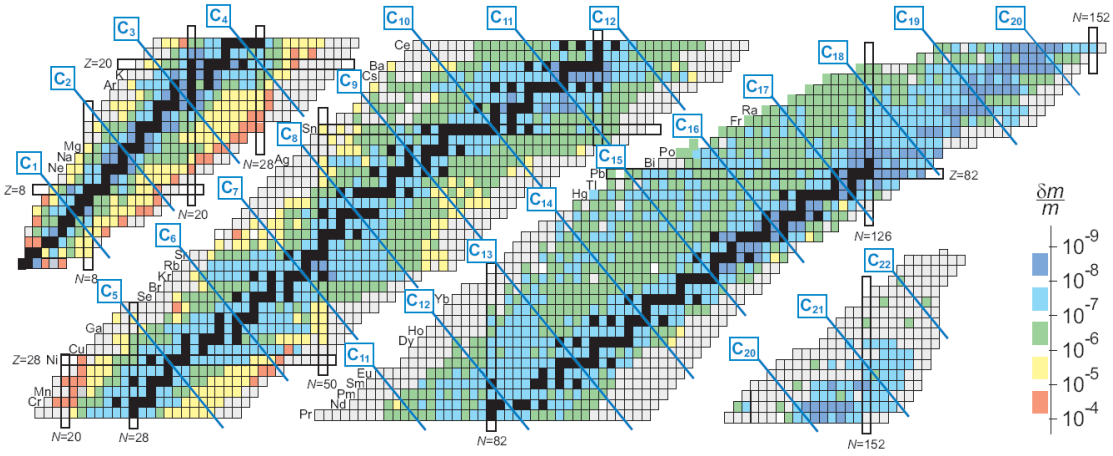

Figure 2.8: Nuclide chart of all known nuclides with their relative mass uncertainty $\delta m/m$ coded in different colors. Stable isotopes are marked black. The isobaric lines of the carbon clusters are marked by diagonal blue lines, which illustrates, that by using carbon clusters many reference masses are available over the whole nuclear chart [Bla06].

Electric and magnetic field errors contribute to systematic uncertainties [Bol90]. If the potential of the real trap is expressed by a multipole expansion, imperfections in the electric field result in multipole terms of higher order. The most important contributions are the octupole C_4 and dodecapole moment C_6, which lead to a frequency shift of the cyclotron frequency:

$$\Delta(\omega_c)^{elec} \approx \omega_- \left[\frac{3}{2}\frac{C_4}{d^2}(\rho_-^2 - \rho_+^2) + \frac{15}{4}\frac{C_6}{d^4}\left[\rho_z^2(\rho_-^2 - \rho_+^2) - (\rho_-^4 - \rho_+^4)\right]\right]. \qquad (2.37)$$

The frequency shift is proportional to ω_-, which is approximately independent of the particle's mass (see Eq. (2.17)). Using Eq. (2.32) to determine m_{ion} in a TOF-ICR measurement via a reference mass, the deviation from the real mass value due to a

mass independent frequency shift of the cyclotron frequency $\Delta\omega_c$ can be expressed by the following term:

$$\Delta m_{ion} = \frac{\Delta\omega_c}{\Delta\omega_c + \omega_{c,ion}}(m_{ref} - m_{ion}). \tag{2.38}$$

This systematic shift is directly proportional to the mass difference between the reference ion and the ion of interest. Here, it is obvious that reference ions of similar mass, ideally mass doubletts, are required to avoid systematic errors. In the following an expression for the systematic error δm_{ion} for a mass independent frequency shift is obtained in the case of FT-ICR measurements, where two reference masses are required. Using Eq. (2.33) to calculate the mass shift $\delta m_{ion} = m_{ion}(\omega + \Delta\omega)$ - $m_{ion}(\omega)$ and the approximation $\omega_+ \approx \omega_c$ the following result is obtained:

$$\delta m_{ion} = -\frac{\Delta\omega^2}{(\omega_{+,ion} + \Delta\omega)^2}\frac{1}{m_{ion}}(m_{ion} - m_1)(m_{ion} - m_2). \tag{2.39}$$

If the real expression for the reduced cyclotron frequency ω_+ is used, a Taylor expansion of δm_{ion} in the frequency shift $\Delta\omega$ leads in highest order to the following expression:

$$\delta m_{ion} \approx -2\Delta\omega\frac{m_{ion}(\chi_1 - \chi_2)(m_{ion}\chi_1 - m_1\chi_{ion})(m_{ion}\chi_2 - m_2\chi_{ion})}{\alpha\chi_{ion}^3(m_1\chi_2 - m_2\chi_1)}, \tag{2.40}$$

where $\alpha = eB/2$ and the parameter χ_i is mass dependent, and given by:

$$\chi_i = 1 + \sqrt{1 - m_i\frac{2U}{eB^2d^2}}. \tag{2.41}$$

In both cases the shift of the mass is also zero in case the reference ions with identical mass are used, $m_{ion} = m_1$ or $m_{ion} = m_2$. Thus, for FT-ICR as well the best choice are reference ions of a mass as close as possible to the mass of the nuclide of interest.

A tilt of the trap axis against the magnetic field axis also contributes to a systematic error (as in Eq. (2.38)) due to a mass independent frequency shift, expressed by [Bol90]:

$$\Delta(\omega_c)^{tilt} = \frac{9}{4}\omega_- \sin^2(\Theta), \tag{2.42}$$

where Θ is the tilt angle. To avoid this, the trap has to be aligned very carefully.

The homogeneity of the magnetic field can also be distorted, for example due to materials with a high magnetic susceptibility μ which are close to the homogenous region of the trap. The lowest order of imperfection, which leads to frequency shifts, is the magnetic hexapole component. The frequency shift is proportional to the cyclotron frequency:

$$\Delta(\omega_c)^{magn} = \beta_2\omega_c(\rho_z^2 - \rho_-^2), \tag{2.43}$$

where β_2 is the relative strength of the hexapole moment of the magnetic field. The absolute value of the cyclotron frequency is shifted by this higher order contribution,

but no further error occurs in mass calibration, since the frequency shift is mass dependent.

Other contributions for frequency shifts arise from the Coulomb interaction in case multiple ions are stored in the trap. In this case, the dependance of the frequencies on the number of particles can be investigated, using different numbers of stored ions. Afterwards, the frequency can be obtained by extrapolation to a single ion stored in the trap [Kel03].

Carbon clusters allow to minimize systematic errors in a mass measurement due to the small mass difference between the reference ion and the ion of interest (m_{ref} - m_{ion}). Furthermore, systematic uncertainties of the apparatus can be investigated by comparing frequencies of different carbon clusters. Thus, the availability of carbon clusters for Penning trap mass spectrometry is improving the accuracy of the measurement procedures. For this reason a suitable ion source is required. In the work presented here the design of a new, reliable and highly efficient carbon cluster ion source for the TRIGA-TRAP mass spectrometer was developed and is described in Chap. 3. The investigation of the carbon cluster ion production is discussed in Chap. 6.

Chapter 3

Design of a laser-ablation ion source

The laser ion source, which has been developed for the production of carbon cluster ions as well as for the desorption and ionisation of heavy elements, is described in this chapter. The available surface and electron impact ion sources at TRIGA-TRAP are discussed first. The reasons why they are not suitable for the carbon cluster ion production are mentioned. Next, the laser ionisation mechanism and finally the design of the source and the test setup, in which the mass spectrum of the produced ion pulses were investigated, is introduced.

3.1 Ion production at the TRIGA-TRAP setup

The surface ion source

Surface ionisation is known as the process where the vapor of an element gets ionised by getting in contact with a hot surface. Depending on the work function of the surface and elements in use, this process can deliver either positively or negatively charged ions[1].

Positively charged ions are created by using a surface with a high work function, for example tungsten or molybdenum, and atoms with a low ionisation potential. If the ionisation potential exceeds ≈7 eV, an efficient ionisation is no longer possible. Hence this process can only deliver ions of alkali or earth-alkali elements, and a few other elements with sufficiently low ionisation potential.

The creation of positively charged ions can be understood as follows: when an atom of the vapor hits the hot surface it gets adsorbed and ionised with a certain probability, which is determined by the cross-section of this process. If the atom stays long enough on the surface to get in thermal equilibrium, the ionisation probability

[1]Negatively charged ions can be created by using a surface with a low work function and elements with a high electron affinity, for example halogen atoms. A caesium-covered tungsten plate can be used as the ionising surface in this case. But this process is not of interest for the following discussion.

material	ϕ_s / eV	ϕ_i / eV	A_e / eV
Ni	4.61	7.6	1.1
Mo	4.15	7.2	1.3
Ta	4.12	7.8	0.6
W	4.54	8.0	0.6
W + O	6	–	–
Ir	5.40	9.0	1.9
Pa	5.32	9.0	2.5
Re	4.85	7.9	0.2
Li	2.46	5.4	0.6
Na	2.28	5.1	0.55
K	2.25	4.3	0.5
Rb	2.13	4.2	0.49
Cs	1.81	3.9	0.4
Ca	3.20	1.6	-1.5
Sr	2.74	5.7	-1.0
Ba	2.11	5.2	-0.5
rare earth metals	≈ 3.5	5.6-6.9	$\approx$0.5

Table 3.1: The work function ϕ_s, the ionisation potenial ϕ_i, and the electron affinity A_e for different materials [Smi67, McD72, Alt86, Alt93]. The electron affinity is of interest for the surface ionisation of negatively charged ions. The ionisation probability can be expressed similar to Eq. (3.1), where $(\phi_i - \phi_s)$ is replaced by $(\phi_s - A_e)$.

for singly charged ions can be expressed by the Langmuir-Saha equation [Lan25]:

$$p_i = \frac{n_i}{n_i + n_a} = \left(1 + \exp\left[-\frac{e(\phi_i - \phi_s)}{kT}\right]\right)^{-1}. \tag{3.1}$$

n_i and n_a are the number of ions/atoms leaving the surface, ϕ_s is the work function of the surface, ϕ_i the ionisation potential of the atoms, e the elementary charge, k the Boltzmann constant and T the surface temperature. Tab. 3.1 lists values of ionisation potenials ϕ_i and work functions ϕ_s of different elements.

In case the temperature of the surface is too low, the atoms remain on the surface for a long time, which reduces the work function of the surface by the outermost layer of atoms. Thus, this effect decreases the ionisation rate. If the temperature is too high the time in which the ion is adsorbed on the surface decreases. This lowers the ionisation probability due to shorter interaction times. To ionise alkali atoms, a temperature between 1000-1500 K is suitable [Zha99].

In order to produce alkali ions in our experiment, a surface ion source manufactured by R. Kirchner at GSI is used, see Fig. 3.1. A cavity, which is made of a tungsten cup, is heated via electron bombardment from a heated filament ($U = 2.9$ V, $I = 12.0$ A). The cavity contains caesium zeolite ($Cs_{12}[(AlO_2)_{12}\ SiO_2)_{12}]$), which is used as emitter material for caesium[2] in this source. The caesium is inserted into

[2]This source is also suited to generate sodium, potassium and rubidium ions, if a corresponding emitter material is used.

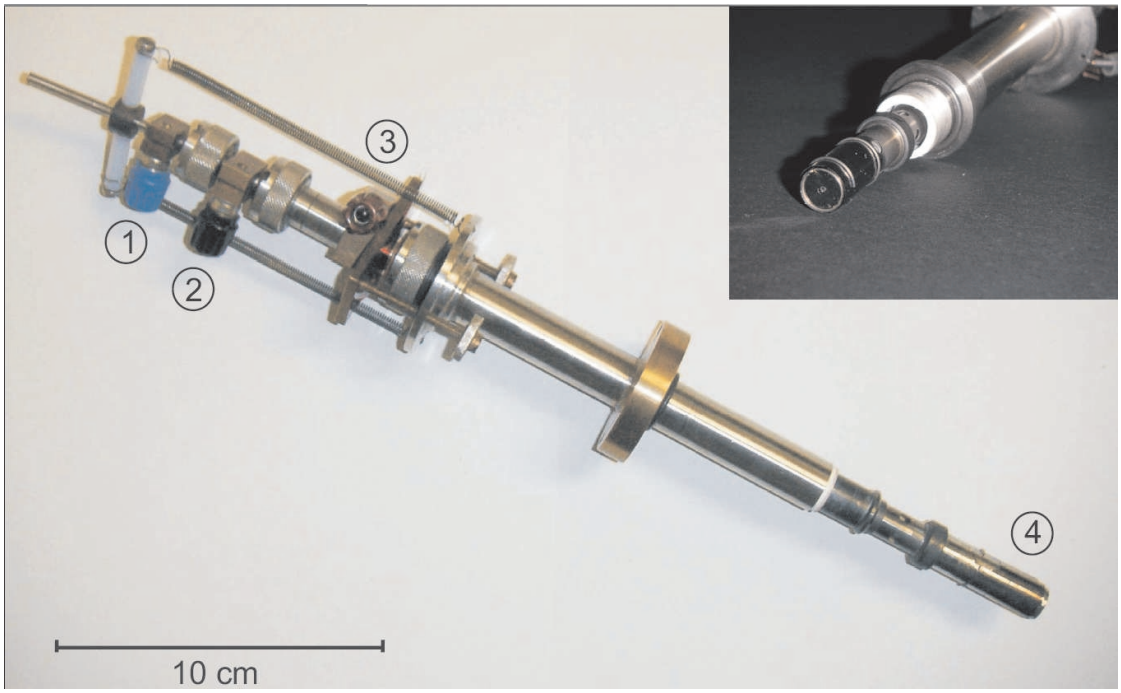

Figure 3.1: A picture of the surface ion source with a hot cavity used to produce caesium ions. The connectors (1) and (2) are used to apply a heating current to the tungsten filament, which heats the cavity by electron bombardment. To define the energy of the outcoming ions, a voltage is applied to connector (3). The cavity with the supply material is located at (4). The ions are extracted through a hole with 0.5 mm diameter (see inset).

the zeolite by a chemical process [Ohs06]. Due to the heating of the cavity by the electron bombardement, caesium is released from the compound and ionised when it touches the hot tungsten surface.

The cavity is used to increase the ionisation efficiency, compared to a single surface for ionisation, since the atom underlies multiple collisions with the surface before it leaves the cavity, see [Kir90] for a detailed discussion. Ions can be extracted by an extraction field through a small hole (d = 0.5 mm) in the tungsten cup. Thereby the ion energy is defined by the voltage applied to the ion source (up to about 1.1 kV).

This surface ion source is well suited to provide a continuous ion beam of alkali atoms with a current of some nA. As discussed above (see Sect. 2.3) these elements are used as reference ions, and also used for optimising the apparatus off-line, where a reliable ion source with a high intensity is required. The output current can be changed by increasing or decreasing the heating current of the filament. For loading ions into a Penning trap it is ideal to have a short pulse of ions, typically about 10 μs long. Therefore an ion pulse has to be created from this source, for example by switching the extraction voltage or the bending voltage of a 90° bender, which is used to bend the ions on the main beamline (see Chap. 4). Nevertheless, the source continuously emits ions and neutral particles, which leads to a higher background pressure when the source is running. Modulation of the output by changing the

current of the filament is not possible since the response time of the source is in the order of minutes.

As for the production of carbon-cluster ions, this type of source is not suitable, as it is difficult to create and vaporize a sample containing all kinds of carbon clusters. Also, the ionisation potential of carbon is too high. Furthermore, it is difficult to run a surface ion source with a sample where only a few atoms are available, as in the case of heavy nuclides, which are the subject of investigation at TRIGA-TRAP. The number of available atoms will be about 10^{12} and even down to only 10^{8} in some special cases. If an ion pulse of 10 μs length should contain as many ions that at least one is measured and detected, this requires a flow of about 10^{7} ions/second, assuming an overall efficiency of the apparatus of 1%-5%. Then only a fraction of 10^{-7} of the available atoms could be used for the measurent. Assuming a constant output, this would limit the running time of the source to about 20 minutes for a sample of 10^{10} atoms.

The electron impact ion source

When an atom (or a molecule) is hit by an electron of a sufficiently high kinetic energy, an electron of the atom can either be brought into an excited state or into the continuum, thereby creating an ion. This process is known as electron impact ionisation, which in the most simple case leads to the following reaction, where A is an atom or a molecule:

$$A + e^- \rightarrow A^+ + 2e^-. \tag{3.2}$$

The ionisation efficiency, which is the number of ionised particles per incident electron and per target particle, depending on the energy of the incident electron E_e and the first ionisation energy E_i of the atoms or molecules, is determined by the ionisation cross-section. Fig. 3.1 shows the cross-section as a function of E_e for different elements. If the electron energy E_e is smaller than E_i, the cross-section is zero. For electron energies slightly above E_i, the ionisation cross-section σ_i can be approximated by the following equation:

$$\sigma_i = \beta(E_e - E_i)^n, \tag{3.3}$$

where β is a constant, and $n = 1.1269$ for the ionisation of atoms or $n = 1.056$ for the ionisation of singly charged ions. The cross-section has a maximum at 3-4 times E_i, which is about 60 eV to 100 eV for most of the elements which are available as gases [Vál77].

In the TRIGA-TRAP setup a commerically available electron impact ion source, a so called Axial Molecular Beam Ionizer, manufactured by ABB Automation Inc. (see Fig. 3.3), is implemented in order to ionise residual gas inside the apparatus. To increase the output current of the source, gas can be leaked into the source, for example helium or argon.

A tungsten filament is heated to provide electrons by thermal emission to create a beam for the electron bombardement. By applying a voltage between the filament and the cylindrical cage, i.e. the ion region where the ions are created, the electron impact energy is defined. All ions created within the ion region are extracted

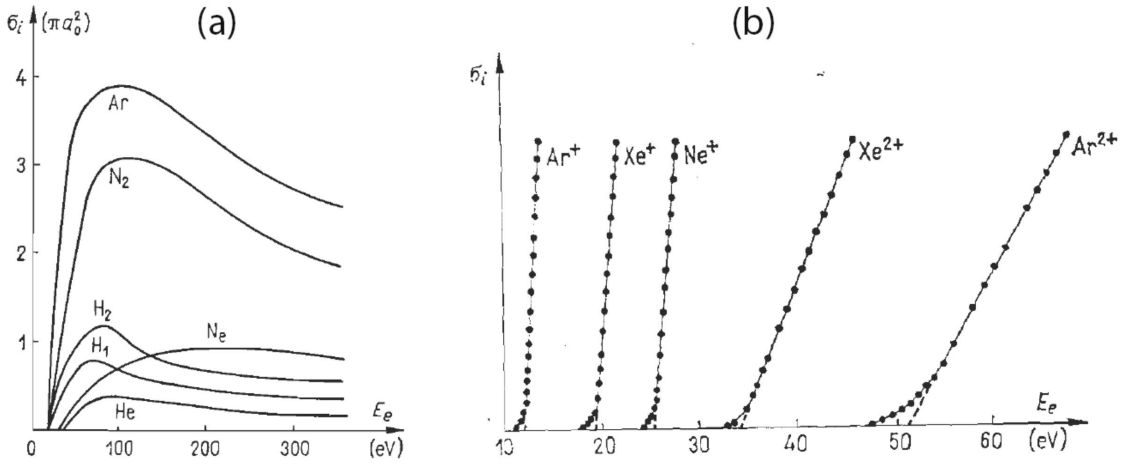

Figure 3.2: (a) Ionisation cross-section σ_i as a function of the electron energy E_e for different gases. (b) Behaviour of the ionisation cross-section close to the ionisation threshold [Vál77].

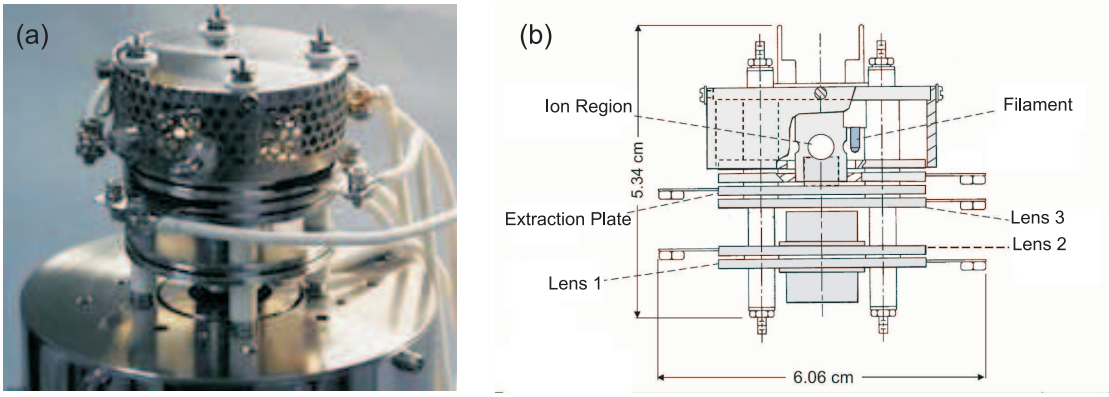

Figure 3.3: (a) The assembled Axial Molecular Beam Ionizer manufactured by ABB Automation Inc. [ABB01]. (b) A schematic drawing of the source together with the extraction electrodes. Electrons, released by the heated tungsten filament, gain kinetic energy due to the electric field between the filament and the ion region. Ions are created within the ion region by electron impact, and extracted and collimated by an extraction plate and an einzel lens.

by a negative voltage on the extraction plate, and collimated with an Einzel lens. Thereby, the ions' kinetic energy is defined by a positive voltage applied to the ion region. By pulsing this voltage, the creation of ion pulses of e.g. helium, argon and of other gaseous elements and molecules of up to 250 eV kinetic energy is possible. This source also provides a reliable, high intensity ion beam for off-line optimisation.

To create ions with this source, it is necessary to get the desired species into the gas phase, and to create a continuous gas flow into the ioniser. Since most of the experimentally required ions, namely the carbon-cluster ions and the heavy nuclides, are only available in solid form, this kind of ion source is not suitable for the creation of most of the ion species except an atomiser is used in combination with this source.

However, the low overall efficiency due to the continuous atomisation also applies here, as discussed above.

3.2 Introduction to laser ion sources

Lasers can also be used to create ions, where two different ionisation processes have to be distinguished:

1. Atoms or molecules can be ionised by directly absorbing photons from a laser. Since the ionisation energy is too high for most of the elements, an electron is first brought into an excited state by a laser, which has to be resonant to a transition of the atom. Afterwards the electron is transfered into the continuum by absorbing a second photon from the same or from a second laser. For every single resonant excitation step of each element a laser with a unique wavelength is required. However, when using one or more resonant excitation steps, a very high elemental or even isotopic selectivity of this ionisation process can be reached. This type of ion source is known as resonance ionisation laser ion source (RILIS) [Koe02] and e.g. in use at the ISOLDE facility at CERN [Kug00].

2. The second possibility of creating ions by laser is to produce ions via ablation. A pulsed laser with a high intensity is focused on a small spot on the surface of a solid target, with a power density of at least 10^8 W/cm^2. By absorbing energy from the laser, this spot is heated, so that depending on the wavelength, pulse energy, pulse duration, and the properties of the target and its environment, different processes of laser-target interaction can occur. The most important ones are electric sputtering, normal vapourisation, normal boiling, and for some materials and high pulse energies explosive boiling, also called phase explosion [Kel04]. The vaporised material forms a plasma plume above the surface, where the target atoms are ionised. This method is not element specific at all, a large number of different ions can be produced, from singly charged ions to cluster ions [Bla03a], and also highly-charged ions are possible [Lás96, Mró96].

Laser ablation is suitable to produce carbon cluster ions for mass spectrometry applications. This has already been demonstrated at ISOLTRAP/CERN [Bla02] and SHIPTRAP/GSI [Cha07]. Carbon cluster ions will be used as mass calibration for TRIGA-TRAP, as described in Chap. 2.3. For this purpose a laser ablation ion source has been developed. The setup of the ion source is described in detail in the next section, the results of the ion production are discussed in Chap. 6.

Compared to the surface ion source, this kind of ion source has the advantage that ions are extracted in short pulses after the laser irradiation, ideal for loading the ions as a pulsed beam into a Penning trap. Another advantage is that the source can be placed in high vacuum, since no particles are evaporated, except the plasma plume during the laser irradiation, thus keeping the vacuum conditions excellent. Another advantage is that no atoms of the source reservoir are lost between two pulses, so that a larger fraction of source reservoir might be accessible for trapping

applications in comparision to ion sources with continuous ionisation. Tests concerning the ionisation of heavy nuclides by laser ablation have been performed (see Chap. 6), to investigate whether the laser ion source is also a suitable ion source for heavy nuclides.

3.3 Laser ion source setup

In the following, the laser system, the sample holder, the extraction system, and ion optics of the laser ion source being designed and constructed within this thesis are described. For an overview a sketch of the ion source is presented in Fig. 3.4.

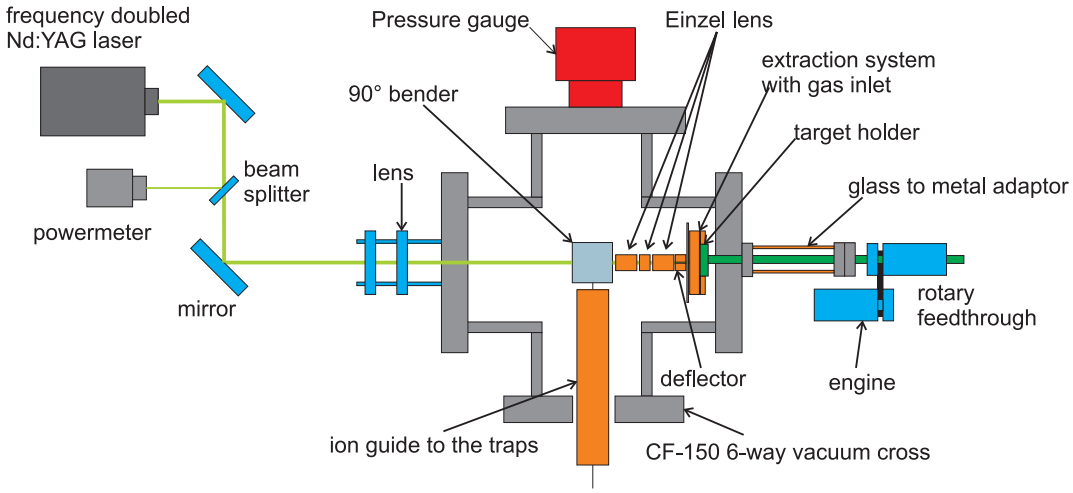

Figure 3.4: Schematic drawing of the carbon cluster laser ion source setup. The connection to the prepump and the turbo molecular pump is for simplicity not shown. A frequency-doubled Nd:YAG laser ($\lambda = 532$ nm) is guided and focused on a sigradure or C_{60} target which is fixed on a rotatable target holder. A small motor is rotating the target. The produced ions are extracted with an extraction plate and guided to a 90° bender by a deflector and an einzel lens and finally transported by an ion guide to the traps. In order to place the rotary feedthrough on high voltage the rotary feedthrough and the engine are electrically isolated.

Laser system

The laser in use is a Continuum Minilite frequency-doubled Nd:YAG laser with a wavelength of $\lambda = 532$ nm, a pulse duration of 3 to 7 ns, and a repetition rate of 1 to 15 Hz. The pulse energy is measured with a pyroelectric detector (Scientech-PHDX-25), further called powermeter, with an uncertainty of 8%. Since the glass of the powermeter transmits only about 95% of the incident light, the observed values are corrected by this factor. The threshold for laser pulse observation of the powermeter is 150 μJ, pulses of lower energy are not detected. A maximum pulse energy of the laser of about 48 mJ at $\lambda = 532$ nm was measured.

The laser has an internal power regulator operating as a user adjustable polarisation filter. In order to monitor the laser pulse energy of the beam, which is

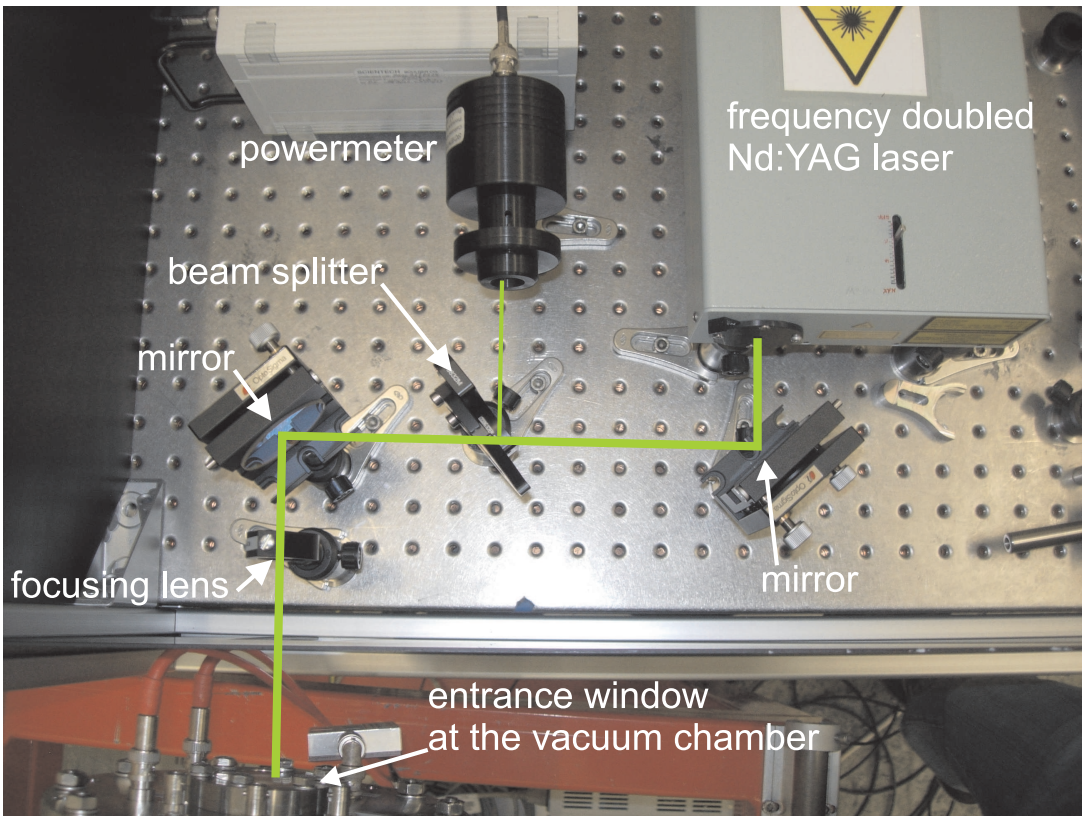

Figure 3.5: Setup of the laser system. A frequency-doubled Nd:YAG laser is guided to the target inside the vacuum chamber. A small fraction of the laser is used to monitor the intensity of the beam with a powermeter. The solid lines indicate the propagation of the laser beam.

guided with suitable mirrors into a vacuum chamber, a beam splitter is used to reflect a small fraction (11%) of the beam into the powermeter by Fresnel reflection. The beam splitter is tilted by 45° against the incident beam. Tab. 3.2 lists different positions of the polarisation filter and the measured corresponding pulse energy. Observed values of the laser output, the transmission, and the brightest reflection from the beam splitter are presented. About 80% of the initial energy are transmitted to the target, while 11% are used for monitoring. The remaining fraction is lost e.g. due to multiple reflections inside the beam splitter. Thus, due to the powermeter threshold, pulse energies below 1.2 mJ at the target can not be monitored. Further energy losses are occuring at the mirrors (≈3%) and the CF-40 window (≈10%), where the laser beam enters the vacuum chamber. A picture of the setup of the laser system is shown in Fig. 3.5.

Laser focus

In order to achieve a high power density at the position of the target, the laser beam is focused on its surface. The diameter of the focus of the frequency doubled Nd:YAG laser has been determined for different lenses at the target position. Thereby, the deposited energy and the laser spot size at the target sample for the production

Switch position	Initial pulse energy in mJ	Transmitted fraction	Reflected fraction
MAX	47.77±0.55		
20	32.82±0.22		
14	16.31±0.10	83.2%±1.4%	12.6%±1.4%
12	11.52±0.10	87.1%±1.8%	11.1%±1.4%
10	7.61±0.11	80.8%±1.9%	10.9%±1.8%
8	3.91±0.04	74.2%±2.3%	9.7%±3.0%
6	1.75±0.01	76.1%±2.1%	10.7%±2.4%
4	0.59±0.01	76.5%±2.6%	
	on average	79.6%±4.5%	11.0%±0.9%

Table 3.2: Measurement of the laser pulse energy. The incident, transmitted and reflected laser pulse energy of a beam splitter are presented in dependence of the switch position of the power regulating polarisation filter. The last line contains the average transmitted and the reflected fraction.

of ions is known. The beam profile was investigated via the knife-edge method as described in [Wri92]. A knife edge is moved via a micrometer screw into the laser beam, while the laser pulse energy of the part which is not cut-off is measured with a powermeter as a function of the position of the knife edge. For an overview of the setup see Fig. 3.6.

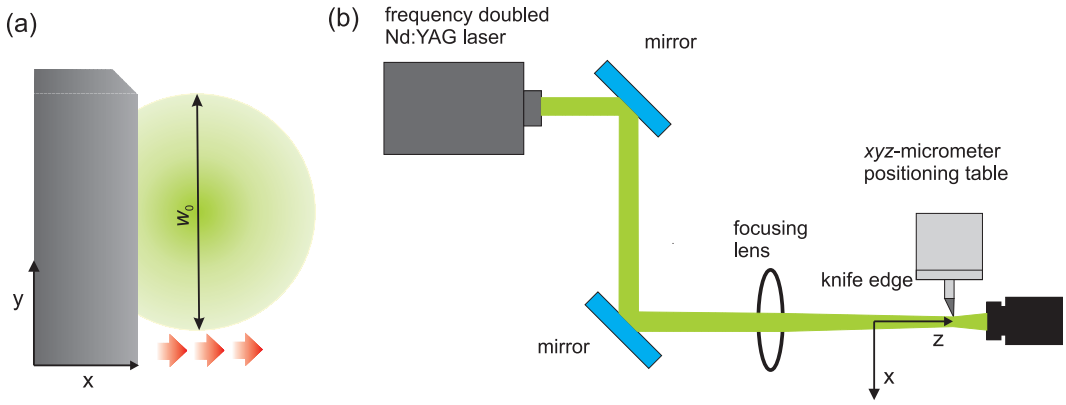

Figure 3.6: (a) Illustration of the laser focus diameter measurement method: the transmitted intensity is measured in dependence of the position of the knife edge. (b) Sketch of the setup for this measurement. The knife edge is moved via a *xyz*-positioning table with micrometer screws into the laser beam. A powermeter detects the transmitted intensity. Lenses with different focal lengths (85 cm, 45 cm and 3 lenses combined with a focal length of 16.9 cm) were put into the laser beam. The diameter was measured for each lens by moving the knife edge vertically and horizontally through the laser beam.

The radius of the beam is defined as the distance where the amplitude of the electric field of a laser with a Gaussian beam profile drops to 1/e (and the intensity by $1/e^2$) of the maximum value. An equation for beam diameter is obtained by

integrating the beam profile over the area which is not covered by the knife edge. This leads to [Wri92]:

$$D(1/e^2) = 1.56(x(90\%I_{max}) - x(10\%I_{max})), \tag{3.4}$$

where $x(90\%I_{max})$ is the position of the micrometer screw at 90% of the maximum intensity and $x(10\%I_{max})$ ar only 10% intensity.

The beam width at the focus point was measured for: two different lenses with a focal length of $f_1 = 45$ cm and $f_2 = 85$ cm, without any lens, a combination of three lenses leading to a calculated focal length of $f_3 = 16.9$ cm, and with a lens system which spreads the beam to a larger diameter (see Fig. 3.8 and discussion below). A fit function is used to obtain $x(90\%I_{max})$ and $x(10\%I_{max})$ from the experimental data. If the knife edge at position x_0 is moved in x-direction, the transmitted intensity for a Gaussian beam propagating in z-direction is given by:

$$I(x_0) = \rho_0 \int_{-\infty}^{\infty} dy \int_{-\infty}^{x_0} dx\ e^{-\frac{(x-\mu)^2+y^2}{\sigma^2}} = \rho_0\sqrt{\pi\sigma} \int_{-\infty}^{x_0} dx\ e^{-\frac{(x-\mu)^2}{\sigma}}, \tag{3.5}$$

where ρ_0 is the power density on the z-axis, μ is the central beam position in x-direction (zero is assumed for y-direction), and σ is the beam width. This integral was approximated by the following fit function:

$$I(x_0) = \frac{I_{max}}{1 + e^{\frac{x-\mu}{\sigma_0}}}, \tag{3.6}$$

where I_{max}, μ and σ_0 are fit parameters. $x(90\%I_{max})$ and $x(10\%I_{max})$ are taken from the fit result. Applying the two positions to Eq. (3.4) results in:

$$D(1/e^2) = 1.56\ln(81)\ \sigma_0. \tag{3.7}$$

Fig. 3.7 shows a plot of the fit function compared to the data for one measurement. The results are listed in Tab. 3.3.

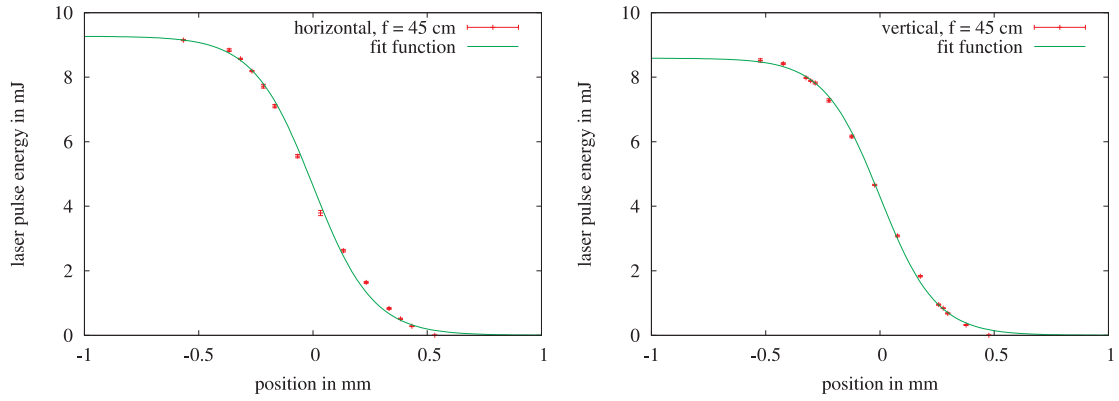

Figure 3.7: Transmitted laser pulse energy in dependence of the knife-edge position for a lens with a focal length of $f = 45$ cm, moving the knife edge in horizontal (left) and vertical (right) direction. The fit function in Eq. (3.6) was applied to the data.

focal length / cm	$D(1/e^2)_{hor}$ / mm	$D(1/e^2)_{vert}$ / mm	ρ_{max} / (W /cm^2)
85.0	1.22±0.05	1.81±0.16	$5.48{\cdot}10^8$
45.0	0.84±0.02	0.89±0.03	$1.62{\cdot}10^9$
16.9	0.37±0.02	0.41±0.02	$8.09{\cdot}10^9$
45.0*	0.24±0.02	0.26±0.02	$1.90{\cdot}10^{10}$
no lens used	2.63±0.08	2.68±0.24	$1.73{\cdot}10^8$

Table 3.3: Results of the laser beam diameter measurement. The diameter for moving the knife edge horizontally $D(1/e^2)_{hor}$ and vertically $D(1/e^2)_{vert}$ through the laser and the maximum reachable power density ρ_{max} are presented. In the measurement marked with * a different lens system was used, which is shown in Fig. 3.8.

The laser has a slightly elliptic beam profile, since the diameters measured in horizontal direction are smaller than those in vertical direction. The beam at the focus position gets larger with an increasing focal length. For a Gaussian beam passing through a lens with focal length f, the following equation for the focus diameter w_0 applies [Sie86]:

$$w_0 = \frac{1}{w(f)} \frac{\lambda}{\pi f}, \tag{3.8}$$

where $w(f)$ is the beam width at the position of the lens and λ the wavelength. Currently our minimum focal length is limited to about 40 cm by the size of the CF160 6-way-cross because the laser enters it from the opposite side of the target position. This has the advantage, that the laser beam incidents perpendicularly on the target surface, thereby minimizing reflection losses. However, due to these technical constraints, the diameter of the focus is about 0.8 mm on the target surface. If an extension of the test chamber is used (see Section 3.4), the focal length is increased to 85 cm, and the beam diameter on the target to 1.2-1.8 mm. The laser can be operated with power densities up to $5 \cdot 10^8$ W/cm^2. If a higher power density would be required, the diameter of the focus has to be decreased. A possibility is a setup similar to the ion sources of ISOLTRAP[3] [Muk07] or SHIPTRAP [Cha07], where a beam diameter of 100 to 200 μm for the ablation and production of carbon cluster ions is used. There, the laser enters the chamber from the side close to the target and hits it under a certain angle. A similar setup could decrease the focal length to about 15 cm, leading to a beam diameter of about 400 μm and increasing the power density by a factor of about 5 (see Tab. 3.3). However, with this geometry a higher fraction of the irradiated laser pulse gets reflected due to the incident angle of the laser.

Another possibility is to spread the beam to a larger diameter, by using a combination of a convex and a concave lens, to increase $w(f)$ in Eq. (3.8). Lenses of larger diameter can be employed to avoid an increase of w_0 due to spherical aberation. The propagation of the laser through such a lens system was calculated using ray matrices (see Fig. 3.8). After passing through a concave and a convex lens, the

[3]At ISOLTRAP a different laser with much higher power is in use.

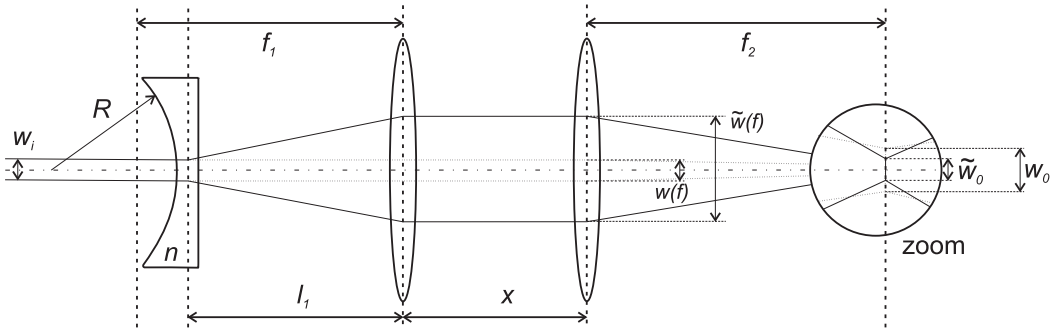

Figure 3.8: A sketch of the lens system which decreases the beam diameter on the target. The propagation of the laser with (continuous lines) and without (dotted lines) the first two lenses are shown. The laser focus is shown in a larger scale in the zoom.

diameter $w(x)$ and the divergence $\partial w(x)/\partial x$ of the laser are given by:

$$\begin{pmatrix} w(x) \\ \frac{\partial w}{\partial x} \end{pmatrix} = \begin{pmatrix} 1 & x \\ 0 & 1 \end{pmatrix} \begin{pmatrix} 1 & 0 \\ -\frac{1}{f_1} & 1 \end{pmatrix} \begin{pmatrix} 1 & l_1 \\ 0 & 1 \end{pmatrix} \begin{pmatrix} 1 & 0 \\ \frac{n-1}{R} & 1 \end{pmatrix} \begin{pmatrix} w_0 \\ \epsilon \end{pmatrix}, \tag{3.9}$$

where f_1 is the focal length of the convex lens, l_1 the distance between the lenses, n the refraction index and R the radius of the concave lens, w_0 the initial radius, and ϵ the initial divergence of the beam, which is assumed to be close to zero. The decrease of the beam diameter compared to the setup with the unspread beam is given by the following ratio:

$$r = \frac{\tilde{w}_0}{w_0} = \frac{f_2\lambda}{\pi\tilde{w}(f)} \Big/ \frac{f_2\lambda}{\pi w(f)} = 0.20, \tag{3.10}$$

where x is assumed to be 25 mm, and the lenses in use have the following parameters: $f_1 = 125$ mm, $l_1 = 100$ mm, $n = 1.515$ and $R = 12.9$ mm. By this combination of lenses the beam diameter can be decreased in theory by a factor of 5 on the target in future measurements. Expermentally, a beam diameter of about 250 μm was measured with this configuration, which is only a fraction of 3.4 smaller compared to a single convex lens with the same focal length. The deviation is propably caused by spherical aberration due to the large diameter of the beam. Furthermore, it is possible that the diameter of the laser at the last convex lens is smaller than assumed in the calculation, since the beam diameter cannot be measured there because it is larger than the aperture of the powermeter. With this lens system a power density of about $2{\cdot}10^{10}$ W/cm^2 can be reached.

Sample holder

The sample holder consists of an aluminium piece, to which the sample is attached, mounted on a rotary feedthrough (see Fig. 3.9). Depending on the size of the target material in use, different shapes of the aluminium pieces are available. For thick targets, e.g. Sigradur[4] or C_{60} pellets, a hole is drilled into the holders, so that the

[4]Sigradur is a trade name of the HTW Hochtemperatur-Werkstoffe GmbH.

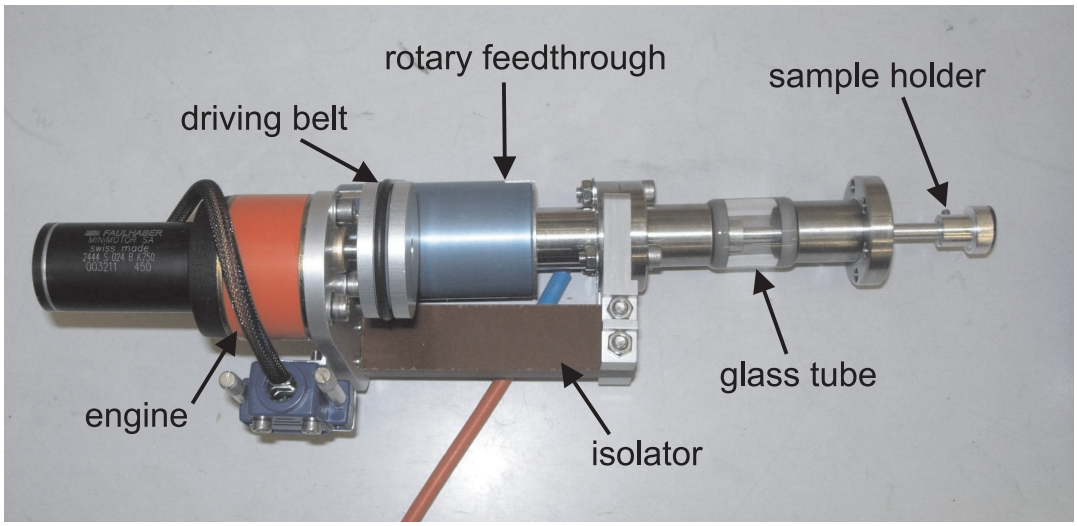

Figure 3.9: Picture of the sample holder, which is mounted on a rotary feedthrough and isolated by a glass tube from the vacuum chamber and an isolator piece from the engine, which drives the feedthrough.

surface of the target material is at the same height as the aluminium, to guarantee a parallel extraction of the created ions. Thin foil targets ($d < 0.5$ mm) are directly glued on top of a flat holder. The energy of the ions is biased by a voltage, which is applied to the rotary feedthrough and thus to the sample holder. To isolate these pieces electrically, a CF-16 glass tube is used to keep the vacuum chamber on ground and the holder of the feedthrough engine was replaced by an isolator piece. The tube is connected to the CF-150 source flange by a CF-16 connection, which is placed 5 mm off-center. By rotating the target, a long operation time of the sample is guaranteed, because the laser does not hit the same spot on the target in every shot.

Extraction and ion optics

A sketch of the ion source electrodes is shown as an overview in Fig. 3.10. The sample holder is placed in a cylinder-shaped electrode, which is split into two parts. The bottom of the cylinder has an off-center bore where the target is inserted. It is necessary to put it on the same potential as the sample holder in order to get an ion beam in forward direction. The side and the top of the cylinder are one piece and used together with an additional extraction plate as extraction elements. Both have a 3 mm diameter bore in the center, where the laser and the ions pass through. Furthermore, the extraction cylinder has a connector to leak in buffer gas, for cooling the plasma in the target region.

A deflector and an einzel lens are used to get a well-defined centered beam in forward direction. The diameter of these elements is 13 mm, the deflector is four-fold segmented and has a length of 9 mm. According to [Ada72] the length of the einzel lens electrodes was chosen to be 44 mm for outer cylinders and 13 mm for the inner electrode to obtain a quite large variation in the focal length. The gap between the electrodes is 1 mm isolated by a 1 mm thick ring made of PEEK. For a sketch of

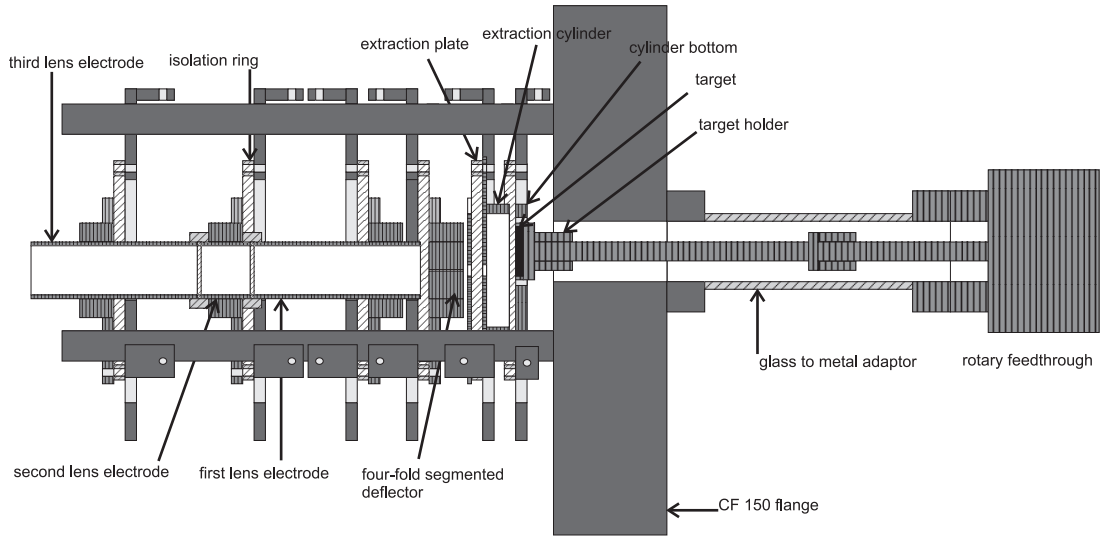

Figure 3.10: Electrode system of the carbon cluster laser ion source, consisting of two extraction electrodes, a four-fold segmented deflector, an einzel lens, and a target holder. Electrodes and parts that are on high voltage are vertically or horizonally hatched, isolating pieces are diagonally hatched.

the ion optical elements see Fig. 3.10. To isolate the electrodes from the vacuum chamber they are mounted on an isolation ring also made of PEEK. All elements are supplied with a voltage from BNC or SHV feedthroughs welded into the ion source flange (see Fig. 3.11). Tab. 3.4 contains typical experimental voltage settings for different ion energies.

Electrode	U_1 / V	U_2 / V	U_3 / V	U_3 / V
target	1100	900	550	250
cylinder bottom	1100	900	550	250
cylinder top	280	220	140	70
extraction plate	-1000	-1000	-1000	-1000
deflector	0	0	0	0
Einzel lens 1+3	0	0	0	0
Einzel lens 2	-1000	-800	-500	-220

Table 3.4: Voltage settings for different ion energies. The deflector and einzel lens voltages have to be adapted to the following ion optics.

3.4 The off-line test setup

The laser ion source should provide a large variation of carbon cluster ions as calibration masses for high-precision mass spectrometry, in order to cover a large region of the nuclear chart with calibration masses (see Sect. 2.3). An analysis of the mass spectrum obtained from different samples (see Chap. 6) with the laser ion source is performed in a test setup to identify the extracted ion species. The mass-to-charge

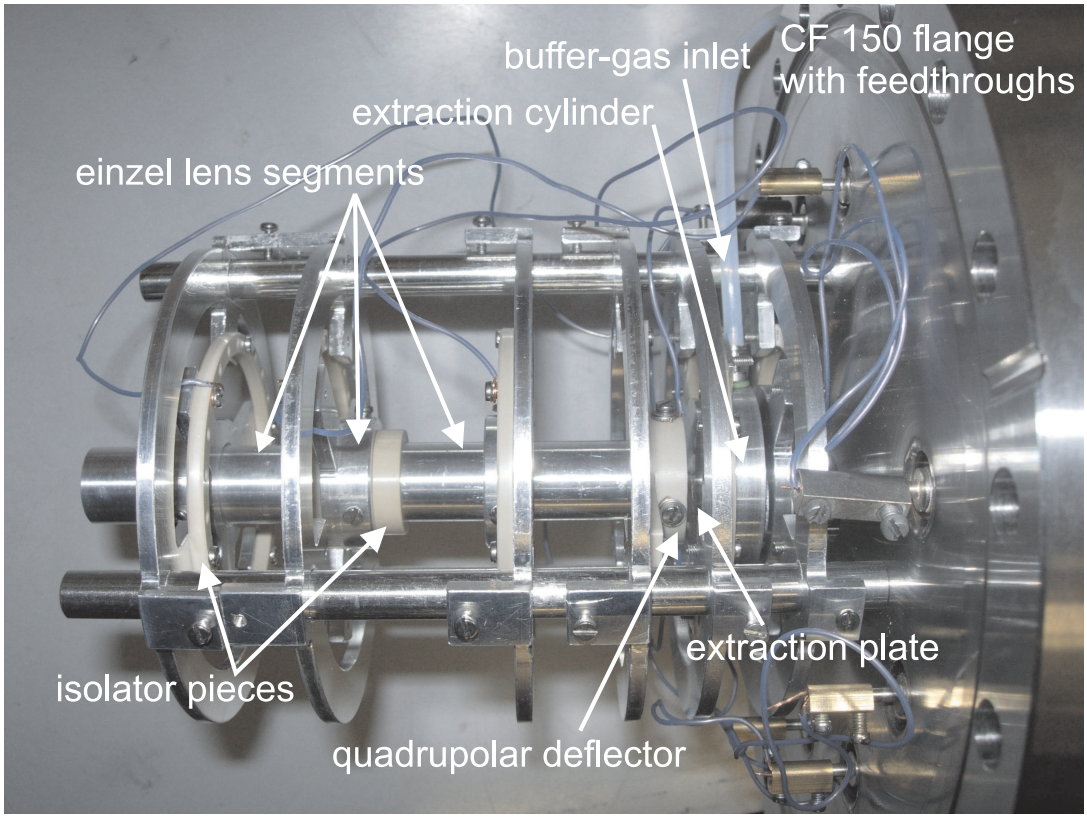

Figure 3.11: Picture of the ion source flange, where the sample holder (see Fig. 3.9) is connected from the right side. The target is placed within a cylinder-shaped electrode, which confines buffer-gas and operates with a second extraction plate as ion extraction. A deflector and an einzel lens are used to guide and collimate the ion beam.

ratio m/q of a particle is measured by detecting the time of flight of the ion from the ion source to a particle detector (see Sect. 5.2). The measurement procedure to record the time-of-flight values and the results of these measurements are described in Sect. 6. In the following the components of the test setup are described.

A six-way-cross is used as a vacuum chamber, which contains besides the ion source flange a channeltron detector[5] and a pressure gauge (Edwards BOC AIM-X). A control valve (Pfeiffer Vacuum, EVR 116) for buffer-gas injection can be used to apply helium gas to the ion source target. Without buffer-gas injection a pressure of 10^{-7} mbar is well preserved by using a prepump and a turbomolecular pump (Leybold Turbovac 340 M). A picture of the test setup is shown in Fig. 3.12.

A schematic drawing of all components inside of the setup is shown in Fig. 3.13. First a setup with a flight length of S = (18.7 ± 0.3) was in use for time-of-flight measurements. Later an additional tube was connected to extend the flight length to S = (57.5 ± 0.3) cm giving a higher resolving power. Electrodes, which are used for the ion transport, are the ion source deflector and einzel lens, and an additional einzel lens and a deflector, which are placed in the extension tube. The advantage of

[5]The operating principles of the channeltron detector are described in Sect. 4.3

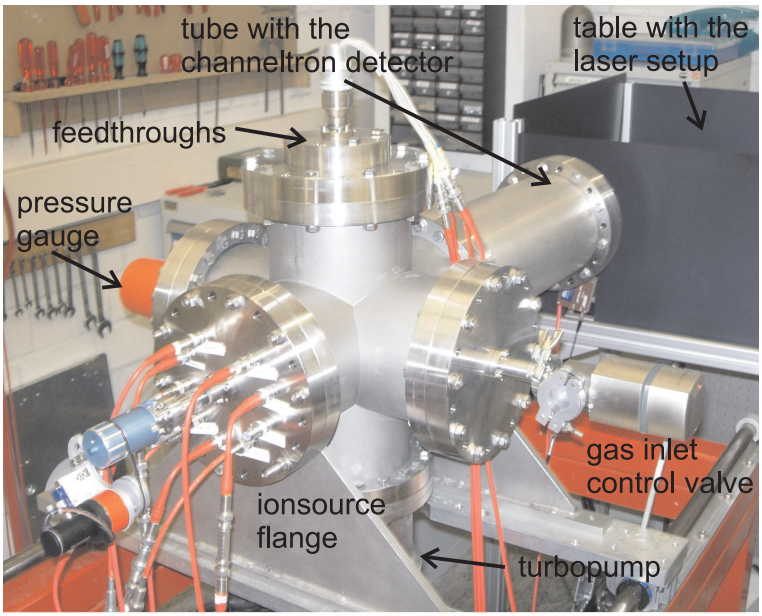

Figure 3.12: Picture of the test setup. The laser ion source is placed in a 6-way cross with a tube to extend the flight distance for the ions to the detector. A sketch of the components inside the vacuum is shown in Fig. 3.13.

the extension is that the mass resolution increases, but a lens with a larger diameter has to be used, which decreases the power density of the laser on the sample. Most results presented in this work (see Chap. 6) were recorded in the extended setup.

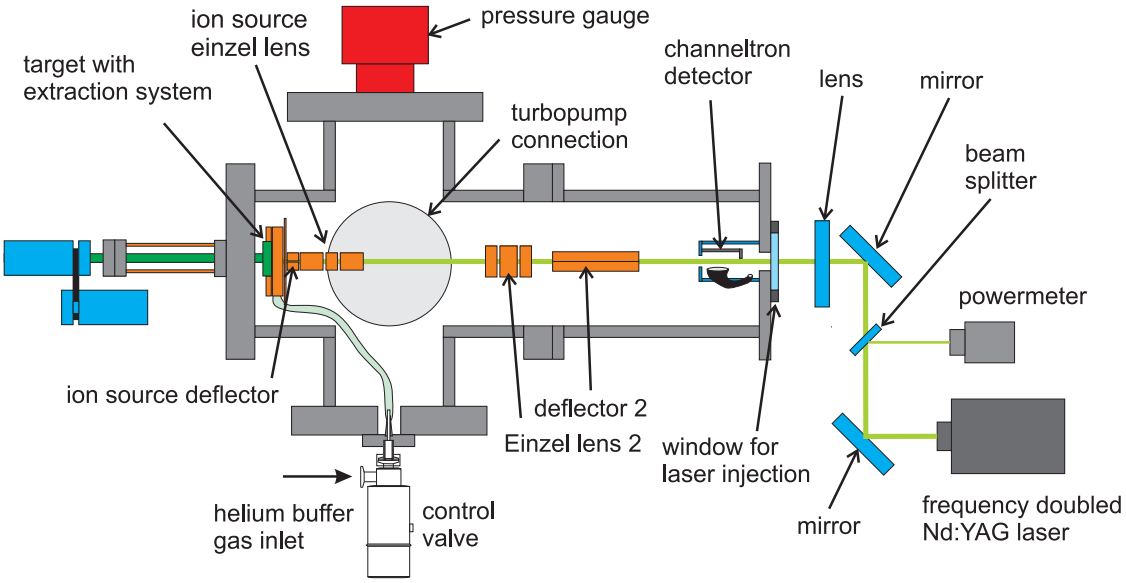

Figure 3.13: Schematic drawing of the test setup. The laser enters the vacuum chamber through the window on the right side. A channeltron detector with a conversion dynode in off-axis configuration is used for ion detection. For the ion transport the ion source deflector, ion source einzel lens, and an additional einzel lens and deflector in an extension tube are used.

Chapter 4

Experimental setup of TRIGA-TRAP

TRIGA-TRAP aims for direct mass measurements on heavy nuclides above uranium up to californium and also on neutron-rich fission medium heavy ($A \approx 130$) products from the reseach reactor TRIGA Mainz. In this chapter the overall experimental setup is discussed, a schematic overview of the mass spectrometer part is shown in Fig. 4.1.

4.1 Ion transport system

The ion transport plays a crucial role in a mass measurement experiment, since the access to nuclides with a low production rate down to one per second and less requires a good transport efficiency, in order to assure that enough ions are available for the measurement procedure. To optimise the transport efficiency, new ion optical elements were designed, constructed and integrated into the setup. Simulations of the ion transport with these new elements have been performed within this work, and are discussed in chapter 5.

To produce ions for trapping in and calibration of TRIGA-TRAP, either the surface ion source (see Sect. 3.1) is used to provide reference ions, such as $^{39}K^{+}$, $^{85}Rb^{+}$ and $^{133}Cs^{+}$ or the laser desorption ion source is used for the production of carbon-cluster ions or for desorption of thin films of transuranium elements (see Chap. 6). Both sources are located inside a CF-150 6-way cross on the entrance side of the traps (left side on Fig. 4.1), and placed off-axis, to suppress neutral particles from moving along the beamline and causing background in the detectors. The ions of interest however are bended into the main beamline by using an electrostatic 90°-bender (see Fig. 4.2), which bends charged particles of a certain kinetic energy with a quadrupolar electric field.

The bender including the electron impact ion source is a commercial device from ABB EXTREL Automation Inc. (see Sect. 3.1). Four parallel, circular-shaped 90° rod segements perpendicular to the plane of bending are used to provide the quadrupolar field. To bend the ions, the same voltage is applied to two opposite electrodes (see Fig. 4.2), the electrodes (1) and (4) are on negative potential in respect to electrode (2) and (3). To confine the electric field, all rods are placed in

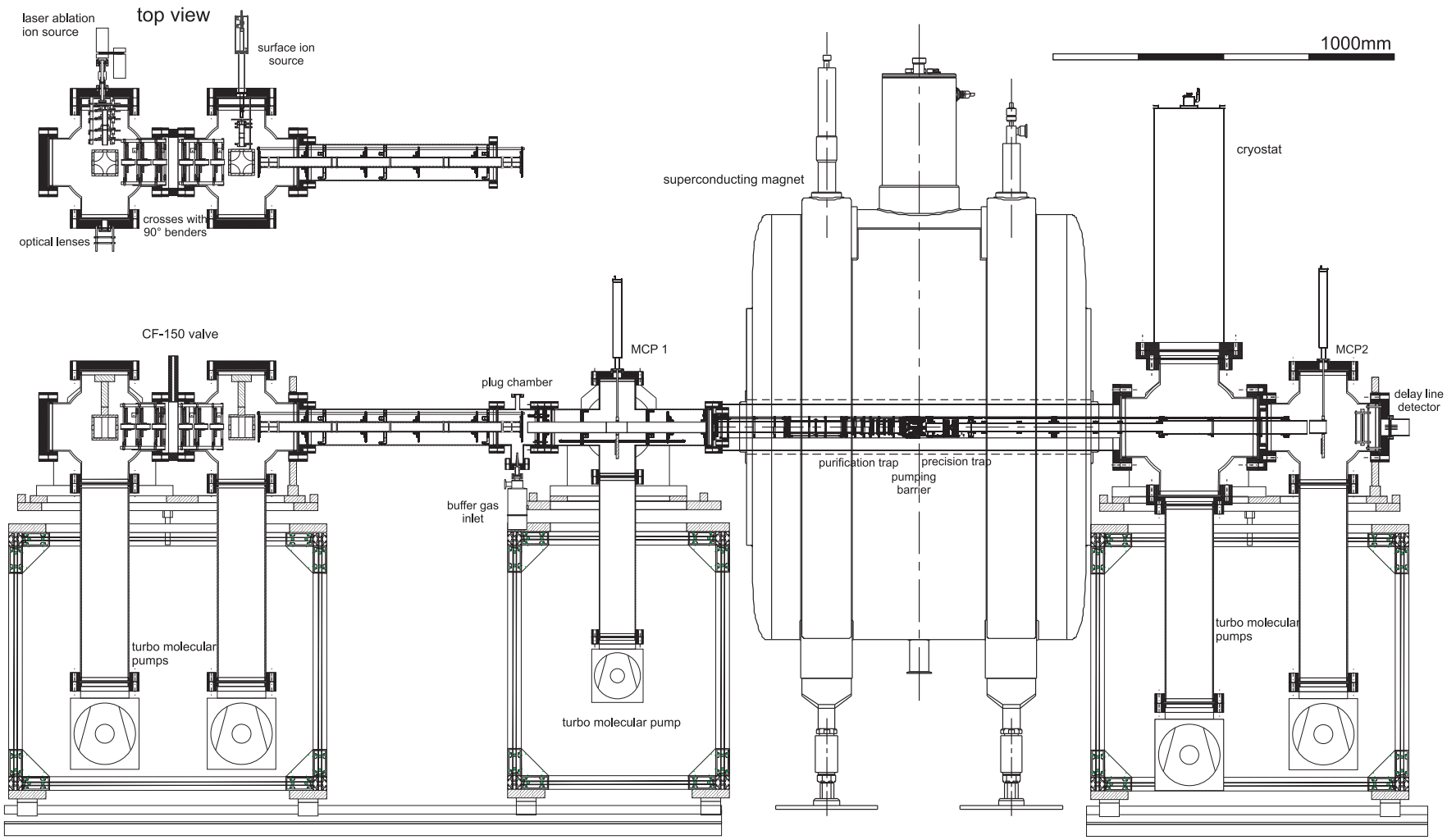

Figure 4.1: Overview of the TRIGA-TRAP setup. A superconducting magnet ($B = 7$ T) hosts the two Penning traps, which are separated by a pumping barrier. Ions, either produced by an off-line or by the TRIGA on-line ion source, are guided to the traps via 90°-benders and ion optics. For beam transport optimisation and particle detection MCP, delay-line and channeltron detectors are used. The cryostat at 4 K hosts the cryogenic amplifiers for the narrow-band FT-ICR detection, and also cools down the traps to 77 K. The vacuum in the apparatus ($p = 10^{-8}$ mbar) is provided by turbo molecular pumps [Ket09].

a cubic housing (side length 76 mm), which is kept on the same potential as the neighbouring electrodes.

The four circular-shaped holes (diameter 13 mm) for injecting and ejecting ions have each a correction ring, to compensate the field cut-off caused by the housing. The bender itself is fixed with a holder made of PEEK for isolation purposes on a CF-150 flange and inserted into the 6-way cross from the top.

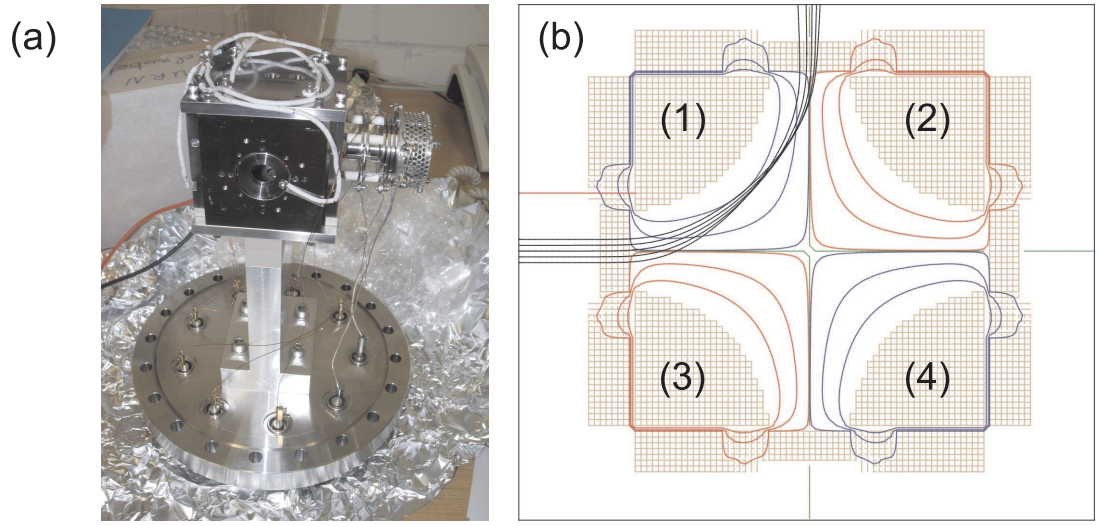

Figure 4.2: (a) Picture of the 90° bender. The electron impact ion source is mounted at the entrance on the right side. (b) Simulation of the quadrupole bender with the ion trajectory simulation software SimIon 8.0. A profile of the bending plane is shown with trajectories of bent ions (black lines) with 1 keV kinetic energy. To the electrodes (1) and (4) -850 V are applied, and 850 V to the electrodes (2) and (3), respectively. The housing and the correction rings are on ground. Equipotential lines for 0V (in green), ±10 V, ±200 V and ±500 V are shown, positive lines in red and the negative ones in blue.

Ion optical elements in TRIGA-TRAP are mainly deflectors and einzel lenses. The deflectors in use consist of a four-fold segmented cylinder. By a combination of voltages on the four segments, the ion beam can be deflected in any direction perpendicular to the beam axis. The einzel lenses consist of three cylindrical electrodes, where the first and last electrode are usually operated on the same potential, and the voltage on the middle part is used to define the focal length of the lens. In case the length and distance of the electrodes are chosen properly in respect to the diameter, a large variation of the focal length is achieved [Ada72].

All labels of ion transport elements, which are used in the following, are given in Fig. 4.3. Both ion sources have similar ion optics between their extraction and their 90°-bender. Behind the extraction plate a deflector (SIS-deflector / LIS-deflector) is used to tilt the ion beam, in case the ions are not extracted parallel to the beamline. In order to obtain a centered ion beam in forward-direction on the beamline, an einzel lens (SIS-lens 1 / LIS-lens 1) collimates the ions into the bender, in order to decrease the diameter of the beam inside the bender. Thereby a spread of the ion beam is avoided, because all ions experience almost the same electric field in the

bender. Between the two 90°-benders, there are two einzel lenses (LIS-lens 2 and 3) to keep the ions from the laser ion source collimated. The laser ion source can be separated from the remaining setup with a valve, if maintenance is required.

The space between the 90°-bender and the trap tube is bridged with the following elements: a pair of two deflectors (deflector 1 and 2), followed by two einzel lenses (lens 1 and 2) and another pair of deflectors (deflector 3 and 4). A third einzel lens (lens 3) is used to focus the beam into the magnetic field, where the Penning traps are located. A strong field gradient has to be passed, before reaching the maximum field strength inside the magnet of $B = 7$ T. Inside the magnetic field the ions move on a cyclotron orbit, thus a collimation of the beam is no longer necessary. Drift tubes are used to accelerate and decelerate the ions. Since the kinetic energy of the ions is quite large during the transport (about 1 keV), they have to be decelerated for trapping. Therefore three drift tubes are placed on the injection side (PDrift 1 to 3). On ejection side it is necessary for the TOF-ICR measurements that the ions move slowly through the magnetic field gradient, in order to have an adiabatic conversion of radial to axial kinetic energy (see Chap. 2.2.3). To this end ten drift tubes (Drift 0, 1, 2a, 2b and Drift 3 to 8) are installed on the ejection side. Some of these drift tubes are located outside the strong magnetic field, so that a combination of three drift tubes can there be used as an einzel lens. An additional drift tube can finally be inserted (Drift 9) or be replaced using a particle detector by a linear feedthrough. To complete the list of transport electrodes, there is a funnel and a pumping barrier installed between the two Penning traps [Nei06, Nei07], where also a voltage is applied. These elements are discussed in the following chapter.

4.2 Double Penning-trap system

The heart of the setup are two Penning traps, the purification and the precision trap [Web04], in which the mass measurement is performed via the TOF-ICR or the FT-ICR method (see Chap. 2.2). Both traps are placed 20 cm apart from each other within a homogenous magnetic field of $B = 7$ T, provided by a superconducting magnet (MAGNEX "7.0 T, 160mm bore actively screened magnet system for ion trap application" [Mag03]). Presently, the Penning trap system is placed in a test setup, where the magnetic field has one large homogeneous region with $\Delta B/B = 2 \cdot 10^{-6}$ for the precision trap [Fer07], while the magnet of the on-line setup has two small homogenous regions of 1 cm^3 size and a homogenity of 1 ppm for the purification trap and 0.1 ppm for the precision trap in the specified distance.

The design and the commissioning of the traps were carried out in the context of the PhD thesis of Ch. Weber [Web04]. To have access to nuclides with low production rates, it is necessary to perform FT-ICR measurements, since the number of required ions for achieving a certain precision is much smaller. Therefore, the precision trap was especially designed to obtain a good signal-to-noise ratio, see Eq. (2.31). Since the ions move on a large radius for FT-ICR detection, the trap itself consists of hyperbolically shaped electrodes, to maintain a harmonic trap potential in a large region, which is not possible for a cylindrical trap. Besides the endcaps and the ring electrode, there are four correction electrodes to compensate field deviations from

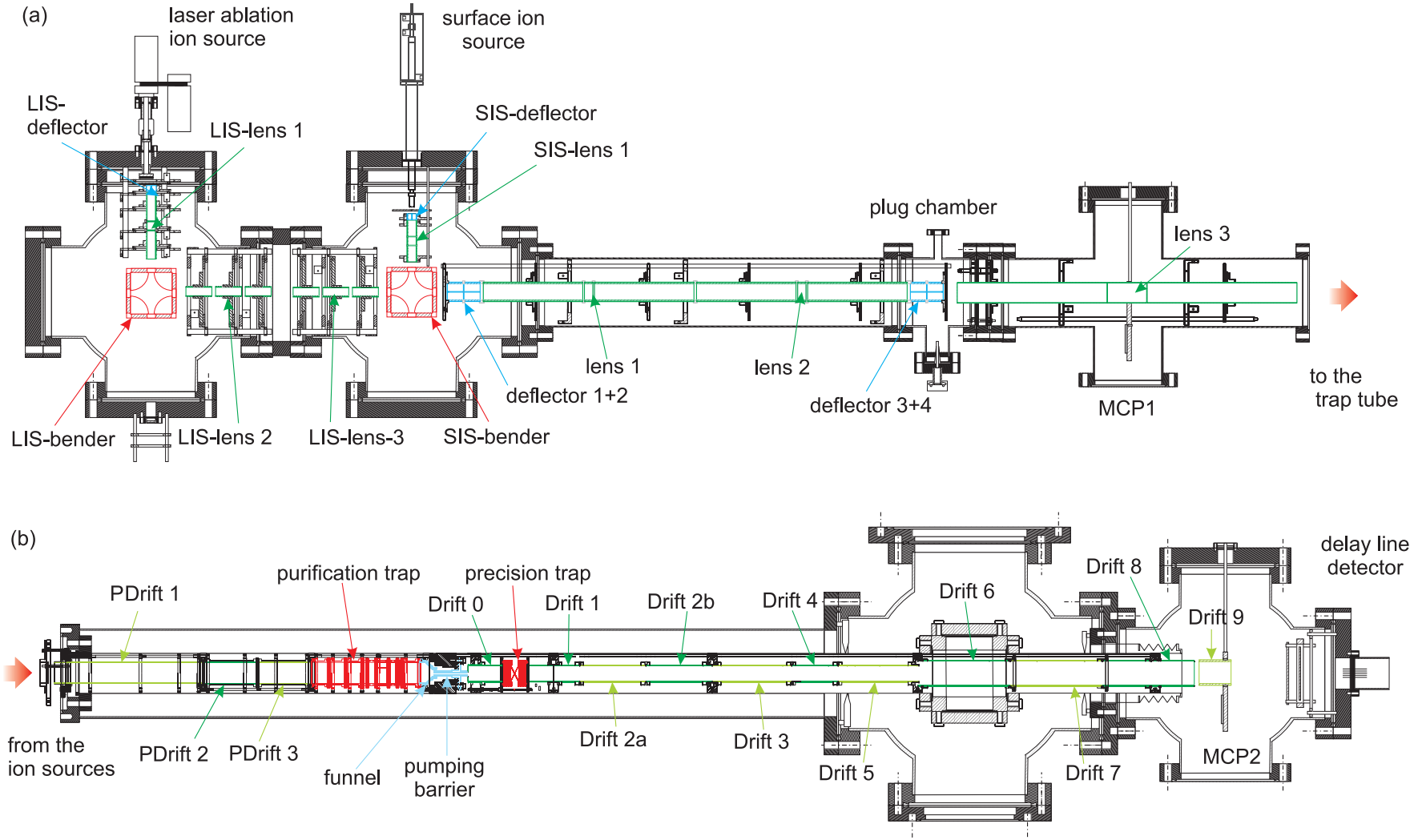

Figure 4.3: Overview of the ion optics in the TRIGA-TRAP setup. The ion source region is shown in (a). Lens elements are coloured in green, deflectors in blue and the 90°-benders in red. The trap tube is displayed in (b), where the drift tubes are coloured in green, the Penning traps in red, the funnel and the pumping barrier in blue.

the ideal configuration (see Fig. 4.4(a,c)). To increase the detection current the ring electrode is asymetrically splitted into four segments, 2 × 40° and 2 × 140°. The excitation is applied to the small segments, while the current is detected on the large segments. Furthermore, both traps are cooled down to 77 K via a thermal connection to the liquid nitrogen reservoir of the cryostat.

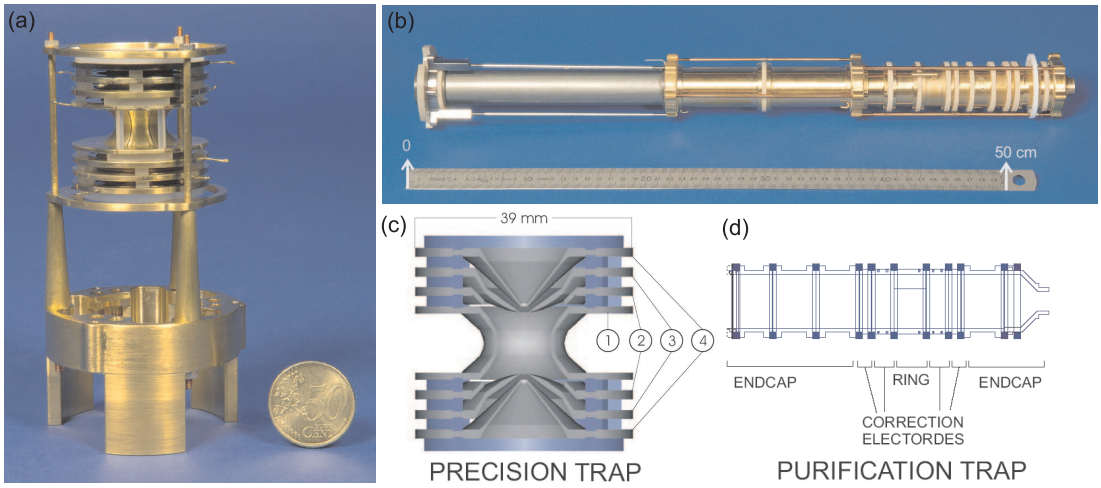

Figure 4.4: Cyrogenic Penning traps in the TRIGA-TRAP setup. The precision trap is shown in picture (a) and as a cut-away sketch in (c), where electrode (1) is the ring electrode, (3) the endcaps, (2) and (4) are the ring and the endcap correction electrodes. (b) shows a picture of the purification trap, assembled with three drift tubes at the entrance (left side). (d) shows a sketch of the electrode layout of the cylindrical trap.

The electrodes are made of high-purity oxygen-free electrolytic (OFE) copper in order to minimize the magnetic susceptibility μ of the used material, which would cause unnecessary inhomogeneties of the magnetic field (see Chap. 2.3) and also to guarantee a good thermal conductivity. Furthermore, the electrodes are first silver plated (5 - 10 μm) as a protection layer to avoid sintering of the 2 - 3 μm gold layer into the copper electrodes. The gold layer prevents oxidation of the trap surface, thereby avoiding potential differences, and thus, deviations from the harmonic trap potential. Small saphire parts are used to isolate the electrodes against each other.

The purification trap consists of seven cylindrically shaped electrodes: The ring electrode is asymmetrically four-fold segmented like the precision trap, inner and outer correction electrodes are used to compensate the errors in the trap potential due to the different geometry. The endcaps are on the entrance side three-fold and on the extraction side two-fold segmented (see Fig. 4.4(b,d)). The electrodes are also made of gold-plated OFE copper, separated by aluminium oxide (Al_2O_3) rings. For cooling and removing contaminations, buffer-gas cooling (see Chap. 2.2.2) is applied in the purification trap [Sav91], one endcap segment has a plug for the buffer-gas connection. Helium is inserted via a controlable needle valve (Pfeiffer Vacuum, EVR 116) to regulate the pressure.

Since buffer-gas cooling requires a gas pressure in the order of 10^{-5} mbar, the purification trap is separated from the measurement trap with a pumping barrier,

where both sides are evacuated by turbo molecular pumps (EBARA ET300WS). Thereby, a low residual gas pressure is maintained in the precision trap, in order to avoid damping of the ions' motion during a measurement procedure due to collisions with residual gas. The pumping barrier consists of a thin channel with a length of 47 mm and a diameter of 1.5, 2 or 3 mm, which is fixed on a cylindrical holder made of OFE copper. To avoid gas flow at the edges of the holder, it is pressed with a sealing ring into the vacuum hosting tube. With the smallest channel a relative pressure suppression of 1 to 6000 is achieved [Nei06, Nei07].

4.3 Detection systems

For particle detection, micro-channel plate (MCP) and channeltron detectors are used. Before the ion beam enters the superconducting magnet, the count rate or, in case of a pulsed beam, the number of ions per pulse can be investigated by replacing an Einzel lens segment with an MCP detector, both mounted on a linear feedthrough (MCP 1 in Fig. 4.1). Two movable masks with slits perpendicular to each other allow to investigate the position of the beam and thus to optimise the beam transport and the injection into the strong magnetic field.

For TOF-ICR measurements (see Sect. 2.2.3) another MCP on the ejection side of the traps (MCP 2 in Fig. 4.1) can be inserted into the beamline, or the particles are detected by a position resolving delay-line detector [Eit07]. Another possibility is to replace this detector by a channeltron detector.

Non-destructive particle detection is performed either broad- or narrow-band inside the two Penning traps, to analyse the trap content and to measure the mass of the trapped ions with the FT-ICR method (see Sect. 2.2.4). In the following, the operating principles of the different ion detectors in the TRIGA-TRAP setup are discussed.

Micro-channel plate detector

A mirco-channel plate detector is a detector for single particle detection. Similar to a secondary electron multiplier (SEM), an incident particle is detected by creating an avalanche of secondary electrons. The MCP itself consists of a plate of high-resistive

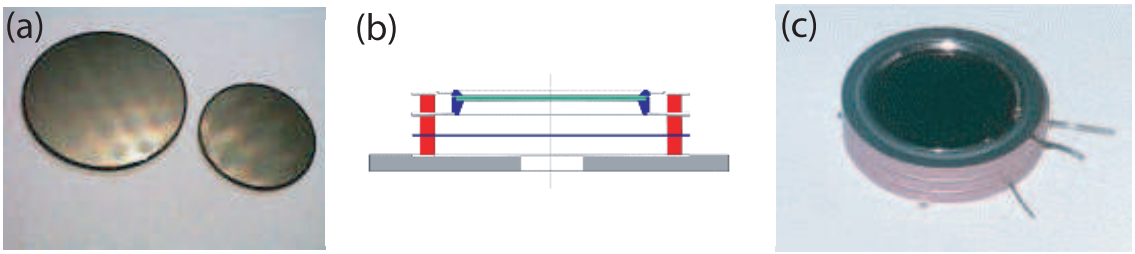

Figure 4.5: Two MCPs (a) and their setup in Chevron configuration (b). The two fitting plates (green) are placed on top of each other. Ceramic insulators (red) are used to isolate them against the read-out anode (blue). The assembled detector is shown in (c).

material, e.g. lead glass, with small parallel channels, in a hexagonal structure, where every channel has a diameter of 5 to 20 μm (see Fig. 4.5(a)). The channels are slightly tilted against the flight direction of the incident particles, typically 5° to 15°, to avoid particles passing the MCP without any interaction. Between the front and the back of the MCP a voltage of typically -1000 V is applied. If a particle hits the surface of the MCP and an electron is emitted, the electron is accelerated into the channel, producing more and more secondary electrons as they hit the wall. In principle each channel works as a single SEM with a gain of about 10^4 at a potential difference of 1000 V. To get a sufficient strong output signal, the Chevron configuration can be used, where two MCP plates are put on top of each other as shown in Fig. 4.5(b,c). Thereby a gain of 10^8 and a detection efficiency of 30-40% can be reached. This signal can then be read out by using a fast-timing preamplifier and an oscilloscope or a multi-channel analyser (MCA). Ions as well as neutral particles and photons with sufficient high energy can be detected with this kind of detector. The MCP has a very short dead time, about 10 ns, since each channel works as a SEM. This makes the detector very attractive for measurements having a high count rate or needing a good time resolution, as it is the case for the TOF-ICR measurements.

Position sensitive delay-line detector

To obtain a position information of the observed particles a commercially available delay-line detector (DET40 from RoentDec Handels GmbH) is employed. It consists of two MCPs placed in chevron configuration and a delay-line anode, which is able to achieve a two-dimensional position resolution of about 70 μm. The point, where the avalanche of electrodes produced by the MCPs hits the delay-line anode, is resolved by the difference between the propagation time of two readout wires in opposite directions. The signal can be used to access position information of the ion beam to improve the ion transport, or to separate contaminations in TOF-ICR measurements [Eit07].

Channeltron detector

Another type of an electron multiplier is the channeltron electron multiplier (CEM). A horn-shaped electrode made of high-resistive material (e.g. lead glass) is used to create an electron avalanche. A typical resistance of the channeltron horn is about 125-200 MΩ. To detect ions efficiently a voltage of -2.1 kV is applied across the horn. Thus, emitted electrons are accelerated into the horn and produce more secondary electrons by striking upon the surface, similar to a channel of the MCP detector. To avoid detection of photons and neutral particles the channeltron can be placed off-axis.

One major problem is that the detection efficiency is different for ions with different mass. Since the creation of electrons in surface impacts depends on the velocity of the incident particle, the detection efficiency decreases for heavier ions (assuming mono-energetic ions). By using a conversion dynode this mass dependency can be avoided. The conversion dynode is simply a metallic electrode on high negative

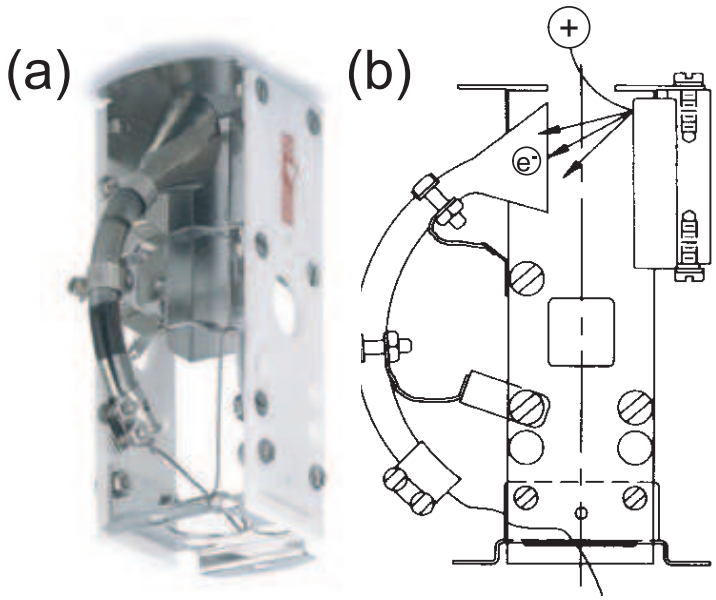

Figure 4.6: The DeTech 402 A-H channeltron detector in off-axis geometry is shown in (a), and (b) the detection of an ion by using the conversion dynode. Due to the potenial difference between the conversion dyonde (-4 kV) and the horn (-2.1 kV), electrons, created by ion impact, move into the horn and start an electron avalache.

voltage. Ions are accelerated by the negative voltage and strike upon the dynode, where they release electrons upon their impact. These electrons are then attracted into the channeltron and thus multiplied, as illustrated in Fig. 4.6(b). The gain of the channeltron is about $2{\cdot}10^8$, similar for all incoming particles. In this work, two different channeltron detectors of the type DeTech 402 A-H (see Fig. 4.6(a)) with different opening diameters of the horn (11.2 mm and 25 mm) were employed to detect ions. The characteristics of this channelron detector are compared to a typical MCP detector in Tab. 4.1.

The channeltron has the advantage that the detection efficiency is higher compared to the MCP. Above 90% can be typically reached for ions with a kinetic energy of about 2 keV [Bur07]. The dead time of the channeltron is larger, about 25 ns [Yaz06], but since the number of ions for Penning trap mass spectrometry is in the ideal case only a few ions per second, it is still suitable for this purpose.

FT-ICR detection

A non-destructive ion detection in the TRIGA-TRAP setup is carried out in both Penning traps, the purification as well as the precision trap. An ion bunch is guided into the purification trap, where it is analysed with a broad-band FT-ICR detection system to resolve different ion species delivered by the ion source. Since up to several hundred ions are present in the purification trap, the induced current (see Eq. (2.28)) is large enough to use room temperature amplifiers to convert the signal into a measurable voltage drop. Two amplification stages are operated at room temperature to obtain a signal of sufficient magnitude [Rep07]. After heterodyning

	two MCPs in Chevron configuration	channeltron detector (MODEL 402A-H)
typical gain	$5{\cdot}10^7$ at 2.5 keV	$2{\cdot}10^8$ at 2.1 keV
aperture plate size	d = 10 - 50 mm	d = 11.2 mm
dark counts	5 counts / s / cm^2	0.05 counts / s / cm^2
maximum count rate	10^8 / s	10^6 / s
impedance	66 - 400 MΩ	40 - 120 MΩ
operating pressure	$\leq 2{\cdot}10^{-6}$	$\leq 1{\cdot}10^{-6}$
raise time	$\approx$ 0.5 ns	$\approx$ 5 ns
pulse width (or dead time)	$\approx$ 2 ns	$\approx$ 25 ns

Table 4.1: Characteristics of the Channeltron detector (Model 402A-H) used in this work, and of two typical MCPs in Chevron configuration [Yaz06].

and filtering, the signal is digitalized and analysed by a Network Signal Analyser to obtain the frequency information of the ion motion.

In the precision trap a narrow-band FT-ICR detection system is used to precisely determine the cyclotron frequency of the captured ions. The development of the detection system was done in [Ket06]. Single ion sensitivity is required for the detection circuit. Two parameters can be optimised to obtain a good signal-to-noise ratio (see Eq. (2.31)): the Q-value of the tuned circuit, and the temperature T of the detection system. Therefore, the traps are cooled down to 77 K and the detection circuit is placed inside the cryostat at liquid helium temperature (4.2 K). To optimize the Q-value, the inductance of the detection circuit is build as helical resonator, consisting of a cylindrical single-layer air-core coil made of niobium-titanium (NbTi) wire, which is superconducting at 4 K and is placed inside a coaxial shield. The unloaded resonator has a Q-value of about 15000, the loaded resonator of about 1000 [Ket06, Fer07]. Two amplification stages are used to amplify the magnitude of the signal to a measureable value: a cryogenic amplifier, also placed in the cryostat to raise the signal amplitude above room temperature noise level, and a flange amplifier at room temperature. The further preparation of the signal for digital processing consist of heterodyning and filtering, similar to the broad-band detection system described above.

Chapter 5

Ion trajectory simulation studies with SimIon

The results of the simulation studies with the commercially available simulation software SimIon 8.0 are presented in this chapter. SimIon is an ion trajectory simulation code, in which the Laplace equation is solved for a defined electrode geometry by a numerical relaxation. The potential is approximated by the three dimensional potential array. Each array element represents a position in space with a potential value. The user has to define for each array element, whether it belongs to an electrode or not. The electric potentials on the electrodes are initially defined, for all 'non-electrode' points the electric potential is obtained by application of the relaxation method. To calculate the ions' trajectories a fourth-order Runge-Kutta iteration method is used [Dah00, Dah07].

The simulations require the following starting conditions of the ions: mass, charge, position, direction of momentum, and initial kinetic energy. A potential array is defined by a so called "geometry file". It contains the electrode geometry, which is defined by the creation of electrodes by unions and intersections of simple objects (e.g. cubes, cylinders, ...). A point-by-point definition of the potential array is also possible.

The simulations have been performed in order to obtain voltages for the ion transport from the surface ion source (see Sect. 3.1) through the complete TRIGA-TRAP setup (see Chap. 4), and also to compare time-of-flight values in the test setup for the different ion species for the analysis of the mass spectra obtained from the laser ion source, which will be discussed in Chap. 6.

5.1 Results of the ion transport simulations

The only information of the ion motion inside the TRIGA-TRAP apparatus, when the ion transport is concerned, is the number of counts detected by particle detectors at fixed positions in the setup. In case of the surface or the electron impact ion sources, both producing ion currents in the order of nA, it is also possible to measure currents on electrodes produced by ion impact. In order to understand the behaviour of the ions in the apparatus, a simulation of the transport voltages and the resulting ion trajectories is necessary. Thereby, optimal values for the voltages

on each electrode resulting in an efficient ion transport can be gained for a perfectly aligned apparatus. For comparison with the real setup, alignment errors such as a slight tilt or shift of some electrodes, which can be investigated by misaligning the electrode geometry in the simulation, have to be considered. Previously a different electrode design for the ion transport was in use, which was designed for a different magnet. This system was not suited for the ion transport with the test magnet. Simulation studies have been performed before commissioning and installing the new transport section. Additional deflectors and einzel lenses have been inserted, which are also able to correct alignment errors. These elements allow to shift the beam by two deflectors, tilt the beam by one deflector, and to prepare a parallel beam by two einzel lenses. The current electrode layout is shown in Fig. 4.1, and a three-dimensional view of the electrode geometry used in SimIon is given in Fig. 5.1. A complete list of all electrodes[1] of the TRIGA-TRAP setup from the surcface ion source to the position-sensitive detector is given in Tab. 5.1 and 5.2.

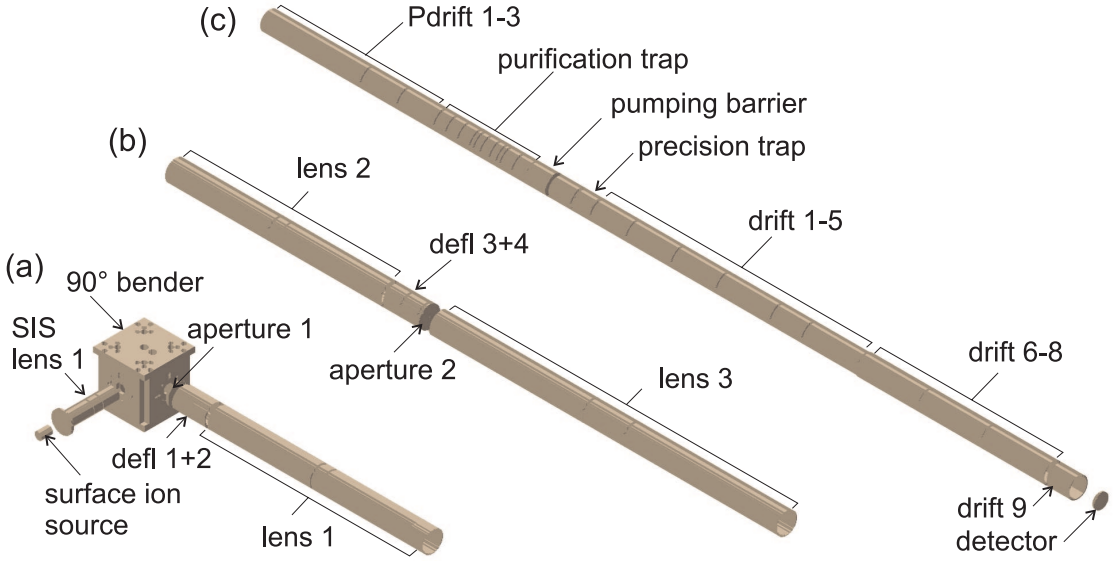

Figure 5.1: Electrode geometries of the potential arrays used for the ion transport simulation. (a) shows the ion source, which is in the experiment mounted on the other side of the bender, but the voltages on the bender electrodes are simply switched, (b) shows the transport tube, and (c) the trap tube, which is scaled down by a factor of 1.5.

The simulation consists of four different potential arrays, since the number of electrodes within a potential array is limited: the ion source potential array in Fig. 5.1(a), containing all electrodes from the surface ion source to lens 1, the transport tube potential array with the electrodes from lens 2 to lens 3 in Fig. 5.1(b), the trap tube potential array, with the remaining electrodes in Fig. 5.1(c), and one additional potential array, which contains the magnetic field of the superconducting magnet.

[1]The laser ion source is up-to-now installed in the test setup and not yet included in this simulation. Therefore, the electrodes of the laser ion source (see Sect. 3.3) are not listed here. An overview of the final setup in shown in Fig. 4.1.

description	l / mm	d / mm	U_{sim} / V	U_{max}/V
SIS energy	-	-	21	1100
SIS extraction	3.0	2.0	-2500	± 4000
SIS deflector up	9.0	13.0	-1000	± 4000
SIS deflector down	9.0	13.0	-1000	± 4000
SIS deflector left	9.0	13.0	-1000	± 4000
SIS deflector right	9.0	13.0	-1000	± 4000
SIS lens 1	25.0	13.0	-1000	± 4000
SIS lens 2	13.0	13.0	-2875	± 4000
SIS lens 3	25.0	13.0	-1000	± 4000
bender electrode 1	-	-	-135	± 4000
bender electrode 2	-	-	-1865	± 4000
bender correction	-	13.0	-1000	± 4000
bender housing	76.0	-	-1000	± 4000
aperture 1	2.0	2.0	-1000	± 4000
deflector 1 up	25.0	26.0	-1000	± 4000
deflector 1 down	25.0	26.0	-1000	± 4000
deflector 1 left	25.0	26.0	-1000	± 4000
deflector 1 right	25.0	26.0	-1000	± 4000
deflector 2 up	25.0	26.0	-1000	± 4000
deflector 2 down	25.0	26.0	-1000	± 4000
deflector 2 left	25.0	26.0	-1000	± 4000
deflector 2 right	25.0	26.0	-1000	± 4000
lens 1 - 1	154.4	26.0	-1000	± 4000
lens 1 - 2	13.0	26.0	-1500	± 4000
lens 1 - 3	154.4	26.0	-1000	± 4000
lens 2 - 1	154.4	26.0	-1000	± 4000
lens 2 - 2	13.0	26.0	-2275	± 4000
lens 2 - 3	154.4	26.0	-1000	± 4000
deflector 3 up	25.0	26.0	-1000	± 4000
deflector 3 down	25.0	26.0	-1000	± 4000
deflector 3 left	25.0	26.0	-1000	± 4000
deflector 3 right	25.0	26.0	-1000	± 4000
deflector 4 up	25.0	26.0	-1000	± 4000
deflector 4 down	25.0	26.0	-1000	± 4000
deflector 4 left	25.0	26.0	-1000	± 4000
deflector 4 right	25.0	26.0	-1000	± 4000
aperture 2	2.0	2.0	-1000	± 4000
lens 3 - 1	230.0	30.0	-1000	± 4000
lens 3 - 2	60.0	30.0	-2175	± 4000
lens 3 - 3	230.0	30.0	-1000	± 4000

Table 5.1: List of all electrodes of the surface ion source (SIS) and of the transport section. For each electrode the length l, the inner diameter d, the optimal voltage U_{sim} with two installed apertures, and the maximum voltage U_{max} are given.

description	l / mm	d / mm	U_{sim} / V	U_{max}/V
PDrift 1	224.5	34.0	-330	1000
PDrift 2	80.875	34.0	-330	1000
PDrift 3	80.875	34.0	-300	1000
PLE 1	25.25	34.0	0	1000
PLE 2	25.25	34.0	0	1000
PLE 3	25.25	34.0	0	1000
purification trap	58.625	34.0	0	1000
PRE 1	25.25	34.0	0	1000
funnel	25.25	14.0	0	1000
pumping barrier	50.0	3.0	0	1000
drift 0	51.6	7.0	0	1000
precision trap	33.4	1.8	0	1000
drift 1	79.0	24.0	0	1000
drift 2a	99.5	24.0	0	1000
drift 2b	99.5	24.0	0	1000
drift 3	119.5	24.0	0	1000
drift 4	69.5	24.0	-10	1000
drift 5	119.5	24.0	0	1000
drift 6	139.0	24.0	0	1000
drift 7	139.0	38.1	-30	1000
drift 8	139.0	38.1	0	1000
drift 9	50.0	38.1	0	1000

Table 5.2: List of all electrodes of the trap tube. For each electrode the length l, the inner diameter d (the smallest inner diameter in case of the funnel, drift 0, the precision trap, and drift 6), the optimal voltage U_{sim} with two installed apertures, and the maximum voltage U_{max} are given.

To calculate the magnetic field the code of J. Verdu [Ver03] was used, which calculates the magnetic field of two finite coils in Helmholtz configuration. The parameters of the coils were chosen so that the field matches the measured on-axis values in the homogeneous region as good as possible. The result is compared to the experimental data in Fig. 5.2. The field does not exactly match the experimental conditions, since a superconducting magnet for ion traps contains usually several correction coils besides the main coils to archieve a good homogeneity in the region of the ion traps. Furthermore, the magnetic field is not symmetric to both ends of the test magnet, since the homogeneous region of the trap is placed off-center, so that the shielding material inside the housing of the superconducting magnet causes a slight asymmetry.

To simplify the geometry of the trap tube, (i) the precision trap has been approximated by a cylinder with two holes for ion in- and ejection, and (ii) the ring electrodes of both traps are not segmented, which is of no cencern for the ion transport. Critical points in the simulation are borders between two potential arrays, since the border of a potential array defines a boundary condition for the solution of the Laplace equation. Thus, electrodes at the egdes of neighbouring arrays should

be on the same potential to avoid errors, since the electric field between electrodes in different potential arrays is not calculated.

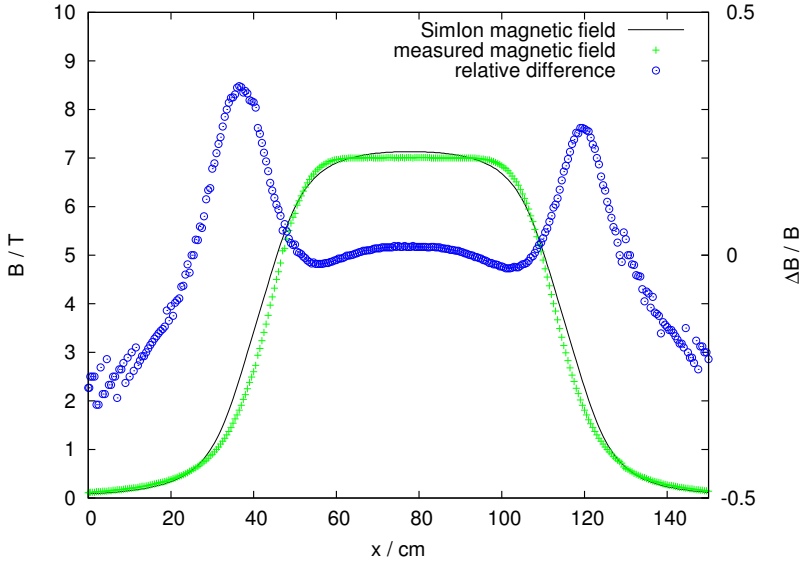

Figure 5.2: Measured magnetic field of the superconducting test magnet [Fer07] (crosses) compared to the calculated magnetic field of two finite coils in Helmholtz configuration [Ver03]. The parameters of the coils were chosen in a way to approximately fit to the measured values in the homogeneous region of the superconducting magnet. The deviation between the simulated and measured field is plotted as open circles.

In the simulation, ^{133}Cs ions are produced from the surface ion source (see Sect. 3.1) to investigate the transmission efficiency ϵ_T without trapping the ions. The starting conditions are generated with a C++ programme, which creates a homogeneous distribution of 10000 ions and a thermal velocity distribution corresponding to $T = 1300$ K within the hot cavity of the ion source. Due to their starting conditions some ions hit the cavity and are lost, while the remaining ions are ejected from the source in form of an ion beam.

In order to align the ion beam easily in the center of the tube, apertures with a 2 mm bore have been installed before deflector 1 and behind deflector 4 (see also Fig. 5.1). Because of the off-axis geometry of the ion source neutral and secondary particles, which are created before the aperture, are unable to reach the detector. On the other hand, these apertures limit the ion transport, beacuse the focal points of the transport optics have to be at the apertures' position in order not to lose too many ions.

The results are presented for two different simulation settings: (a) without installed apertures (see Tab. 5.3) and (b) with installed apertures (see Tab. 5.4). 'ejected ions' represents the number of ions which left the source, 'extracted ions' which passed through the extraction hole, 'detected ions' which reach the corresponding position. The extraction efficiency ϵ_E is the ratio of 'extracted ions' to 'ejected ions' and the transport efficiency ϵ_T the ratio of 'detected ions' to 'extracted ions'. Thus, the transport efficiency represents the quality of the ion transport, the

extraction efficiency is considered to be defined by the ion source. The number of initally required ions for a measurement procedure is defined by the fraction of ions which reach the position-sensitve detector (see Fig. 4.1) at the end of the setup. Furthermore of interest is the fraction of ions, which is available for trapping in the purification and in the precision trap, also listed in Tab. 5.3 and 5.4. The uncertainty in the number of ions at the different positions is given by the standard deviations of the binominal distributions, the uncertainties of ϵ_E and ϵ_T are obtained by the propagation of uncertainties.

desciption	n	$\epsilon_E \cdot \epsilon_T$	ϵ_T
overall	10000		
ejected ions	3378±47	100.0%	
extracted ions	2023±40	$59.9\% \pm 1.5\%$	100.0%
purification trap	1975±40	$58.5\% \pm 1.4\%$	$97.6\% \pm 2.8\%$
precision trap	490±22	$14.5\% \pm 0.7\%$	$24.2\% \pm 1.2\%$
detector	472±21	$14.0\% \pm 0.7\%$	$23.3\% \pm 1.1\%$

Table 5.3: Simulation results of the ion transport without apertures. The number of ions n, the overall efficiency $\epsilon_E \cdot \epsilon_T$, and the transport efficiency ϵ_T at different positions in the setup of the ion beam are presented. The initially available number of ions for the ions transport is defined by the number of 'extracted ions'. If the extraction efficiency ϵ_E is included, the initially available number of ions is given by 'ejected ions' (see text for details).

desciption	n	$\epsilon_E \cdot \epsilon_T$	ϵ_T
overall	10000		
ejected ions	3357 ± 47	100.0%	
extracted ions	2022 ± 40	$60.2\% \pm 1.5\%$	100.0%
aperture 1	1265 ± 33	$37.7\% \pm 1.1\%$	$62.6\% \pm 2.1\%$
aperture 2	853 ± 28	$25.4\% \pm 0.9\%$	$42.2\% \pm 1.6\%$
purification trap	828 ± 28	$24.7\% \pm 0.9\%$	$40.9\% \pm 1.6\%$
precision trap	169 ± 13	$5.0\% \pm 0.4\%$	$8.4\% \pm 0.7\%$
detector	161 ± 13	$4.8\% \pm 0.4\%$	$8.0\% \pm 0.6\%$

Table 5.4: Simulation results of the ion transport with two installed apertures. The number of ions n, the overall efficiency $\epsilon_E \cdot \epsilon_T$, and the transport efficiency ϵ_T are presented (see text for details).

Fig. 5.3 shows a 3D picture of the ion transport simulation. The most crucial parts where ions get lost are shown as insets. From the simulation studies the following observations are made:

- Ions are lost at the extraction plate due to the large emittance of the ion source. The extraction efficiency ϵ_E is about 60%.
- In case no apertures are installed almost all ions (98%) reach the purification trap. With installed apertures, the transport efficiency is reduced to 40% due to losses at both apertures.

- The most crucial parts in the setup for the ion transport are the pumping barrier with a diameter of 3 mm and the precision trap, with 1.5 mm diameter bores in the endcap electrodes, where a large fraction of the incoming ions are lost. Since the ions move through this part on a cyclotron orbit due to the magnetic field, the injection into the magnetic field by lens 3 has to be carefully adjusted. Due to Liouville's theorem the phase space volume an ion beam is constant in a conservative force field. Therefore, the diameter and the radial kinetic energy of the ions' motion cannot be decreased at the same time, so that a higher transmission through the pumping barrier and the precision trap is not possible. The transport efficiency into the precision trap is only 24% (8% with apertures).

- On the ejection side of the precision trap almost no ions are lost, so that the overall efficiency for the ideal setup is about 14% (5%).

During a mass measurement procedure the number of initially required ions of the nuclide of interest per ion bunch is defined by the overall efficiency of the apparatus, which includes in that case besides the transport efficiency also the trapping efficiency ($\geq 80\%$) and the detection efficiency (30-40 % for a MCP detector and $\geq 90\%$ for a channeltron detector [Yaz06, Fer07]), since in the ideal case at least one ion per bunch should be available for a measurement. Thus, a fraction of 3%-10% (1-4%) of the initially available ions can be used for a measurement, this requires about 10-30 (25-100) ions per bunch for a perfectly aligned apparatus. However, one should note that the transport efficiency through the pumping barrier and the endcaps of the precision trap is higher during a mass measurement procedure, since a large fraction of the incoming ions is captured and mass selectively cooled in the purification trap by means of buffer-gas cooling [Sav91]. Thereby energy is dissipated into the buffer gas leading to a centered and cooled ion bunch with low emittance.

The optimal voltages used in the simulation are listed in Tab. 5.1 and 5.2 for the simulation with two installed apertures. In the experiment aperture 2 was removed to capture ions in the purification trap. Tab. 5.5 compares the latest experimental voltage settings with the simulated ones with only aperture 1 installed. The voltages for the ion transport without apertures are given as well in Tab. 5.5. All electrodes in the transport section that are not listed are on -1000 V to accelerate the ions to about 1 keV for the injection into the magnetic field. In the trap tube they are decelerated to a few eV for trapping, the electrodes of the trap tube are therefore on ground potential.

The voltages applied to the einzel lenses match the simulated ones quite well. Deviations occur for SIS-lens 1 and lens 3. The latter has a slighty higher voltage than in the simulation, since the simulation was optimised for the transport through the whole setup, and the experiment for trapping in the purification trap. Applying the experimental voltage in the simulation increases only the diameter of the beam a little, so that more ions are lost at the pumping barrier and precision trap, but the number of ions reaching the purification trap is the same. The deviation of the SIS-lens 1 is probably caused by a misalignment of the 90° bender, also indicated by a deviation between the experimental and the simulated voltages applied to it. The experimental deflector voltages are between -950 V and -1000 V and are not

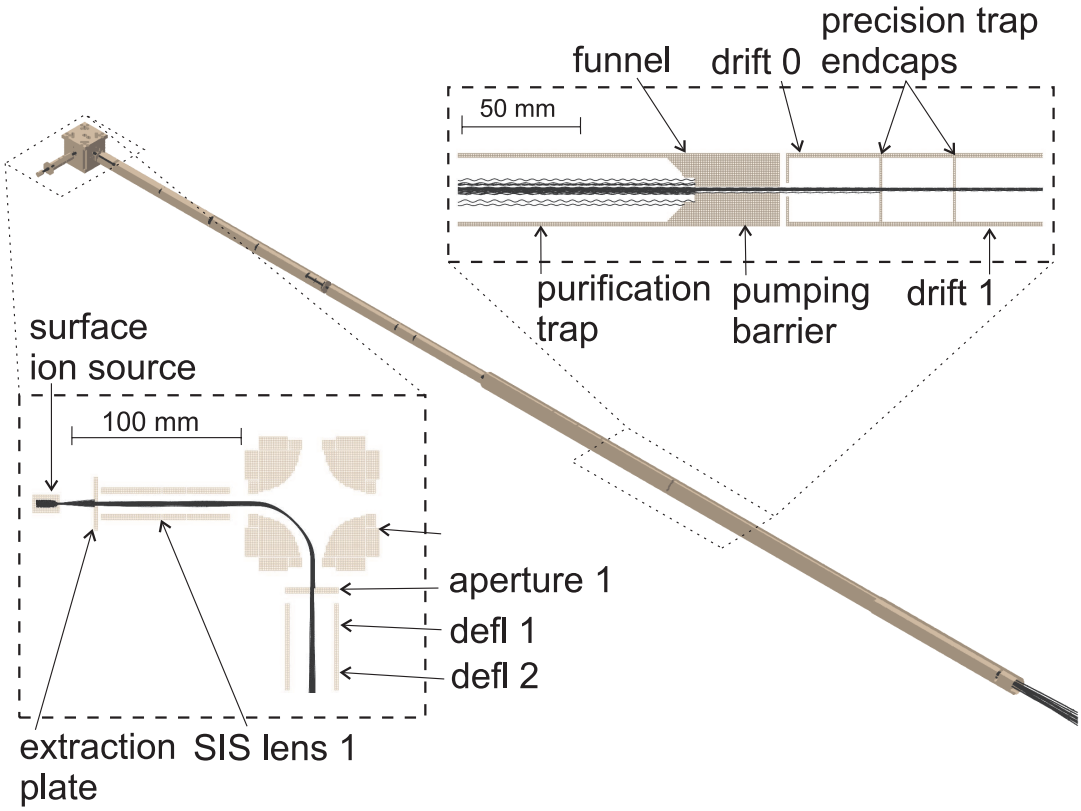

Figure 5.3: Ion transport simulation in the TRIGA-TRAP setup. Ion trajectories are displayed as black lines. The two insets show the region of the ion source and of the two Pennings traps. Ions are mainly lost at the extraction plate, at the apertures, at the pumping barrier, and at the endcaps of the precision trap.

presented here, since an ideal alignement of the setup was used in the simulation. An asymmetry in the deflector voltages decreases therefore the transport efficiency in the simulation.

Experimentally, the deflectors are used for the correction of alignment errors, e.g. a shift or a tilt between two eletrodes. In the experiment they cannot be avoided totally, since e.g. the 90° bender, which is mounted on a rotatable flange, has to be carefully positioned and the surface ion source gets tilted after heating due to thermal expansion. To correct these errors the count rate on the MCP detectors is maximised in dependence of the deflector and bending voltages.

As an example for an alignment error, the transport efficiency was simulated for a tilt of the bender in the bending plane of 3° and a shift of the transport tube in respect to the center of the bender. The results are presented in Tab. 5.6. Without any corrections no ion transport is achieved. By changing the voltages on the bender to -60 V and -1940 V (from -135 V and -1865 V, respectively) and appling -980 V to deflector 1 right (instead of -1000 V), these errors are corrected as good as possible, but the transport efficiency is still lowered by 25% in respect to the ideal setup.

In this chapter a complete overview of the ion optics of the TRIGA-TRAP setup was given for the first time. The optimal voltages for the ion transport have been obtained by ion trajectory simulation studies with SimIon and the transport effi-

Electrode	Voltage without apertures / V	Voltage with aperture 1 / V	Experimental voltages / V
Ion Energy	21	20	20
Extraction	-2500	-1600	-1600
SIS - Lens 1 - 2	-2812	-3300	-3600
Bender 1	-135	-135	+32
Bender 2	-1865	-1865	-2026
Lens 1 - 2	-2037	-2160	-2160
Lens 2 - 2	-1925	-2017	-2017
Lens 3 - 2	-2250	-1975	-2200
PDrift 1	-330	-330	-380
PDrift 2	-330	-330	-360
PDrift 3	-300	-300	-300
Drift 4	-10	-10	0
Drift 7	-30	-30	0
Transport section	-1000	-1000	-1000
Trap tube section	0	0	0

Table 5.5: Voltages used for the ion transport. The voltage listed as transport section is the voltage applied to the remaining unlisted electrodes up to lens 3, and the electrode "trap tube section" comprises the voltage for all unlisted drift tubes and trap electrodes.

desciption	n	$\epsilon_E \cdot \epsilon_T$	ϵ_T	n/n_{ideal}
overall	10000			
ejected ions	3378 ± 47.30	100.0%		
extracted ions	2023 ± 40.17	59.9% ± 1.5%	100.0%	
aperture 1	990 ± 29.87	29.3% ± 1.0%	48.9% ± 1.8%	78.3% 3.1%
aperture 2	641 ± 24.49	19.0% ± 0.8%	31.7% ± 1.4%	75.1% 3.8%
purification trap	613 ± 23.99	18.1% ± 0.8%	30.3% ± 1.3%	74.0% 3.8%
precision trap	122 ± 10.98	3.6% ± 0.3%	6.0% ± 0.6%	72.2% 8.5%
detector	122 ± 10.98	3.6% ± 0.3%	6.0% ± 0.6%	75.8% 9.0%

Table 5.6: Simulation results of the ion transport with two installed apertures and alignment errors. The bender is tilted by 3° in the bending plane and the transport tubes are shifted by 2 mm against the center of the bender. The number of ions n, the overall efficiency $\epsilon_E \cdot \epsilon_T$, transport efficiency ϵ_T, and the ratio of ions to those in the ideal setup n/n_{ideal} (see Tab. 5.4) are presented.

ciency through the whole apparatus was investigated. In the ideal case, the overall effeciency of the ion transport is 14% (or 5% with installed apertures), which is sufficient to provide ions for mass measurements. Alignment errors which cannot be totally avoided in the experiment lower the transport efficiency, even when corrections with deflectors are done. Thus, it is necessary to have a well aligned setup, since multiple alignment errors will further decrease the overall transport efficiency.

5.2 Time-of-flight simulation studies

For mass calibration the most important factor of the ion source is the availability of carbon clusters in a large mass range. Thus, it is necessary to analyse which kind of ions can be produced and extracted from the source. A possibility is to separate the ions with different m/q values by their different time of flight to a particle detector.

The time of flight of an ion with a certain mass-to-charge ratio m/q in an area with constant potential U of lenght s can be calculated by the following formula:

$$\tau = \sqrt{\frac{m}{2q(U_0 - U)}}s, \tag{5.1}$$

where U_0 is the potential of the ion creation region. In the setup the potential is not constant along the flight path since high voltages are applied to the different electrodes for the beam transport and for particle detection. Knowing $U(s)$ and the trajectory of the ion the time of flight is calculated to be:

$$\tau = \int_0^S \sqrt{\frac{m}{2q(U_0 - U(s))}}ds. \tag{5.2}$$

In order to separate ions of different masses, it is necessary to have a good mass resolution. Therefore, the energy spread of the ions has to be as small as possible to keep the time-of-flight distributions of the single ion species as narrow as possible. Furthermore, the mass resolution increases with a larger flight length. An analysis of the laser ion source output via time-of-flight separation has been performed in an off-line test setup (see Sect. 3.4), which contains the laser ion source, a channeltron detector and elements for the ion transport. The mass values to the corresponding measured time-of-flight values can be obtained by comparing the measured values to values predicted by Eq. (5.2). Therefore, a model of the test setup was created in SimIon 8.0, which is used to solve Eq. (5.2), since the exact trajectories of the ions and the potentials for a calculation are not known. A picture of the SimIon representation of the test setup in shown in Fig. 5.4, which includes the following electrodes:

- the target and the extraction system of the laser ion source
- the deflectors and einzel lenses for the ion transport
- the 6-way-cross and the holders of the electrodes

- the channeltron detector consists in the simulation of four electrodes: the conversion dynode, a plate at the front and at the back of the detector, and the channeltron horn, which is approximated by a cylinder at the opening of the horn, where the particles enter (see Fig. 5.4). An ion is considered to be detected and thus, to contribute to the time-of-flight value, if it either hits the horn approximating cylinder from the top or the conversion dynode, in case it is used.

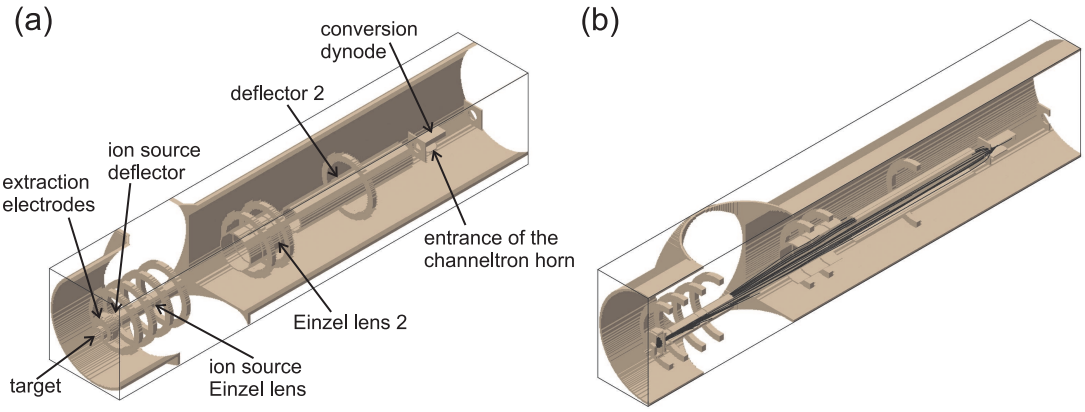

Figure 5.4: An 3D view of the electrode geometry of the test setup (see Sect. 3.4) is shown in (a), a cut-away view of the test setup is shown in (b), where the trajectories of C^+ ions are displayed as black lines. Applied voltages: target 250 V, extraction cylinder 70 V, extraction plate -1 kV, ion source einzel lens -220 V, einzel lens 2 -400 V, conversion dynode -4 kV, channeltron horn -2.1 kV.

For the time-of-flight prediction especially the distance between the source and the ion detector is a crucial parameter, which is measured to be $S = 57.5 \pm 0.3$ cm. An average time-of-flight value of each carbon cluster from C_1 to C_{60} is obtained by simulating 1000 ions of each species through the setup, the transport efficiency was between 17%-35%. An obtained time-of-flight spectrum, which contains the sum of the distribution for all cluster sizes, is plotted in Fig. 5.5(a). Experimentally, it is not possible to separate clusters larger than C_{20}, since the peaks of neighbouring clusters in the time-of-flight distribution are already too close to resolve them properly. In the simulation, the distribution for each cluster size can be extracted from the data (see Fig. 5.5(b)), thereby obtaining an average time-of-flight value for all clusters, which are used to obtain a fit function for ion identification. A Gauss function is fitted to the center of the time-of-flight distribution of each cluster size to obtain the center τ:

$$N(t) = A \exp^{-\frac{(t-\tau)^2}{2\tilde{\sigma}^2}}, \tag{5.3}$$

where A is the amplitude, and $\tilde{\sigma}$ represents the width of the distribution. The $1/e$ width is given by $\sigma = \sqrt{8}\tilde{\sigma}$, which is used as the uncertainty of the time-of-flight center τ.

The following fit function was applied to the simulation results in order to interpolate mass values between the test masses used in the simulation:

$$m_{ion}(\tau) = \alpha\tau^2, \tag{5.4}$$

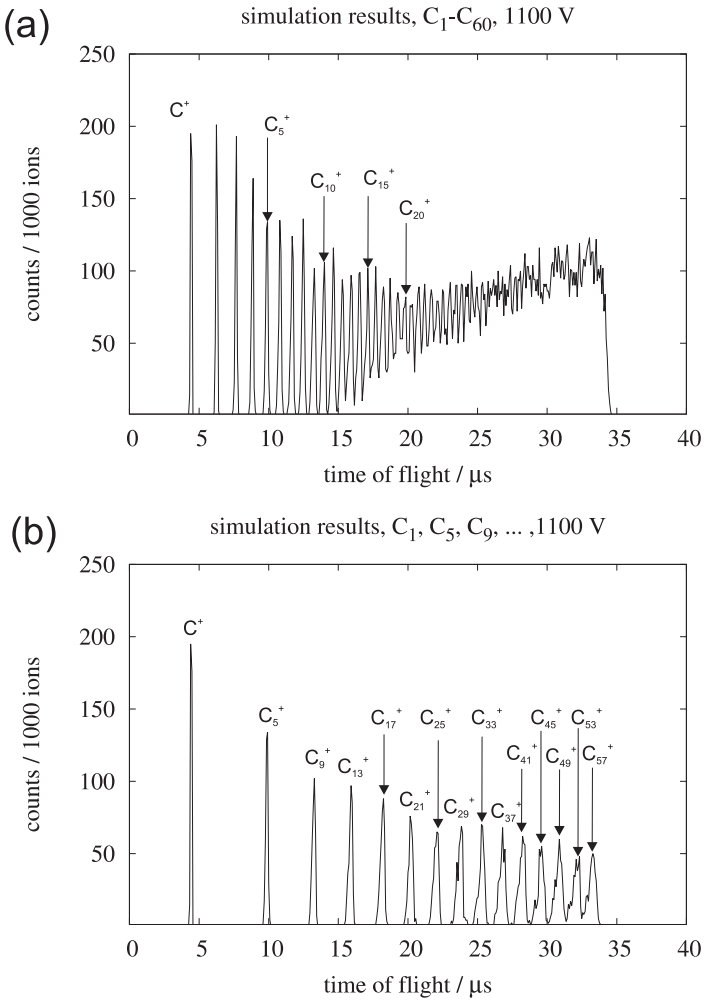

Figure 5.5: (a) The sum of the time-of-flight distributions obtained from SimIon simulations of the carbon clusters from C_1 to C_{60}. (b) Since clusters above C_{20} are not seperated in (a) the time-of-flight distribution for the clusters C_{4n+1} is shown, where all peaks can be clearly identified. For each cluster size 1000 ions have been simulated.

where α is the fit parameter, approximated for a straight uniform motion by:

$$\alpha = \frac{2eU_0}{S^2}, \tag{5.5}$$

where U_0 is the potential at the creation point of the ion. The starting parameters - angle and kinetic energy of the ions - have been estimated in respect to the experiment[2]. A uniform angle distribution and a Gaussian kinetic energy distribution with center values between 5 and 10 eV are used as an approximation. Since this energy is small compared to the energy gain due to the applied voltages (250 - 1100 V) on the target, the influence of the initial kinetic energy on the time of flight is neglected here. In case of the time-of-flight prediction for the C_{60} sample, the

[2]A pepper-pot emittance meter [Wit92] is currently under construction to determine the emittance of the ion sources.

target type	target voltage / V	α / (u / μs^2)
C_{60}	1100	0.61937 ± 0.00016
C_{60}	250	0.15228 ± 0.00008
other	1100	0.67218 ± 0.00007
other	550	0.34435 ± 0.00006
other	250	0.16276 ± 0.00009

Table 5.7: Fit parameter α (see Eq. (5.4)) required for mass calibration and ion identification in the test setup. Target type 'others' refers to all flat conducting targets, such as Sigradur or tungsten filaments.

simulation had to be modified, since the C_{60} pellet, which is inserted into a hole of the sample holder, is not conducting[3]. The grid points in the simulation, where the pellet is positioned, are replaced by non-electrode points, thereby the potential U_0 at the ions creation point is slightly modified. Fig. 5.6 shows the avarage time-of-flight values as data points and the corresponding fit functions. The obtained fit parameters, which are used for the on identification in the next chapter, are listed in Tab. 5.7.

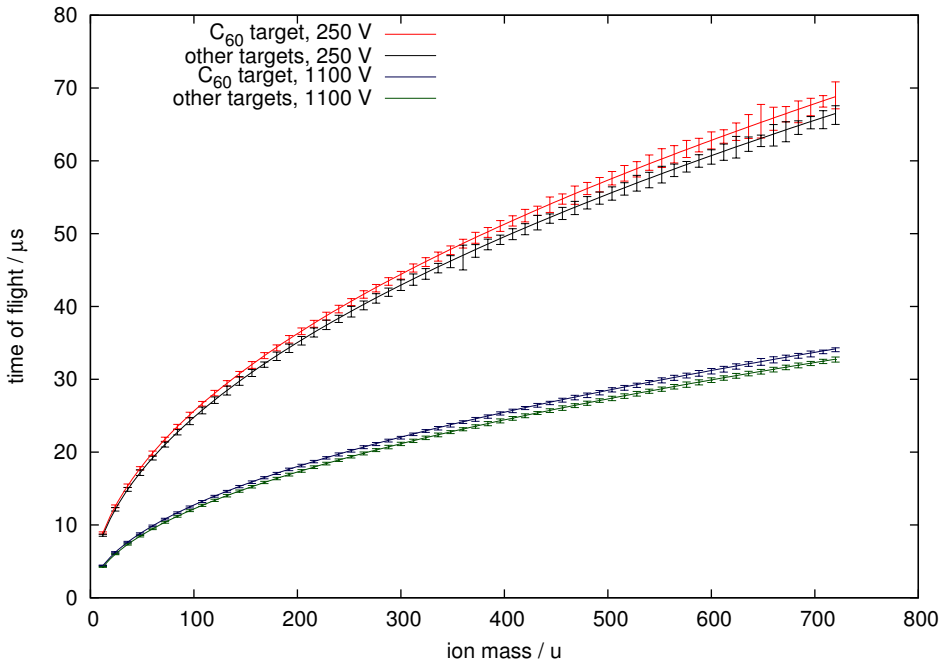

Figure 5.6: Simulation results for the time-of-flight values of carbon clusters from C_1 to C_{60} in the off-line test setup are plotted with the fit function in Eq. (5.4), which was applied to the corresponding simulation data. In case of the C_{60} target the ions are slower due to a lower acceleration voltage caused by the resistance of the C_{60} pellet (see text for discussion).

Furthermore, the peak shape of gadolinium was investigated, since gadolinium

[3]The voltage on the surface of the C_{60} pellet is < 1V, if a voltage (tested up to 250 V) is applied to the target holder.

has seven natural isotopes with similar abundances (see Tab. 5.9). In addition gadolinium is the chemical homologe of the heavy transuranium elements, which will be investigated in TRIGA-TRAP. Thus, many properties like ionisation efficiency can be studied off-line with a stable element. Gadolinium ions and also other ions which are expected from a gadolinium sample were simulated to obtain a time-of-flight distribution. Since gadolinium oxideses in contact with air, gadolinium oxide (Gd_2O_3) is also on the sample, and H^+, H_2O^+, Na^+, K^+ are expected as contaminations. GdO^+ is observed as well from laser ablated gadolinium samples [Mau04]. 10^4 ions were simulated of each ion species. In case of K^+, Gd^+ GdO^+, and $Gd_2O_3^+$ the mass distribution of the 10^4 ions was chosen in respect to the natural abundances of the elements. The result is shown in Fig. 5.7, and the mean time of flight τ and the 1/e width σ of the different ion species are listed in Tab. 5.8. As expected the width of the peaks of the gadolinium, GdO^+, and $Gd_2O_3^+$ ions is larger than the width of the monoisotopic elements due to two reasons: (a) the initial energy spread increases the width of the distibution for longer time of flights, and (b) due to the mass distribution according to the natural abundances of the used ions. In case of K^+ a similar width to H_2O^+ or Na^+ is observed, since the second stable isotope ^{41}K contributes only to 6.7%. In case of the ions of gadolinium (152 - 160 u) and its compounds GdO^+ (168 - 176 u) and $Gd_2O_3^+$ (352 - 368 u), the different isotopes of gadolinium contribute to the increased width of the peak. Due to the small flight distance, the isotopes are not separated and only a single peak is observed with and without the extension of the test setup. Considering the dead time of the channeltron detector in use (see Sect. 4.3) of about 25 ns, a separation is impossible, since an ion bunch contains multiple gadolinium ions, which arrive in a short time interval of only 150 ns.

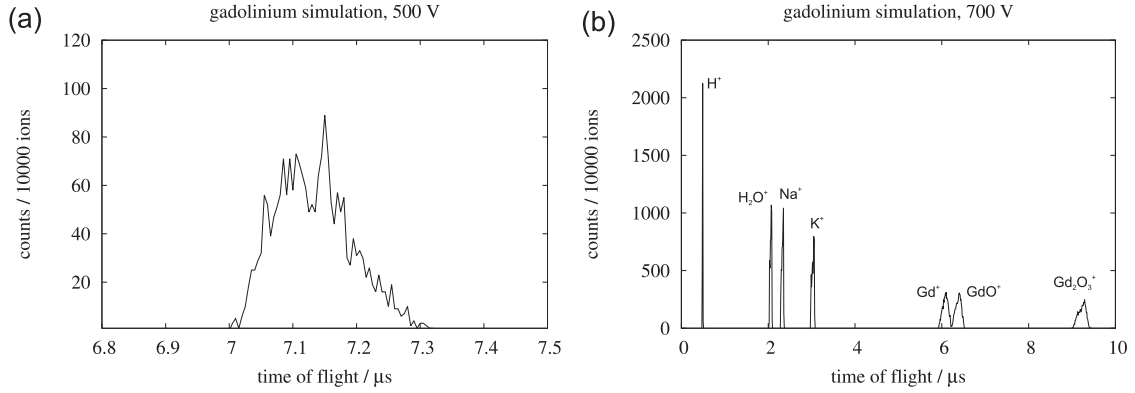

Figure 5.7: (a) Simulation of the time-of-flight distribution of gadolinium with natural isotope abundances and (b) the distribution of all expected gadolinium compounds and contaminations from a gadolinium sample.

In the following chapter, the fit functions and time-of-flight spectra obtained in this section will be used to assign ion species with mass-to-charge ratio m/q to maxima in the measured time-of-flight spectra. For each sample the comparison between experimental and simulation results is discussed.

Ion	m / u	n	τ / μs	σ / μs
H^+	1	1	0.49	0.01
H_2O^+	18	1	2.06	0.04
Na^+	23	1	2.33	0.04
K^+	39, 41	2	3.03	0.05
Gd^+	152−160	7	6.09	0.15
GdO^+	168−176	7	6.37	0.14
$Gd_2O_3^+$	352−368	15	9.24	0.18

Table 5.8: Simulation results for gadolinium samples. The ion species, the atomic mass m, the number of isotopes or the number of molecules with different atomic masses due to the isotope abundances n, the time of flight τ, and the 1/e width σ are listed.

Mass Number	Natural Abundance	Half-life
152	0.20%	$1.08 \cdot 10^{14}$ y
154	2.18%	Stable
155	14.80%	Stable
156	20.47%	Stable
157	15.65%	Stable
158	24.84%	Stable
160	21.86%	$1.3 \cdot 10^{21}$ y

Table 5.9: Stable gadolinium isotopes and their natural abundances[Nat07]. ^{152}Gd and ^{160}Gd are considered to be stable due to their long half-lifes.

Chapter 6

Experimental procedure and results

The most important property of the laser ion source concerning high-precision mass measurements is the possibility to generate carbon clusters as reference masses over a wide mass range in order to obtain reference ions all over the nuclear chart. The analysis of the ion species with different mass-to-charge ratios m/q extracted from the source is performed via their different time of flight to a particle detector. The investigations mainly focus on carbon cluster ions produced from Sigradur[1] and C_{60} samples, which are used as ions for mass calibration (see Sect. 2.3). Furthermore, gadolinium samples were investigated, which are of interest concerning the ionisation of heavy nuclides for mass measurements. The preparation of the samples for the laser ion source, the measurement procedure of the time-of-flight separation for ion identification (see Sect. 5.2), and the results of the analysis of the extracted ions are presented in this chapter.

6.1 Sample preparation

For the production of carbon clusters two different sample materials were investigated. Sigradur, also known as glassy carbon, is a solid state configuation of carbon with a fullerene-like structure with high thermal, chemical and physical stability and good conductivity. To obtain a suitable sample for the laser ion source, the commercially available plates with a thickness of typically 1-2 mm are cut into circularly-shaped samples with a diameter of 14 mm (see Fig. 6.1(a)). The other target material used for the ablation of carbon clusters is a powder of C_{60}. A small amount of isopropanol is added to the powder before it is pressed with a pressure of 130 kg / mm^2 to a solid pellet. A C_{60} pellet with a diameter of 7 mm was produced and investigated (see Fig. 6.1(b)). Pellets with larger diameter were not stable enough to use them for the laser ion source. Another possibility to get a C_{60} target is to deposit a solution of C_{60} in hexane on a substrate, e.g. tungsten, which will be discussed below. This thin surface layer of C_{60} delivers less cluster ions than the pellet. Thus, the pellet is favored as the sample material.

[1] Sigradur is a trade name of the HTW Hochtemperatur-Werkstoffe GmbH.

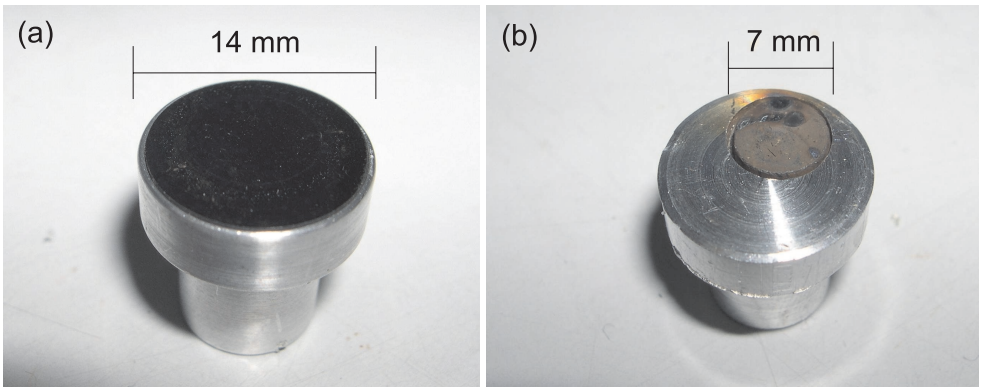

Figure 6.1: A picture of the Sigradur sample is shown in (a) and one of the C_{60} pellet in (b). Since a C_{60} pellet of larger diameter is not stable, the pellet has to be placed off-center, in order to bring it into the laser focus. Due to laser irradiation there are black spots on the surface of the pellet, where C_{60} clusters were desorbed.

To investigate the ion production of the heavy elements, which are the actinides from uranium to californium, studies with gadolinium being the chemical homologue of californium have been performed. Targets with different numbers of target atoms have been investigated in order to find the minimum number required for a reliable ion production. The samples were produced at the Department of Nuclear Chemistry at the University of Mainz. Two different methods for sample production were chosen:

1. Deposition: Gadolinium nitrate ($Gd(NO_3)_3$), or an actinide compound in case of the heavy elements, is dissolved in 0.1 molar nitric acid (HNO_3). About 10 μl of the solution are evaporated to dryness by means of an infrared lamp on a tungsten or titanium substrate. Thereby samples with 10^{11} to 10^{17} gadolinium atoms have been made.

2. Molecular plating: For molecular plating the gadolinium nitrate[2] is dissolved in a small volume (5-10 μl) of nitric acid and the aqueous phase is mixed with a surplus of an organic solvent (few ml), e.g. isopropanol, isobutanol, or acetone. Under these conditions no electrolytic dissociation occurs by applying an electric current at voltages up to 2000 V [Par62, Ebe04]. It is assumed that the dissolved molecules form clusters that migrate in the electric field towards the cathode. However, the deposition process is not yet completely investigated. In general, the composition of the deposition is complex and possibly containing also fragments of the solvent molecules.

In this work the results for gadolinium samples with 10^{17}, 10^{15}, 10^{13}, and 10^{11} atoms as well as the study of a gadolinium foil are presented. For these samples the gadolinium solution was deposited on a tungsten substrate with a diameter of 7 mm. The solution is placed in one spot with a diameter of about 3 mm off-center, at the position where the laser is irradiated.

[2]This method for sample preparation is also suited for compounds of the heavy elements.

The distribution of the gadolinium atoms on a substrate is made visible by irradiating neutrons from the TRIGA reactor to the gadolinium solution before deposition. Via the neutron capture process

$$^{158}Gd + n \rightarrow ^{159}\,Gd \tag{6.1}$$

the radionuclide ^{159}Gd is produced in a small amount, which has a half-life of $\tau =$ 18.4 h and decays in the following way:

$$^{159}Gd \rightarrow ^{159}\,Tb + e^{-} + \bar{\nu}_e. \tag{6.2}$$

An imaging plate, which is sensitive to β or γ radiation, is exposed to the sample for about 2-3 days, since the activity of the samples is quite low due to the small deposited amount of gadolinium. The imaging plate is read out with an imager (Fujifilm FLA 7000) to analyse the absorbed dose position-sensitively. The results are presented in Fig. 6.2. The advantage of the molecular plating is that a thin, homogeneous layer of gadolinium is adsorbed to the substrate, while for the deposition method the sample material is distributed on the surface in a very inhomogeneous way. Usually, the number of deposited atoms is much larger at the edge of the deposited spot than in the center (see Fig. 6.2(a)). The distribution of 10^{14} and 10^{12} gadolinium atoms on a titanium substrate is shown in Fig. 6.2(b) and (c), for a sample with 10^{10} gadolinium atoms the activity of the irradiated sample is too low (see Fig. 6.2(d)).

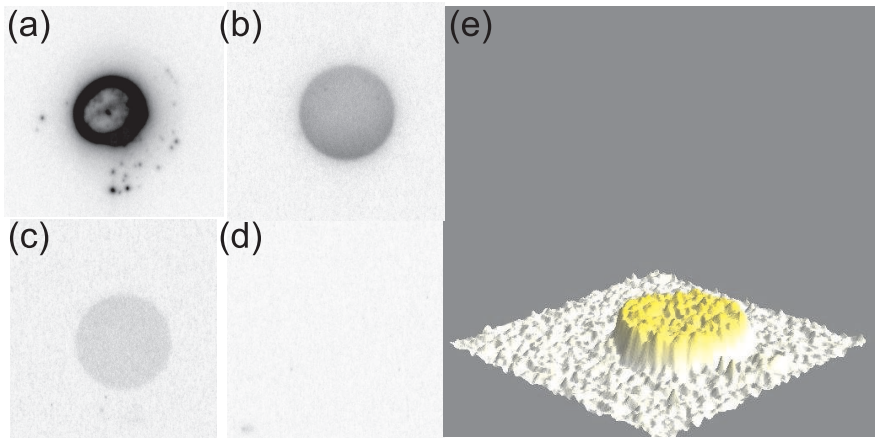

Figure 6.2: The distribution of gadolinium atoms on a titanium substrate are presented. A sample created by deposition of $3{\cdot}10^{14}$ gadolinium atoms is shown in (a), samples created by molecular plating with a homogeneous distribution of 10^{14} and 10^{12} atoms are shown in (b) and (c). The activity of the irradiated sample with 10^{10} Gd atoms was too low, the distribution of the atoms could not be detected (d). A surface plot of sample (c) is shown in (e).

6.2 Measurement procedure

In the following the measurement procedure to record the time-of-flight values for ion identification (see Sect. 5.2) is described.

The recorded spectrum in the test setup (see Sect. 3.4) consists of the time-of-flight values, which the ions require to the channeltron detector from the ion source. As start and stop trigger the laser pulse and the ion impact on the channeltron detector are used. The CS-control system [Bec04] is used to control the timing of the signals for a measurement procedure with a FPGA-card (National Instruments PCI-7811R FPGA RIO) and function generators (Agilent 33250A) are used for the amplification of the trigger pulses.

A typical measurement cycle, which is used to record the time difference between the two trigger signals is illustrated in Fig. 6.3 and proceeds as follows: The timing of the laser is controlled by two trigger pulses, one for the flashlamp and one for the Q-switch of the laser. Scanning the time delay between these two pulses can be used to optimise the power output. After the Q-switch trigger signal the laser pulse has a build-up time of about 60 ns before it is released. The ions produced by the laser at the target position are extracted by an acceleration voltage. The ion optics guide the ions to the channeltron detector, where they create a small voltage pulse which is amplified by a fast-timing pre-amplifier (Ortec VT120). To record the time difference between the start trigger, which is in this case the Q-switch of the laser, and the incoming signals from the channeltron detector, a multi-channel analyser (MCA, Stanford Reasearch Systems, SR 430) is in use. After recieving the start trigger, the MCA counts voltage pulses from the channeltron detector in bins with a defined bin width, which is typically 40-80 ns. In order to suppress noise, only voltage pulses are recorded with an amplitude above an certain discriminator threshold. Since the voltage pulses from the channeltron are negative, a signal is counted, if the input voltage drops below the discriminator threshold, which is typically -10 to -30 mV. Spectra of multiple laser pulses are summed-up with the MCA device to get better statistics for the time-of-flight distribution of the extracted ions. The mean time-of-flight of each peak in the spectrum is determined by a Gaussian fit.

For the determination of the corresponding mass-to-charge ratio m/q of ions with a certain time of flight τ, either a linear motion is used as approximation and the mass-to-charge ratio is calculated with Eq. (5.1) or the necessary fit function $m(\tau)$ is obtained from simulations studies (see Sect. 5.2).

Since the most stable carbon clusters are those with the lowest ionisation potential, namely clusters with atom numbers $n = 4k + 3$, with $k = 2, 3, 4...$ and $n < 30$ [Wur94], the cluster distribution can also be used as identification criterion. The ion species which are identified via this method can be used to obtain an empirical fit function $m(\tau)$ similar to Eq. (5.4), where the parameter α (see Eq. (5.5)) is adapted to the experimental data, corresponding to an adaption to the average kinetic energy of the ions during their flight to the detector.

6.3 Experimental results

Sigradur sample

A Sigradur plate (see Fig. 6.1(a)) was used for the investigation of the carbon cluster ions production by ablation with the laser ion source. Since Sigradur is a material with high thermal stability, it is necessary to shoot at the beginning laser pulses

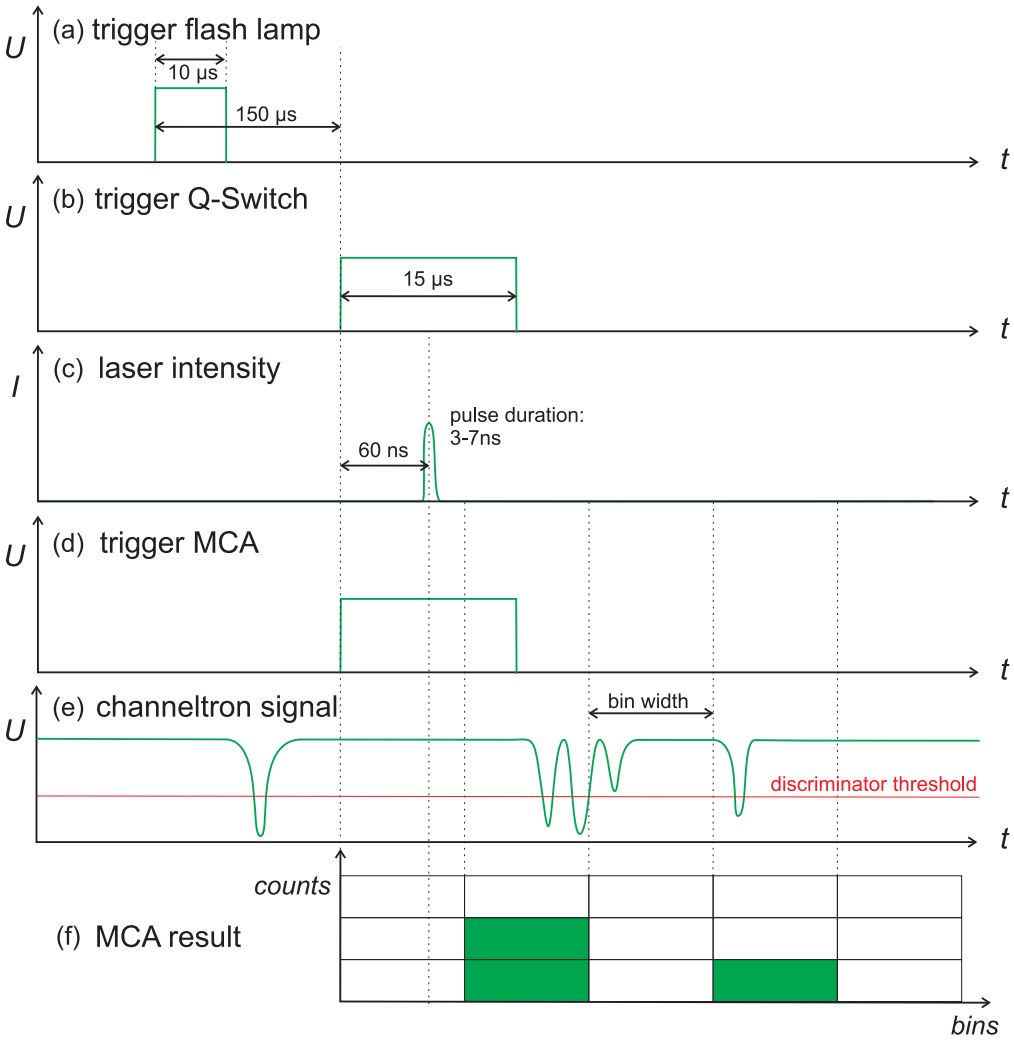

Figure 6.3: The timing of the signals for the measurement procedure is illustrated. For this purpose the time axis is not scaled. At first the laser is trigged by igniting the flashlamp and opening the Q-switch (a,b). The laser pulse has a build-up time of 60 ns before it is released (c). The MCA is triggered simultaneously with the Q-switch (d), and is used to count the events in the channeltron (e). Only signals below a certain discriminator threshold are able to trigger the MCA and are counted as an ion event (e,f).

with high pulse energies (about 30 mJ) on the surface, before carbon clusters can be observed. The laser pulse energy is the most crucial parameter, which influences also the carbon cluster distribution. To observe as many clusters C_n with different cluster sizes n as possible, the laser energy has to be lowered to about 6 mJ afterwards. Larger clusters are otherwise destroyed immediately after creation. For pulse energies lower than 5 mJ almost no cluster ions are observed from the sample. The result of a single measurement is presented as an example in Fig. 6.4, the obtained mass values are listed in Tab. 6.1.

The dependence of the cluster distribution on the buffer-gas pressure was also investigated by leaking in helium, thereby cooling the created plasma plume. The

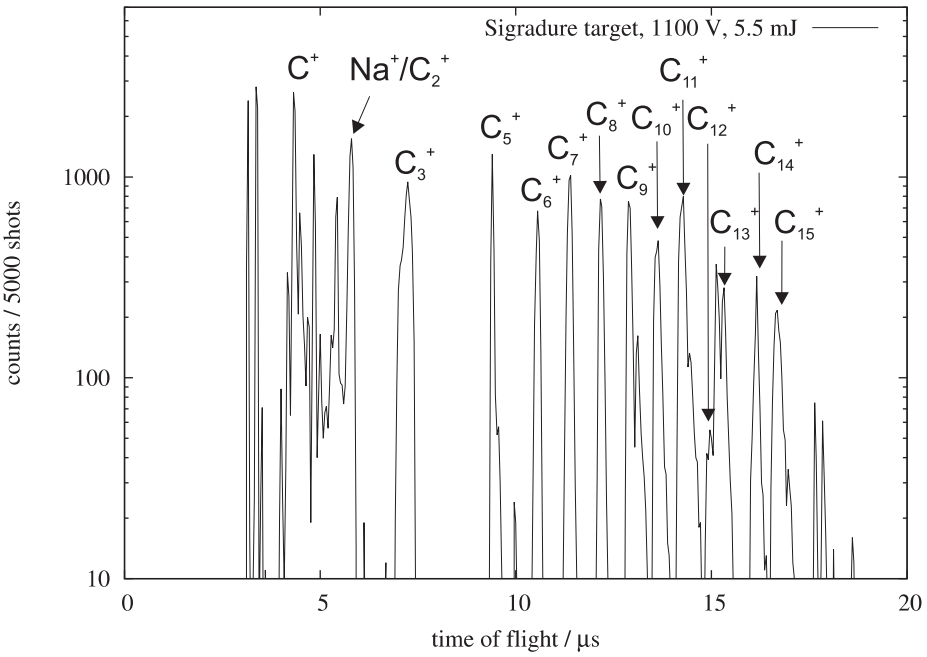

Figure 6.4: The number of counts in dependence of the time of flight for a Sigradur sample is shown in a logarithmic scale. A voltage of 1100 V was applied to the target and a laser pulse energy of 5.5 mJ was used. Carbon cluster ions up to C_{15}^+ are clearly visible. The obtained mass values are listed in Tab. 6.1.

maximum flow of helium was $1.5 \cdot 10^{-5}$ mbar/s, which lead to a pressure of $5 \cdot 10^{-6}$ mbar in the test setup. Higher flows of buffer gas were not tested in order to avoid a damage of the channeltron detector, which has an optimal operating pressure of $\leq 1 \cdot 10^{-6}$ mbar. Tests with a higher buffer-gas pressure can be performed in the TRIGA-TRAP setup (see Chap. 4), since the distance to the detectors is much larger and MCP 2 is even separated by the pumping barrier. The results of the measurement with the highest buffer-gas flow and highest background pressure is presented in Fig. 6.5.

Even with the maximum flow of buffer gas in use, there was no difference observed in the cluster production and distribution compared to the tests without buffer gas. We conclude that the pressure of the buffer gas was too low to observe any changes due to interactions between the ablated plasma plume and the buffer gas. Since similar results are obtained for both measurements (see Fig. 6.4 and Fig. 6.5), the measurement without buffer gas is discussed in the following, representing both measurements.

In Tab. 6.1 the mass-to-charge ratios m/q obtained from the measured time-of-flight values via the different ion identification methods are listed. During these measurements a voltage of 1100 V was applied to the target holder. The mass values for the straight uniform motion m_{lin} are lower than expected, since the average kinetic energy is higher than $eU = 1100$ eV due to electrodes on negative potential in the drift section. The average kinetic energy calculated from the fit parameter α (see Eq. (5.5)) in the simulation corresponds to 1159 eV. But the simulation results also deviate from the expectation, since the average distance between two assumed

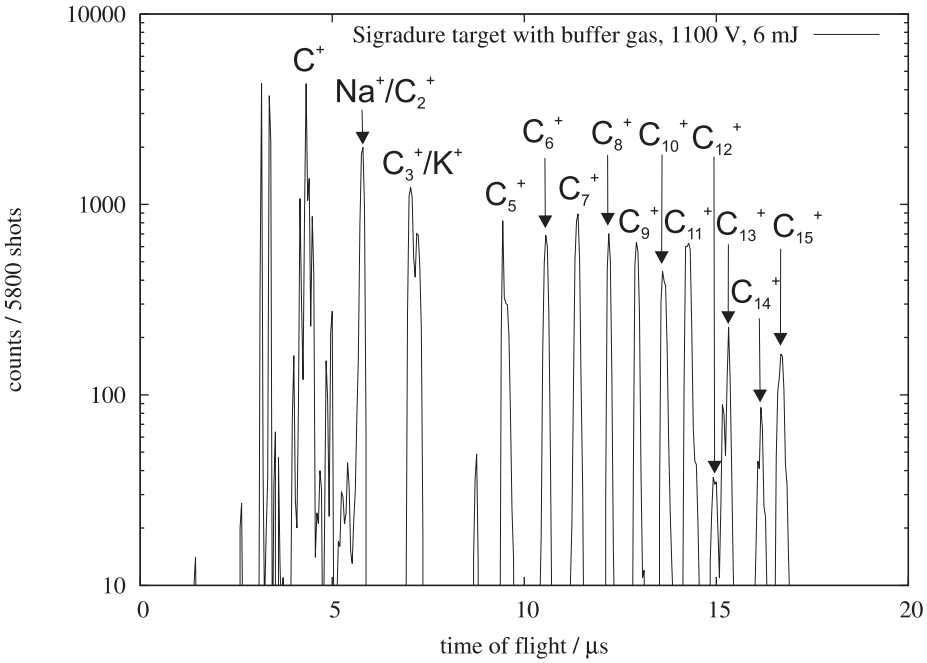

Figure 6.5: The time-of-flight distribution for a Sigradur sample with leaking in helium with a flow of $1.5 \cdot 10^{-5}$ mbar/s into the source is plotted in a logarithmic scale. A voltage of 1100 V was applied to the target and a laser pulse energy of 6.0 mJ was used. A result similar to the measurement without buffer gas is obtained (compare Fig. 6.4).

cluster ions is 12.7 u. Thus, the obtained mass values from the simulation m_{sim} are too high. For the calculation of the empirical fit function, the ions from C_6^+ to C_{11}^+ have been used for calibration in this case. The average kinetic energy obtained from this method is 1117 eV and the obtained mass values match the experimental results well. A possibility for the deviation of the simulation is that the ionisation of the ions occurs not immediately after laser irradiation. If the particle drifts away from the target surface before it is ionised, it sees a different potential for acceleration. A difference of the average kinetic energy of 42 eV between the simulation (1159 eV) and average observed kinetic energy (1117 eV), corresponds to a drift of 120-800 μm, depending on the mass and the kinetic energy of the particle after ablation, where 0.1-5 eV were assumed. In general, the simulation includes no plasma and particle interactions, which may also effect the time-of-flight, especially directly after the ablation. Further systematic errors of the simulation are discussed below.

In the mass region 6 u $< m <$ 40 u a large number of peaks are observed, which cannot be clearly assigned to an atomic or molecular species. In addition to the carbon cluster ions from C_1^+ to C_3^+, contaminations like H_2O, ^{23}Na, ^{39}K, etc. are expected in this region. An assignment of these peaks is difficult, since the deviation from the mass values of these expected ions is not within the error bars, except C^+. In case of C^{2+}, C_2^+ and C_3^+ the closest peaks have been assigned to these ions, in case of C_2^+ and C_3^+ the peak is probably a superposition of Na^+ and C_2^+, and K^+ and C_3^+, which results due to interactions in a shift of the time of flight. The maximum cluster size observed is $n = 15$. C_4^+ is not observed, probably due to a lower production

Ion	m/q in u / e	τ in μs	$(m/q)_{lin}$ in u / e	$(m/q)_{sim}$ in u / e	$(m/q)_{emp}$ in u / e
C^{2+}	6	3.16 ± 0.06	6.4 ± 0.1	6.7 ± 0.2	6.5 ± 0.1
??		3.38 ± 0.05	7.3 ± 0.1	7.7 ± 0.2	7.4 ± 0.1
C^+	12	4.34 ± 0.09	12.0 ± 0.2	12.7 ± 0.5	12.2 ± 0.3
??		4.85 ± 0.07	15.0 ± 0.2	15.8 ± 0.5	15.2 ± 0.2
H_2O^+		5.42 ± 0.09	18.7 ± 0.3	19.7 ± 0.7	19.0 ± 0.3
Na^+/C_2^+	23-24	5.79 ± 0.12	21.4 ± 0.4	22.5 ± 1.0	21.7 ± 0.5
C_3^+	36	7.21 ± 0.21	33.1 ± 1.0	34.9 ± 2.0	33.7 ± 1.0
C_5^+	60	9.40 ± 0.08	56.4 ± 0.5	59.4 ± 1.0	57.2 ± 0.5
$^*C_6^+$	72	10.56 ± 0.13	71.1 ± 0.9	74.9 ± 1.9	72.2 ± 0.9
$^*C_7^+$	84	11.38 ± 0.15	82.5 ± 1.1	87.0 ± 2.2	83.8 ± 1.1
$^*C_8^+$	96	12.18 ± 0.12	94.6 ± 0.9	99.7 ± 2.0	96.1 ± 1.0
$^*C_9^+$	108	12.91 ± 0.13	106.2 ± 1.1	112.0 ± 2.2	107.9 ± 1.1
$^*C_{10}^+$	120	13.63 ± 0.17	118.4 ± 1.5	124.8 ± 3.1	120.2 ± 1.5
$^*C_{11}^+$	132	14.26 ± 0.18	129.7 ± 1.6	136.7 ± 3.5	131.7 ± 1.7
C_{12}^+	144	14.96 ± 0.27	142.7 ± 2.6	144.9 ± 2.6	150.4 ± 3.9
??		15.14 ± 0.15	146.1 ± 1.5	148.4 ± 1.5	154.0 ± 2.2
C_{13}^+	156	15.32 ± 0.28	149.5 ± 2.7	151.9 ± 2.8	157.6 ± 4.1
C_{14}^+	168	16.15 ± 0.19	166.3 ± 2.0	175.3 ± 4.1	168.9 ± 2.0
C_{15}^+	180	16.70 ± 0.25	177.8 ± 2.7	187.4 ± 5.7	180.6 ± 2.7
??		17.65 ± 0.07	198.7 ± 0.8	209.5 ± 1.7	201.8 ± 0.8
??		18.62 ± 0.09	221.0 ± 1.1	233.0 ± 2.2	224.5 ± 1.1

Table 6.1: Evaluation of the measurement with the Sigradur sample shown in Fig. 6.4(a). The assumed ion species with the expected mass-to-charge ratios m/q, and the ratios calculated by assuming a straight uniform motion $(m/q)_{lin}$, by using the fit function from the simulation $(m/q)_{sim}$ (see Sect. 5.2), and by an empirical fit function $(m/q)_{emp}$ from the time of flight τ are listed (for a discussion of the deviations of the mass values see the text). Ions that were used to define the empirical fit function are marked with *.

rate (see discussion below), between C_{12}^+ and C_{13}^+ a thrid ion species is observed with $m/q \approx 146$ - 154 u, so that these peaks are not resolved completely.

In Fig. 6.6 a time-of-flight spectrum from [Bla03a] is shown. It is possible to create carbon cluster ions up to C_{23}^+ with a Sigradur sample, although the production probability is quite low for the clusters above C_{15}. For these measurements a different laser with higher intensity and smaller focus diameter was in use resulting in a higher power density and the mass resolution is much better, since the spectrum was recorded in a setup with a much longer flight length (2.50 m). In case of the carbon clusters C_3 and C_5-C_{11}^+ the count rate was limited due to saturation effects of the detector in use. The count rate of C_4^+ is although low compared to the neighbouring clusters, since C_4^+ does not saturate the detector. Due to their lower production rate C_4^+ and clusters heavier than C_{15} may not have been observed yet. Up-to-now reference ions from 12 up to 180 atomic mass units can be provided by this sample with the developed ion source. For measurements on heavy nuclides like

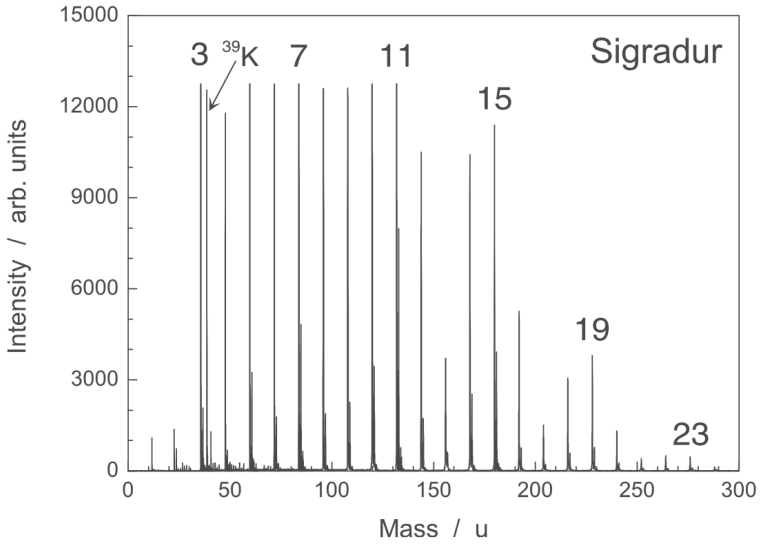

Figure 6.6: Time-of-flight distribution of a Sigradur sample [Bla03a]. In case of the carbon clusters C_3 and C_5-C_{11}^+ the count rate was limited due to saturation effects of the detector in use.

transuranium elements the cluster size is not sufficient to obtain suitable calibration masses, since calibration masses are required up to ^{252}Cf. A possibility to increase the cluster size may be to use much higher buffer gas pressures in the source and to decrease the diameter of the laser focus (see Chap. 3). Tests with a diameter below 0.9 mm have not been performed yet.

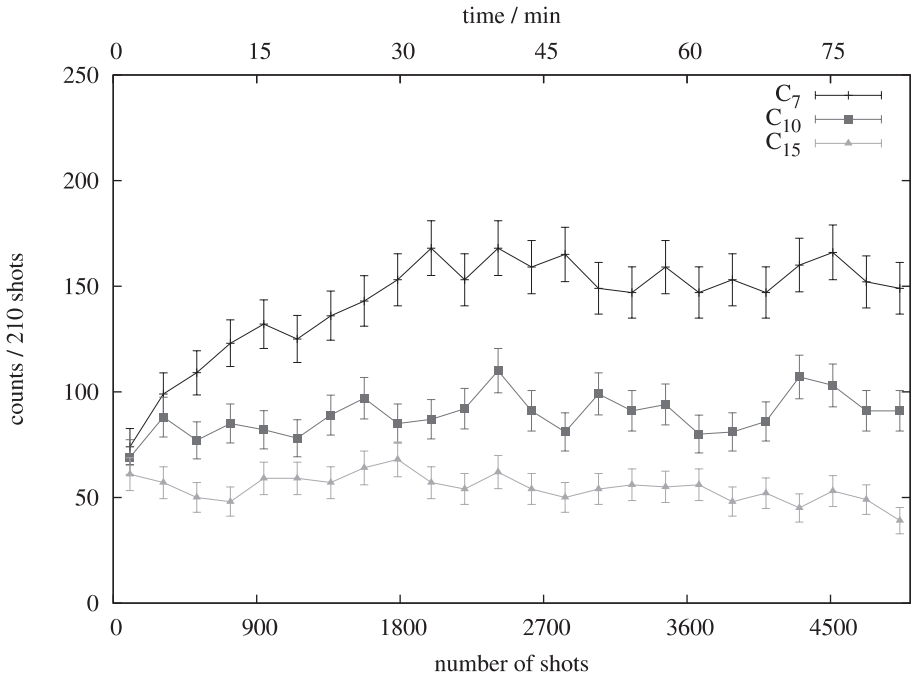

Figure 6.7: Counts of carbon clusters as function of the number of laser pulses for a Sigradur sample. C_7, C_{10} and C_{15} are plotted as example.

The carbon clusters can be produced from a Sigradur sample in a reliable way. The counts of carbon clusters as function of the number of laser pulses is plotted in Fig. 6.7 for C_7, C_{10}, and C_{15}. During this measurement the laser ions are produced from one spot on the target surface, i.e. the sample did not rotate. For 5000 laser pulses, which corresponds to a period of 1.5 hours with a repetiton rate of about 1 Hz of the laser, the ion source generated continuously ions, which is quite important for high-precision mass spectrometry where the number of stored ions should be constant 1-3 ions.

C_{60} sample

A pellet of C_{60} was used for the production of carbon cluster ions by ablation, fragmentation and ionisaton of the C_{60} fullerene. In previous investigatons of C_{60}^+ fragmentation with multiphoton ionisation, even-numbered fullerene-like fragments were observed for $58 \geq n \geq 32$ and clusters with $n \leq 30$ with a linear structure [Wur94]. The stability of the clusters has a minimum for C_{30}. A time-of-flight spectrum of a C_{60} sample obtained in [Kel03] is shown in Fig. 6.8. A similar result is to be expected in these measurements.

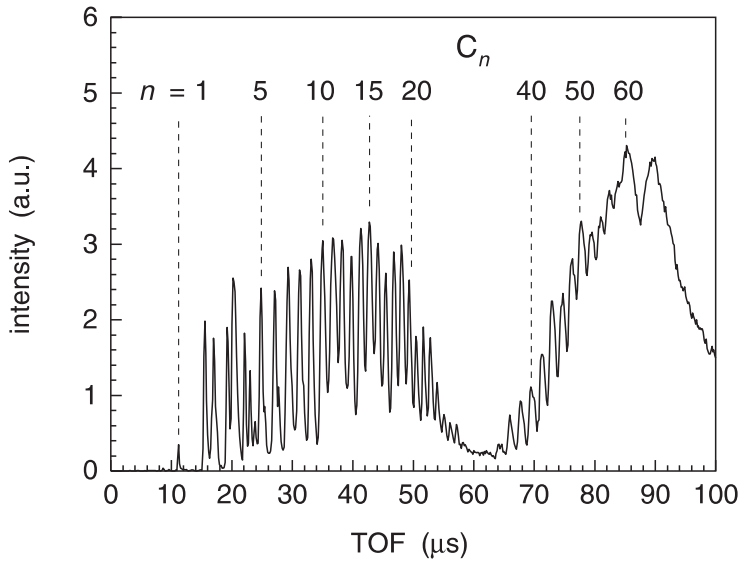

Figure 6.8: Time-of-flight distribution of a C_{60} sample [Kel03].

Compared to the Sigradur sample a lower laser pulse energy is required for the carbon cluster production, about 1.5-3 mJ in this case. Fig. 6.9 compares two time-of-flight spectra for different laser pulse energies. At low pulse energies the probability for the fragmentation of the C_{60} fullerene is small, so that mainly C_{60}^+ ions are observed. At higher pulse energies the carbon clusters created by fragmentation are observed.

A time-of-flight spectrum obtained from the C_{60} pellet with sufficiently high laser pulse energy for the fragmentation of the C_{60} fullerene to occur is shown in Fig. 6.10, and the time-of-flight values of some maxima of this measurement are listed in Tab. 6.2. Carbon cluster ions from C_1^+ to C_{23}^+ are observed. The fragments

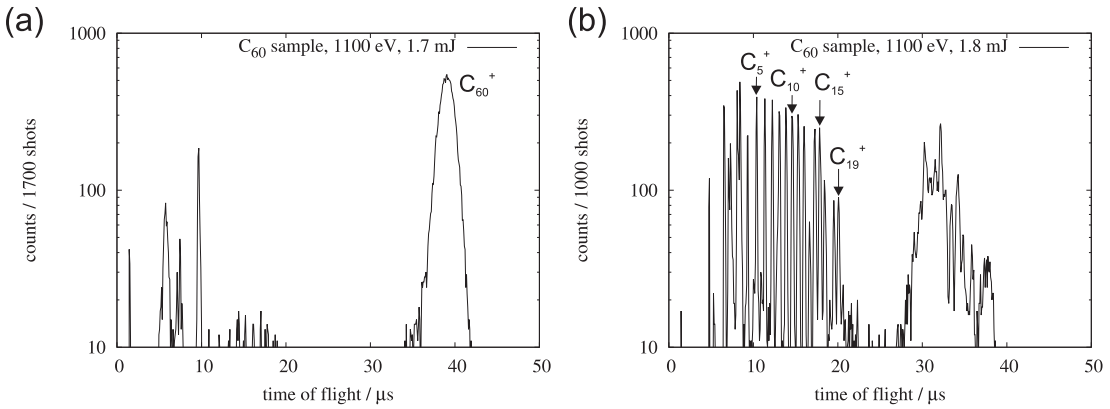

Figure 6.9: The number of counts in dependence of the time of flight for a C_{60} pellet is plotted in a logarithmic scale. Two measurements with a target voltage of 1100 V and similar ion optics settings are presented. In (a) mainly the ablation and ionisation of C_{60}^+ is observed, and in (b) the laser pulse energy is slightly above the fragmentation threshold.

with atomic sizes $24 \leq n \leq 48$ are missing in Fig. 6.10. The production rate is probably too low and the resolution of the apparatus is not good enough to separate the different clusters. Fullerene-like clusters with sizes $50 \leq n \leq 60$ are observed, similar to Fig. 6.8. Compared to the distribution in Fig. 6.8 only the clusters with atom sizes $27 < n < 36$ are not observed. This is due to the use of a mixture of C_{60} and C_{70} as sample material to enhance the production of the medium clusters sizes.

Concerning the ion identification, the approximation for a straight uniform motion is not shown in Tab. 6.2, since the potential at the ionisation location is not known. This is due to the fact that the C_{60} pellet is not conducting and thus not on the same potential as the target holder, where 250 V were applied in this case. Although the shape of the target holder was adapted for this sample in the simulation, the simulation predicts time-of-flight values which are much too short compared to the values for the clusters of size $1 < n < 23$. This leads to deviation of the average mass difference between two clusters of 15.1 u, which is 25 % too high.

If one assumes similar to the Sigradur sample a delayed ionisation of the particles, the ionisation position has already to take place outside of the extraction cylinder to obtain the measured time-of-flight values. Other reasons for systematic uncertainties in the time-of-flight prediction occur due to several reasons:

- The starting conditions of the ions cannot be exactly reproduced, since the creation of the plasma plume and interactions between ions, the laser, and the plasma plume are not included in the simulation process. Therefore, the angle and velocity distributions are only estimated.

- Alignment and positioning errors can occur, which lead to a deviation of the real and simulated electric field.

- It is difficult to include the channeltron detector (see Sect. 4.3) in the simulation, because it is made of a material with high resistance (lead glass), which creates a voltage drop along the horn-shaped detection electrode. Thus, the

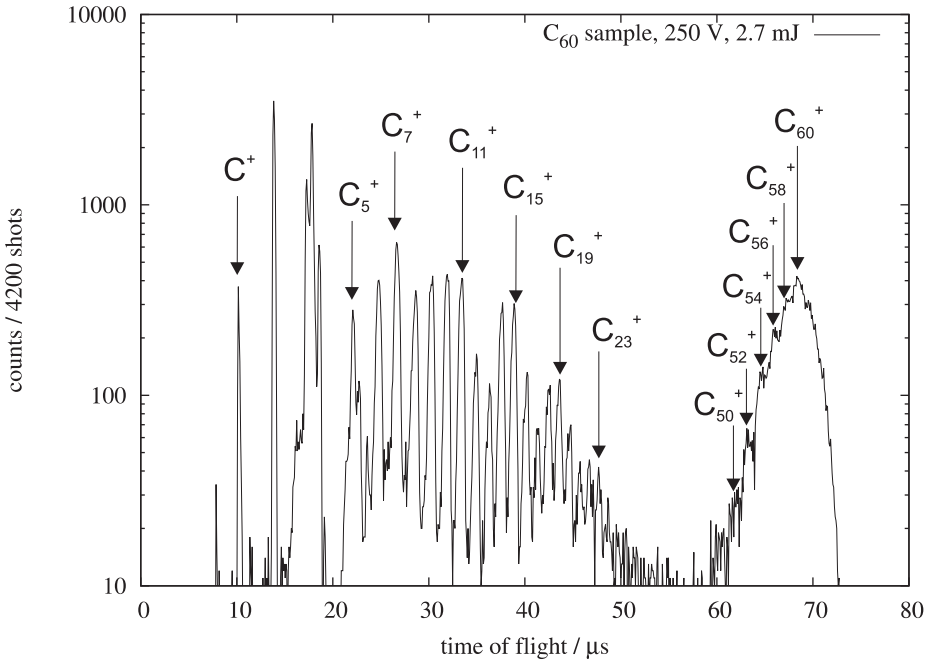

Figure 6.10: Time-of-flight distribution of ions extracted from a C_{60} pellet for a laser pulse energy of 2.7 mJ and a target voltage of 250 V. The counts are plotted in a logarithmic scale. Some mass values obtained from the time-of-flight values are given in Tab. 6.2.

electric field in the region close to the detector deviates from the experimental one.

- Deviations are caused due to interactions between the ions during their flight, which are also not included in the simulations.

- In case of the C_{60} pellet, the possibility of a delayed fragmentation of the C_{60} molecule and negative surface charges on the not conducting C_{60} pellet due to previous laser pulses have to be considered.

For the clusters with $1 < n < 23$ an empirical fit function, where the ions C_7^+-C_{17}^+ are used to determine α (see Eq. (5.4) and Eq. (5.5)), matches the measured values well. The average kinetic energy is only 194 eV compared to 261 eV, which are predicted by the simulation. Fullerene-like clusters with $n > 48$ are observed as well, but the time-of-flight values of the different clusters are too close together to observe separated peaks. From the simulation studies a mass value close to the mass C_{60} is obtained for the highest peak at $\tau = 68.32$ μs, but the empicial fit function predicts mass values which are much too small. A reason for this deviation is probably caused by interactions between the laser and the ablated plasma plume, which is discussed below (see discussion of the results of the gadolinium foil). It was observed that the average kinetic energy of the ions increases higher laser pulse energies W and with higher ion masses m, leading to shorter time-of-flight values for heavier ions. Since the average kinetic energy of the ions C_7^+-C_{17}^+ (194 eV) were in use to calculate the empirical fit function, this fit function seems to be not suited for ions

with much higher mass. If C_{60}^+ is assumed to be the fullerene-like carbon cluster ion with the highest abundance, an average kinetic energy of 265 eV is obtained. In the investigations of the gadolinium foil even higher differences between ions of different mass than 70 eV are observed. For this reason the highest peak of the fullerene-like carbon clusters is assigned to be C_{60}^+, which is also in agreement with previous investigations. If the ions are trapped in the Penning traps in the TRIGA-TRAP setup (see Chap. 4), the mass-to-charge of the ions can be determined with much higher precision and independent from the ions initial motion thereby confirming that the assignment is correct. For the C_{60} target an investigation of the dependance of the time of flight on the laser pulse energy is not possible, since the extracted ion species crucially depended on the laser pulse energy. Most of the ion species were only observable for a small range of W, where no major change in the time of flight was observed.

Ion	m / u	τ / μs	m_{sim} / u	m_{emp} / u
C^+	12	10.21 ± 0.23	15.9 ± 0.4	12.4 ± 0.3
Na^+/C_2^+	23-24	13.88 ± 0.26	29.3 ± 0.5	22.8 ± 0.4
		17.66 ± 0.91	47.5 ± 2.4	36.9 ± 1.9
C_3^+	36	17.80 ± 0.52	48.2 ± 1.4	37.5 ± 1.1
K^+	39	18.59 ± 0.33	52.6 ± 0.9	40.9 ± 0.7
C_5^+	60	22.22 ± 1.44	75.2 ± 4.9	58.4 ± 3.8
C_6^+	72	24.76 ± 0.72	93.4 ± 2.7	72.6 ± 2.1
$^*C_7^+$	84	26.67 ± 0.72	108.3 ± 2.9	84.2 ± 2.3
$^*C_{10}^+$	120	31.87 ± 0.61	154.7 ± 3.0	120.2 ± 2.3
$^*C_{15}^+$	180	38.83 ± 0.67	229.6 ± 4.0	178.5 ± 3.1
$^*C_{17}^+$	204	41.36 ± 1.14	260.5 ± 7.2	202.6 ± 5.6
C_{18}^+	216	42.47 ± 0.87	274.7 ± 5.6	213.5 ± 4.4
C_{19}^+	228	43.55 ± 1.24	288.8 ± 8.2	224.5 ± 6.4
C_{20}^+	240	44.58 ± 1.30	302.6 ± 8.8	235.2 ± 6.9
C_{23}^+	276	47.70 ± 0.92	346.5 ± 6.7	269.4 ± 5.2
C_{60}^+	720	68.32 ± 2.39	710.8 ± 24.9	

Table 6.2: Time-of-flight values from the measurement with the C_{60} sample in Fig. 6.10 are presented for some ions as example. Their calculated mass values m_{sim} from the simulation and m_{emp} from the empirical fit function are given as well.

The carbon cluster ion production with a C_{60} pellet is of interest to provide reference ions for the heavy elements, since more clusters up to C_{23} are available in a sufficient amount, compared to C_{15} as the heaviest cluster from a Sigradur sample. Thus, calibration masses up to a mass of 276 atomic mass units are available, which is already in the range of the element 112 and thus more than sufficient for the aims of TRIGA-TRAP. The reliability of the ion production with a C_{60} pellet is not as good as with a Sigradur sample. The laser penetrates the surface of the pellet after some shots, leaving a macroscopic hole in the sample. In Fig. 6.11 the counts of the carbon clusters C_{15}, C_{23} and C_{60} are plotted as function of the number of laser shots. After 1000 shots the count rate decreases and underlies strong fluctuations. In case the production rate is too low the pellet can be rotated to extend the operation time,

which may require an adjustment of the laser focus position and of the ion optics.

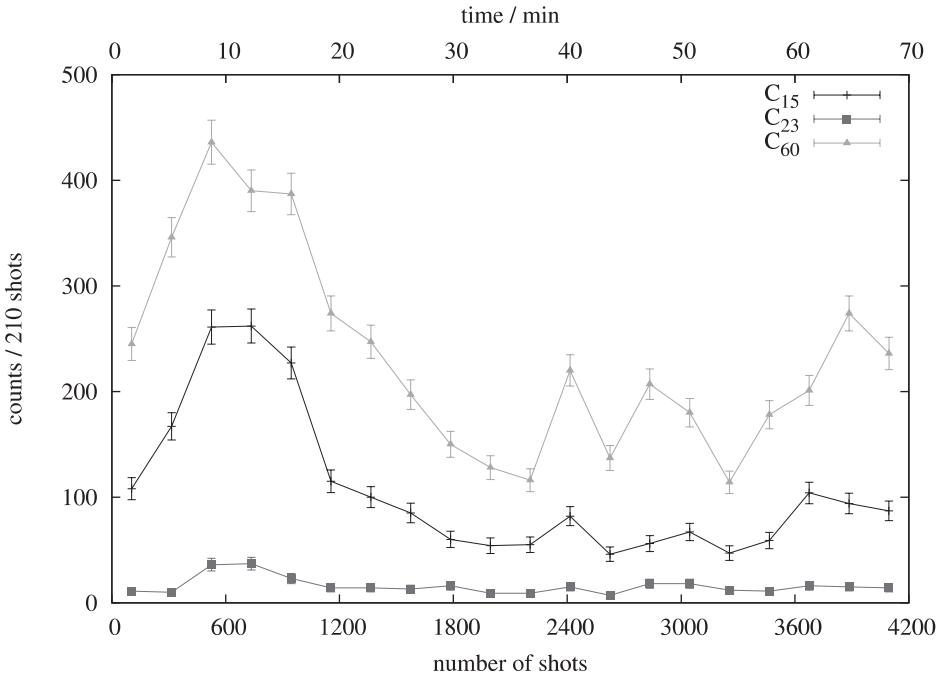

Figure 6.11: Counts of the carbon clusters C_{15}, C_{23} and C_{60} as function of the number of laser pulses for a C_{60} sample.

Tests with a gadolinium foil

First, a gadolinium foil (diameter 16 mm, thickness 0.25 mm) has been used to test whether gadolinium ions can be ablated and ionised with the laser ion source or not, before proceeding with deposited samples. The latter are the kind of samples available for the mass measurements on heavy elements. In Fig. 6.12 time-of-flight spectra taken with the gadolinium foil for identical settings of the ion optics and different laser pulse energies are shown.

The first observation in Fig. 6.12 is that the time of flight depends on the laser pulse energy W as already observed for the carbon clusters. The broad peak at τ = 19.73 μs with a FWHM of 0.52 μs in Fig. 6.12(a) (W = 4.8 mJ) was assigned to Gd^+ ions. The broader time-of-flight distribution can be explained by the natural abundances of the gadolinium isotopes (see Tab. 5.9). Up to a laser pulse pulse energy of 12.8 mJ in Fig. 6.12(d) the time of flight of the gadolinium ions has decreased by 15% to 16.86 μs. In Fig. 6.13 the average kinetic energy of Na^+, K^+, Gd^{2+} and Gd^+ calculated from the time-of-flight is plotted as function laser pulse energy. From this plot the following systematic trends are observed:

- The ions have higher kinetic energy at higher laser pulse energies W. The conclusion is that kinetic energy is transfered from the laser pulse to the ions, which is caused by interactions between the ablated ions in the plasma plume and the laser pulse. The difference in kinetic energy between 4.8 mJ and 12.8

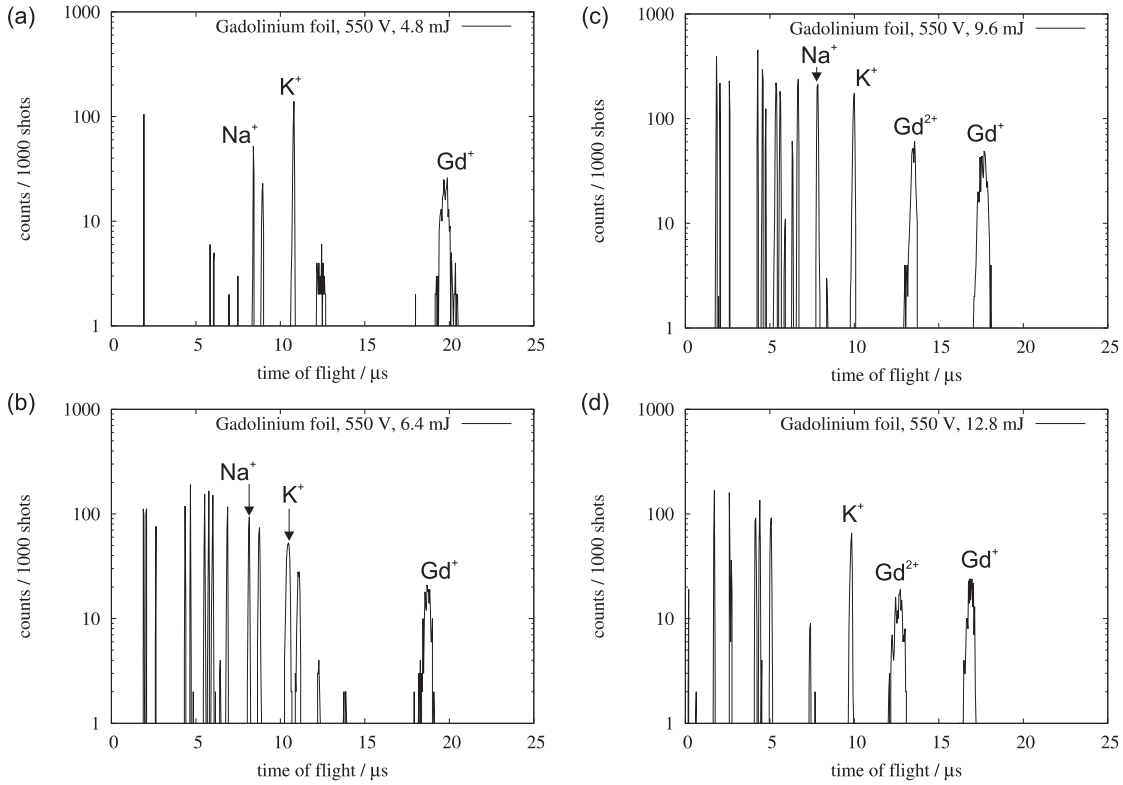

Figure 6.12: Time-of-flight distributions from a gadolinium foil at a target voltage of 550 V for with different laser pulse energies W. The used laser pulse energies W (energy densities ρ) are 4.8 mJ (0.43 J/cm^2) in (a), 6.4 mJ (0.57 J/cm^2) in (b), 9.6 mJ (0.85 J/cm^2) in (c), and 12.8 mJ (1.13 J/cm^2) in (d). The observed maxima are listed in Tab. 6.3 (see also text for discussion).

mJ is in case of the Gd^+ ions 250 eV. In addition to the kinetic energy expected from the acceleration voltage up to 400 eV kinetic energy is observed.

- The additional kinetic energy due to the laser pulse energy seems to increase with the ions mass-to-charge ratio m/q, thus lighter ions have on average less kinetic energy than heavier ions. Even at 1.9 mJ pulse energy a difference of more than 100 eV is observed between the gadolinium and sodium or potassium ions.

It is known that lasers with very high power densities of $\approx 10^{15}$ W/cm^2 accelerate ions up to 38-40 keV per charge state, which finds application for laser ion sources for accelerators [Zha99]. Due to this fact the identification of ions becomes difficult. The power densities used here are $\approx 10^{10}$, and the observed kinetic energy from the laser is 3 orders of magnitude less, but not negligible compared to the acceleration voltage. The identification should be carried out at low pulse energies, where the acceleration of the ions is negligible, which is on the other hand not always possible since a minimum laser pulse energy is required for ablation and ionisation. At higher laser pulse energies the simulated mass values cannot be used as a reference for the identification of the spectra (see Tab. 6.3). The ions are empirically identified by decreasing the laser pulse energy, observing the shift of the peaks, and comparing

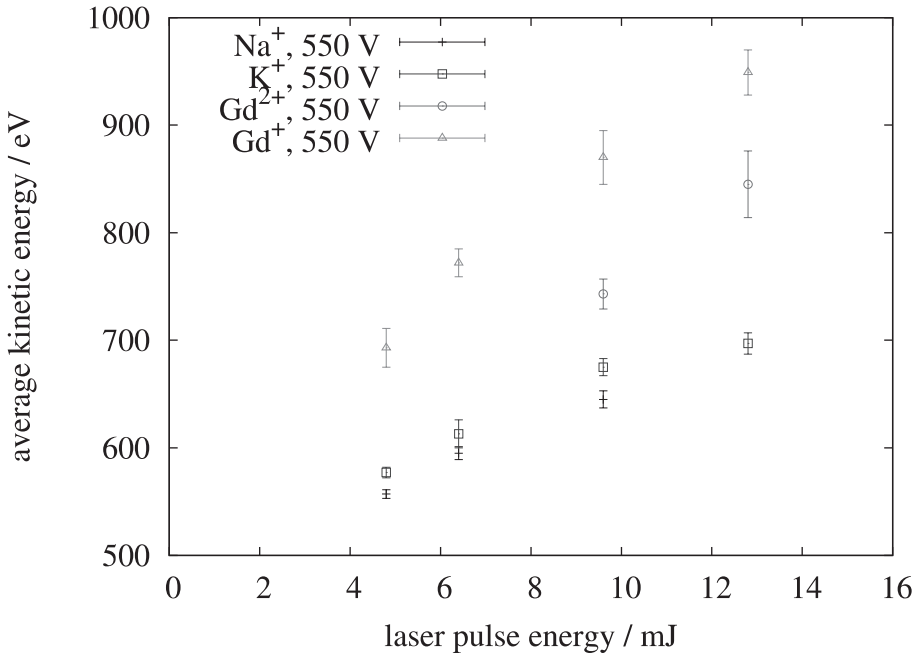

Figure 6.13: Average kinetic enengy as function of the laser pulse energy. E_{kin} = 550 eV is due to the acceleration voltage, up to 400 eV additional kinetic energy is observed for Gd^+ ions at 12.8 mJ laser pulse energy.

them finally to a simulated spectrum at lower pulse energies. The energy distribution of the ions has not been measured yet. This is for example possible by using the 90° bender to select, bend and detect ions with a certain kinetic energy on the main beam line. But considering this, the trap injection of a certain ion species becomes more difficult, since the bending voltages have to be adapted for each mass and laser pulse energy configuration.

Investigations concerning the velocity distribution of laser ablated gadolinium ions have been carried out by J. Maul [Mau05]. The velocity distribution consists of a thermal phase and a shockwave-driven phase. For an energy density[3] of 0.18 W/cm^2 the thermal phase has a temperature of $T \approx 2850$ corresponding to 0.3 eV average kinetic energy and the shockwave-driven phase has a maximum of already 21 eV kinetic energy. In all measurements performed with the gadolinium foil a much larger kinetic energy is observed, but when comparing these results to the investigations in [Mau05] the following differences have to be considered: (i) a laser with a different wavelength was in use (λ = 532 nm), and (ii) much higher energy densities were in use (from 0.43 J/cm^2 to 1.17 J/cm^2 compared to 0.17 J/cm^2 in [Mau05]). In case of one measurement with a similar energy density (see Tab. 6.3) an additional kinetic energy of 22 eV - 33 eV was observed, which is in good agreement to the observed kinetic energy of the shockwave front in [Mau05].

Further investigations were performed at higher acceleration voltages and lower laser pulse energies in order to minimise the influence of the laser on the time of flight. The obtained time-of-flight distributions corrensponding to the lower part

[3] A frequency-tripled Nd:YAG laser (λ = 355 nm) with a pulse width of 4 ns and a diameter of $\approx$ 20 μm was in use for these measurements.

Ion	m/q in u / e	τ in μs	$(m/q)_{sim}$ in u / e	E_{kin} in eV	W in mJ	ρ in J / cm^2
Na^+	23.0	8.41 ± 0.03	24.4 ± 0.2	557 ± 4	4.8	0.43
K^+	39.1	10.79 ± 0.05	40.1 ± 0.3	577 ± 5	4.8	0.43
Gd^+	157.3	19.73 ± 0.26	134.1 ± 3.5	693 ± 18	4.8	0.43
Na^+	23.0	8.14 ± 0.04	22.8 ± 0.2	595 ± 6	6.4	0.57
K^+	39.1	10.46 ± 0.11	37.7 ± 0.8	613 ± 13	6.4	0.57
Gd^+	157.3	18.70 ± 0.16	120.4 ± 2.1	772 ± 13	6.4	0.57
Na^+	23.0	7.82 ± 0.05	21.1 ± 0.3	645 ± 8	9.6	0.85
K^+	39.1	9.97 ± 0.06	34.2 ± 0.4	675 ± 8	9.6	0.85
Gd^{2+}	78.6	13.47 ± 0.13	62.5 ± 1.2	743 ± 14	9.6	0.85
Gd^+	157.3	17.61 ± 0.25	106.8 ± 3.0	870 ± 25	9.6	0.85
Na^+	23.0	7.38 ± 0.02	21.1 ± 0.3	645 ± 8	12.8	1.13
K^+	39.1	9.81 ± 0.07	33.1 ± 0.5	697 ± 10	12.8	1.13
Gd^{2+}	78.6	12.63 ± 0.23	55.0 ± 2.0	845 ± 31	12.8	1.13
Gd^+	157.3	16.86 ± 0.19	97.9 ± 2.3	949 ± 21	12.8	1.13
Gd^+	157.3	15.50 ± 0.07	161.4 ± 3.0	1123 ± 10	1.9	0.17
GdO^+	173.3	16.20 ± 0.06	176.3 ± 2.7	1133 ± 8	1.9	0.17
Na^+	23.0	6.08 ± 0.01	24.8 ± 0.2	1067 ± 4	2.8	0.25
K^+	39.1	7.84 ± 0.01	41.3 ± 0.2	1091 ± 3	2.8	0.25
Gd^+	157.3	15.32 ± 0.08	157.7 ± 3.2	1149 ± 12	2.8	0.25
GdO^+	173.3	16.09 ± 0.05	174.0 ± 2.0	1148 ± 7	2.8	0.25
Na^+	23.0	5.96 ± 0.01	23.9 ± 0.2	1111 ± 4	4.8	0.43
K^+	39.1	7.64 ± 0.01	39.2 ± 0.2	1149 ± 3	4.8	0.43
Gd^+	157.3	14.49 ± 0.07	141.2 ± 2.8	1285 ± 12	4.8	0.43

Table 6.3: Measured time-of-flight values τ of ions from a gadolinium foil for different laser pulse energies. The 1/e width of the time-of-flight distribution is used as uncertainty of τ. The upper part of the table are the identified ions from the measurements shown in Fig. 6.12 with a target voltage of 550 V, the lower part are the identified ions in the measurements shown in Fig. 6.14 with a target voltage of 1100 V. The assumed ion species with the expected m/q value, the mass-to-charge ratio obtained from the simulation fit function m_{sim}/q, the average kinetic energy E_{kin} for the assumed mass value m, the laser pulse energy W, and the energy density ρ are listed.

of the listed maxima in Tab. 6.3 are shown in Fig. 6.14. Laser pulse energies from 1.9-4.8 mJ were used and 1100 V were applied to the target. Gadolinium ions Gd^+ and even more GdO^+ ions are observed at 0.17 J/cm^2. While increasing the laser pulse energy, the fraction of GdO^+ ions decreases, at 0.43 J/cm^2 pulse energy only Gd^+ ions remain. In case of the previous measurements, Gd^{2+} ions are observed as well above 0.8 J/cm^2 laser pulse energy. As contaminations on the sample Na^+ and K^+ ions were identified.

Since a desorption of Gd^+ or GdO^+ ions with the laser ion source is possible, gadolinium ions or ions of gadolinium compounds are expected to be observed as well from targets made by deposition or molecular plating (see Sect. 6.1). Concerning

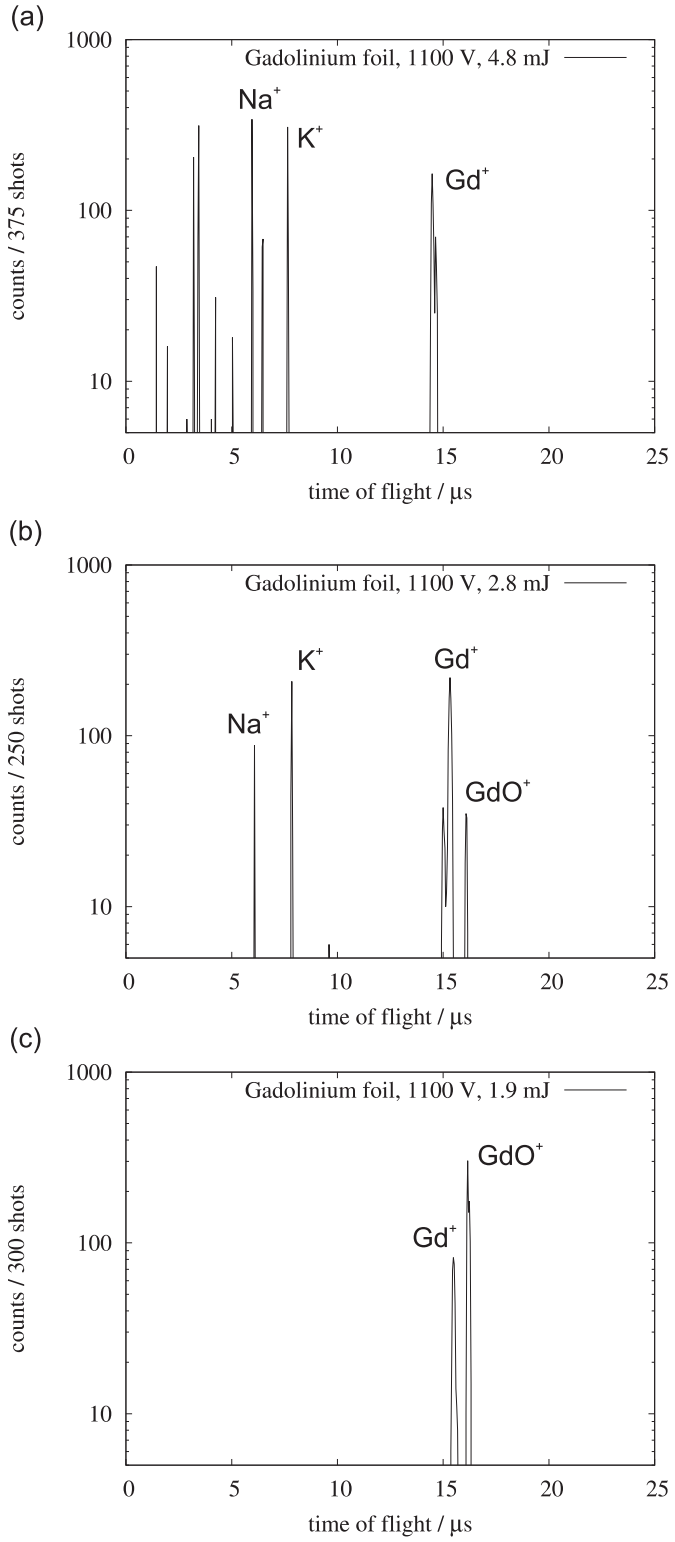

Figure 6.14: In (a)-(c) the obtained time-of-flight distributions from a gadolinium foil with different laser pulse energies $W = 1.9$ mJ, 2.8 mJ, and 4.8 mJ and a target voltage of 1100 V are shown.

the mass determination of heavy nuclides, oxygen compounds of these elements are suited as well for a measurement, since the mass of oxygen is well known (see Tab. 2.1 [Aud03]).

Samples of a gadolinium solution deposited on a tungsten substrate

Since the tests of the gadolinium foil were carried out successfully, samples with 10^{17}, 10^{15}, 10^{13}, 10^{11} gadolinium atoms on a tungsten substrate were produced by deposition (see Chap. 6.1) and investigated in the test setup without the extention tube. In Fig. 6.15 the experimental results of all four samples with similar ion optics and laser settings are plotted and compared to the simulation results (see Sect. 5.2).

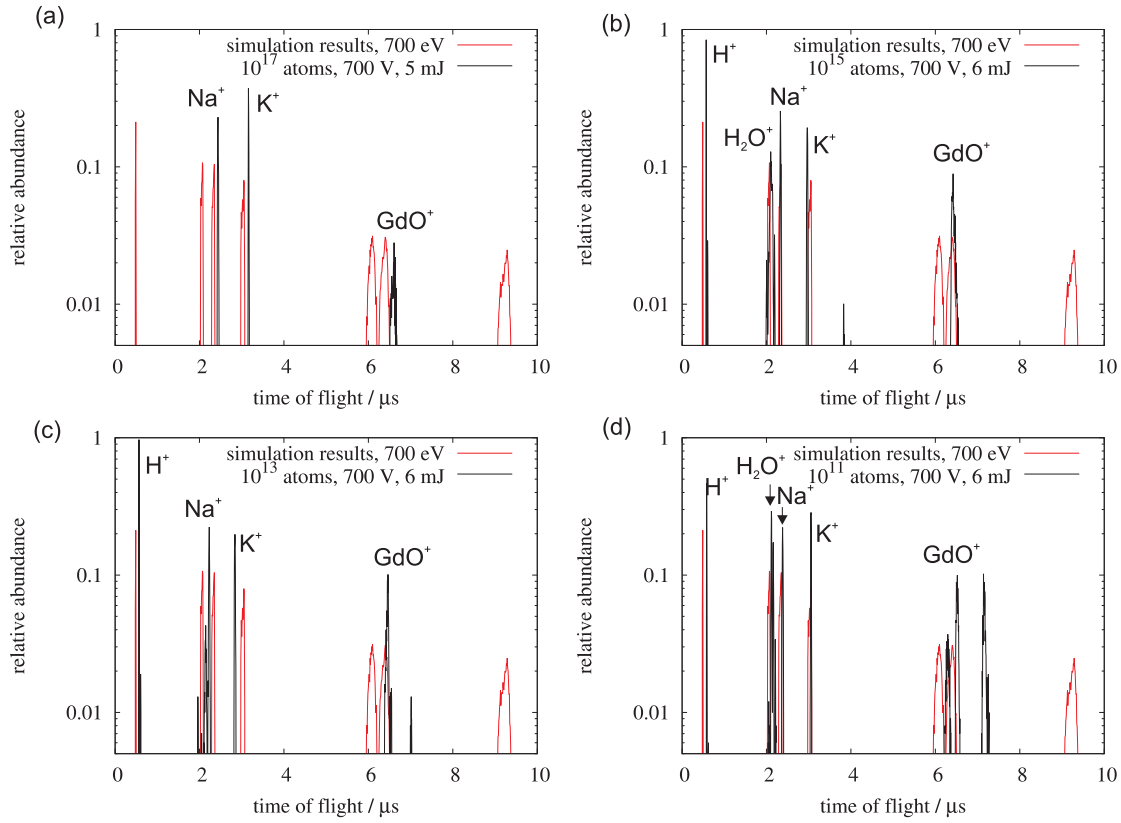

Figure 6.15: Time-of-flight spectra of samples with 10^{17}-10^{11} deposited gadolinium atoms. The experimental results in black are compared to a simulated spectrum in red. In the simulation H^+, H_2O^+, Na^+, K^+, Gd^+, GdO^+ and $Gd_2O_3^+$ are used (see Sect. 5.2). In all measurements a peak corresponding to GdO^+ is obtained. In case of the 10^{17} atoms sample, the abundance of the GdO^+ ions is lower since a lower laser pulse energy was used. In case of the 10^{11} atoms sample, two additional peaks are observed, since the MCA was operated with a lower dicriminator voltage.

The identifaction of the peaks was carried out by comparison to the simulated spectra. Slight deviations between the simulation and the measured time-of-flight distribution indicate, that the starting conditions of the ions did not exactly match

the experimental ones. A too low (or too high) initial kinetic energy results in a shift of all peaks to higher (or lower) time-of-flight values. Furthermore, the energy distribution of the ions was about a factor of 2 too large in the simulation, since the width of the simulated peaks is larger than of the experimental ones. Other reasons for the deviations between the expected and measured time-of-flight values are already discussed above. In all measurements peaks were observed, which were assigned to be Na^+, K^+, and GdO^+. In case of the 10^{17} atoms sample, a lower pulse energy was used. Therefore the abundance of the GdO^+ ions is lower, and H_2O^+ and H^+ ions are not observed compared to the other measurements. The latter are assumed to be created from fragmentation of H_2O molecules. In case of the gadolinium foil (compare Fig. 6.14), at power densities[4] of $\geq 0.5{\cdot}10^{11}$ W/cm^2 only gadolinium ions are observed. For the deposited samples larger power densities, $2{\cdot}10^{11}$ W/cm^2, have been used. Thus, Gd^+ ions are expected instead of GdO^+ ions. The target material, escpecially its reflectivity, has to be taken into account as well, when the laser energy transfered to the Gd atoms is considered. This may differ dramatically between tungsten and the gadolinium foil, leading to different results than expected from the measurements above.

Concerning the abundance of GdO^+ of the samples with different numbers of atoms, a decrease of the GdO^+ is not observed for samples with less gadolinium atoms. Due to the dead time of the channeltron detector in use, the absolute number of observed ions is not accessible. All ions of the same species are arriving within a very small time period (about 100 to 200 ns) at the channeltron detector, so that the detector is saturated. An indication that less ions are extracted is that the amplitude of the GdO^+ peak decreased for samples with less gadolinium atoms. In case of the 10^{11} atoms sample the discriminator threshold had to be lowered, since the signal corresponding to GdO^+ in the other measurements was below the discriminator threshold. Therefore two more signals are observed, which may correspond to Gd^+ and an ion with a mass of 207 - 217 u.

In order to know which kind of ions are coming from the tungsten subtrate and which kind of ions are coming from the gadolinium solution a pure tungsten subtrate was used as blank sample. The time-of-flight spectra with different laser pulse energies were recorded. For laser pulse energies ≤ 6 mJ almost no ion signals were observed with the channeltron detector. For 7 mJ and 8 mJ the obtained time-of-flight spectra are shown in Fig. 6.16. In both cases a peak at 0.8 μs is observed, but in case of the 7 mJ laser pulse energy the counts in the period from 5 to 7 μs where the gadolinium atoms or compounds are expected are negligible. For 8 mJ laser pulse energy a wide peak corresponding to mass values[5] from 170 to 275 u is observed, which is probably partly caused by tungsten ions, but too wide to be caused by just one ion species. Since all measurements with the deposited gadolinium samples have been performed at pulse energies below 6 mJ, the conclusion is that no signals caused by laser ablation of the tungsten substrate contribute to the obtained

[4]The power densities are compared here instead of laser pulse energies, because for both measurements different lenses (f = 45 cm and f = 85 cm) were in use, resulting in a different diameter of the focus (see Sect. 3.3).

[5]These values are obtained by calcations with the fit function from simulations. The edges of the wide peak have been used to estimate the mass range.

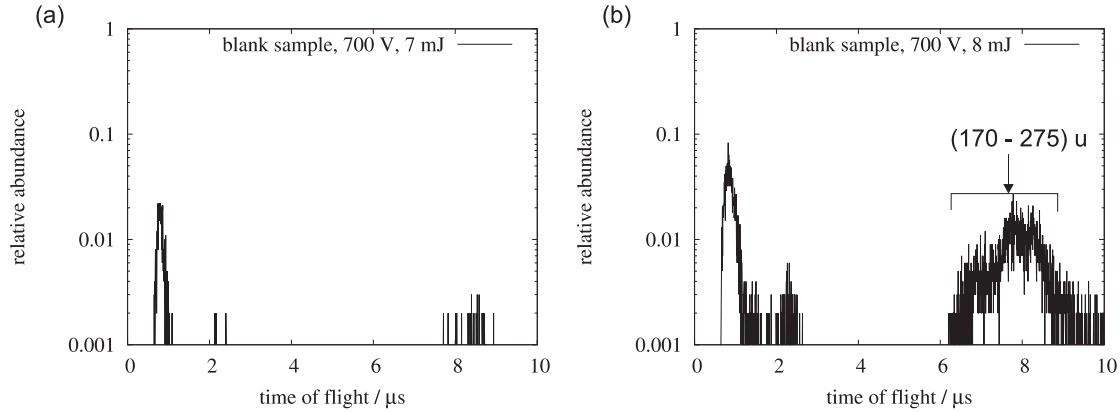

Figure 6.16: Signals observed with a blank tungsten substrate as target. Different laser pulse energies from 6 mJ up to 8 mJ were used. In case of 6 mJ no signals were observed, the measurement of 7 mJ and 8 mJ are shown in (a) and (b). 700 V were applied to the target holder threshold.

time-of-flight distributions.

Further tests have been performed where the gadolinium samples were rotated with the rotary feedthrough. Since the spot with the gadolinium has only a diameter of about 3 mm and is placed off-center, the the area covered with gadolinium can be moved out of laser spot. In that case no ion signals are expected to be observed at laser pulse energies below 7 mJ. Since the target is not visible during the test, multiple positions have been tested for each sample. The results of four different positions on sample with 10^{11} atoms are presented in Fig. 6.17.

In the case of the measurements shown in Fig. 6.17(a) and Fig. 6.17(b) the gadolinium spot was hit, only the yield of ions is slightly different. In case of the third position (see Fig. 6.17(c)), a clean spot was hit, where no ion signals are observed similar to the blank sample below 7 mJ pulse energy. The last investigated spot shown in Fig. 6.17(d) was contaminated. Ions identified as H^+, H_2O^+, Na^+ and K^+ were observed, but no gadolinium was observed at that position. Thus, the maximum in the time-of-flight spectrum, which was identified as GdO^+ is not related to ions from the tungsten plate[6] which could be misinterpreted to be GdO^+ due to the uncertainties in the mass determination.

Thus, to confirm that the produced ions are really gadolinium or gadolinium compounds, further tests are necessary. Since the ion identification in the test setup is limited due to the small flight length and the uncertainty in the initial kinetic energy, the best choice is to move the laser ion source to the TRIGA-TRAP setup and to proceed there with further tests. By trapping and measuring the cyclotron frequency of the ions a doubtless identification of the extracted ions is possible.

Concerning the ion production, the tests performed so far lead to the following results:

- Carbon cluster ions C_n^+ can be produced up to $n = 15$ from a Sigradur sample, and up to $n = 23$ from a C_{60} pellet, which is sufficient to provide reference ions for mass measurements on heavy nuclides.

[6] e.g. W^+ with an average mass of 183.8 u

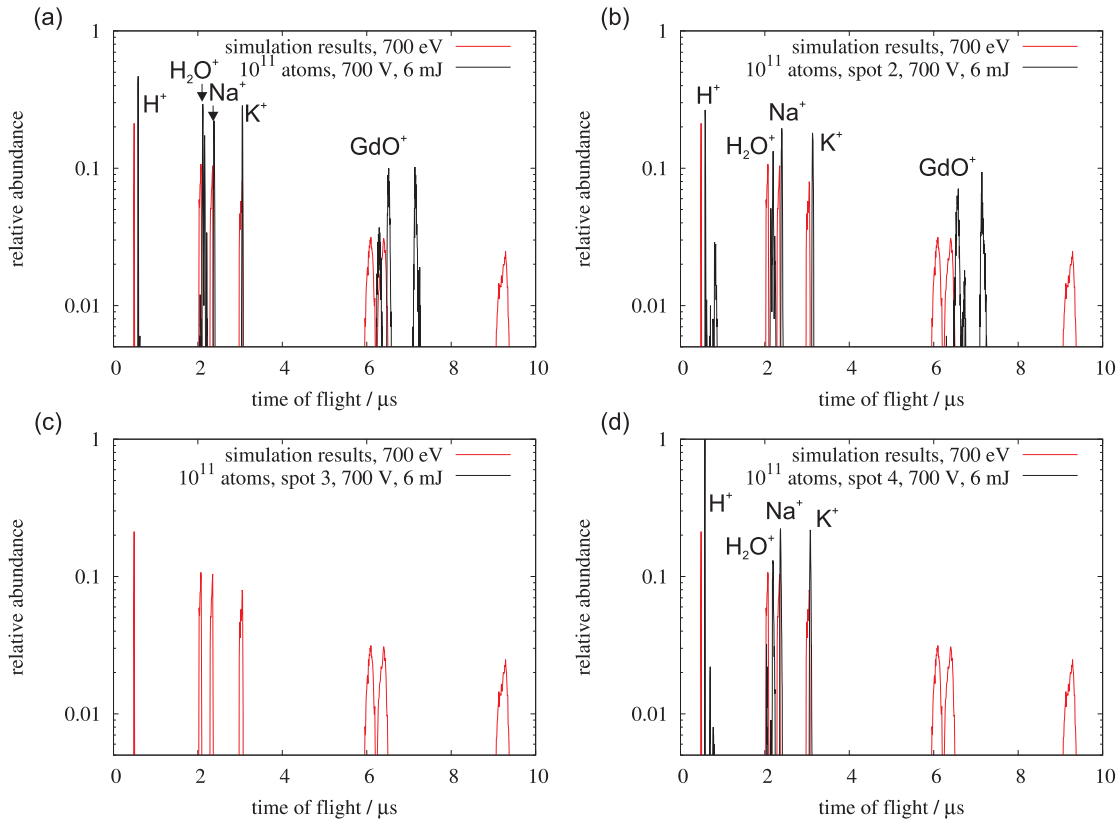

Figure 6.17: Time-of-flight distribution for 4 different positions on the target with 10^{11} gadolinium atoms. In the case of (a) and (b) the spot where the gadolinium solution was deposited was hit. For the measurement shown in (c) the gadolinium spot was missed and no ions are observed, as expected from the blank sample. In (d) the spot was also missed, but some contaminations on the surface were ablated by the laser.

- Gadolinium ions can be produced in large amounts by laser ablation with the developed ion source. Due to the similar chemical properties of the transuranium elements, an ionisation of these elements should be possible as well.

- The laser ion source is suited for the ionisation of the heavy nuclides from samples with only 10^{11} atoms, in case the ion identification is correct. Targets with a lower number of target atoms of the nuclide of interest may even be possible, since the detection limit was not yet reached.

Chapter 7

Conclusions and Outlook

For high-precision mass spectrometry in Penning traps, ions with well-known mass serve for the calibration of the magnetic field. Since the atomic mass unit is defined as 1/12 of the mass of the nuclide ^{12}C, carbon atoms or clusters are the ideal reference masses to perform absoulte mass measurements. Moreover, they provide a mass comb over the complete nuclear chart, which is especially important for mass measurements on heavy ions at TRIGA-TRAP. For the production of carbon clusters as well as heavy ions from uranium to californium, a laser ion source has been developed, assembled and characterised within this work. The production of carbon cluster ions has been demostrated with the source in a test setup, where the extracted ions were identified. Clusters C_n were observed with atom numbers $1 \leq n \leq 15$ using a Sigradur[1] sample, and $1 \leq n \leq 23$ as well as fullerene-like clusters with $n \geq 50$ using a C_{60}[2] sample. Since reference ions up 276 atomic mass units can be generated by C_{60}, all nuclides of interest for mass measurements with TRIGA-TRAP, which are nuclides up to ^{252}Cf, can be supplied with the ideal calibration mass.

For both sample materials, it should be possible to obtain clusters C_n with higher atom numbers n, as demonstrated in previous measurements [Bla02, Bla03a]. In case of the the Sigradur sample, clusters up to C_{23} were observed in these references. To increase the cluster size further tests can be performed, e.g. using a smaller diameter of the laser spot to increase the power density on the sample. In case of the C_{60} sample a higher mass resolution than obtained in the test setup is required to observe a separation of neighbouring clusters C_n with $n > 23$. Therefore, the next step is to attach the laser ion source to the TRIGA-TRAP setup, where a precision mass measurement of the clusters can be performed by determining the cyclotron frequency of the ions in the Penning traps. A direct comparison to the alkali ions with well-known mass can be used there for the identification of the produced cluster sizes.

Further applications for the carbon cluster ions are the possibility to study systematic uncertainties of TRIGA-TRAP in the mass determination, since the cyclotron frequency ratio of two clusters to each other is exactly known. By carbon cluster cross-reference measurements, where a carbon cluster ion C_m^+ is used as the

[1] Sigradur is a trade name of the HTW Hochtemperatur-Werkstoffe GmbH.

[2] C_{60} is also known as the Buckminsterfullerene.

reference ion for the mass determination of a second cluster C_n^+, these systematic uncertainties can be revealed, as demonstrated at ISOLTRAP [Bla02] and SHIPTRAP [Cha07].

For mass measurements on nuclides with a low production rate, it is necessary to have a good transport efficiency from the ion source to the Penning traps, to have as many ions as possible available for the measurement. Therefore, a simulation with the SimIon simulation code was carried out, in order to optimise the voltages of the transport electrodes and to understand the corresponding ion trajectories. The part of the TRIGA-TRAP setup which was included in the simulation has already 62 electrodes[3] for the ion transport and is therefore challenging to optimise. Assuming perfect alignment, optimal voltages for the ion optics were obtained, and studies concerning the transport efficiency and alignment errors, which have to be considered experimentally, were carried out. A transport efficiency from the surface ion source to the particle detector of 5%-14% can be reached in case of a perfect alignment. Alignment errors can be corrected using the stearing and bending elements in the beam optics, but the transport efficiency of the ideal case cannot be reached anymore.

TRIGA-TRAP also requires ionisation of the heavy elements from uranium to californium. For off-line tests, stable gadolinium isotopes were used as a sample material due to the similar chemical properties of the elements of interest. First, it was demonstrated that gadolinium ions can be generated with the laser ion source by using a gadolinium foil as sample. However, the most challenging part is the small number of atoms on the available samples, in the range of 10^{12} down to 10^8 atoms. Test were performed concerning the gadolinium ion production with different numbers of atoms on the samples. Atom numbers down to 10^{11} have been tested, and signals identified as GdO^+ were observed in all cases. To confirm that the identification is correct, further tests with a higher mass resolution are necessary, e.g. a mass measurement in a Penning trap. The next steps concerning the ion production of the heavy nuclides consist of:

- A clear identification of the ablated ion species will be performed by measuring the cyclotron frequency of the ions after installing the laser ion source in the TRIGA-TRAP setup.

- The lowest number of gadolinium atoms on a sample required for a reliable ion production has to be determined in order to save the heavy element material.

- Tests concerning the operation time, the ablation and ionisation efficiency have to be performed with different laser and target properties as well. The fraction of atoms available for trapping and the number of ion pulses should be as high as possible.

- Different substrate materials have to be tested. In the ideal case, the heavy ions can be generated from the surface of a Sigradur plate, thereby providing

[3]The transport electrodes for the trap injection for ions from the carbon cluster ion source, the correction electrodes and segments of the trap electrodes are not included in the simulation. If all trap electrodes are considered, the overall number of electrodes is already 78.

the ions of interest and the reference ions from the same sample simultaneously. Samples of these kind are in preparation at the Nuclear Chemistry Departement at the University Mainz.

Bibliography

[ABB01] ABB Automation Inc.: Axial Molecular Beam Ionizer Manual, 2001.

[Ada72] A. Adams *et al.*: Electrostatic cylinder lenses II: Three element einzel lenses, *J. Phys. E*, 5:150, 1972.

[And62] P.W. Anderson: Theory of flux creep in hard superconductors *Phys. Rev. Lett., 9:309, 1962*

[And64] P.W. Anderson *et al.*: Hard superconductivity - theory of motion of abrikosov flux lines *Rev. Mod. Phys., 36:39, 1964*

[Alt86] G.D. Alton: Semiempirical mathematical relationships for electropositive adsorbate work function changes, *Surf. Sci.*, 175:226, 1986.

[Alt93] G.D. Alton: Ion sources for accelerators in materials reaseach, *Nucl. Instr. Meth. B*, 73:221, 1993.

[Aud03] G. Audi *et al.*: The AME2003 atomic mass evaluation, *Nucl. Phys. A*, 729:337, 2003.

[Bec04] D. Beck *et al.*: A new controlsystem for ISOLTRAP, *Nucl. Instr. Meth. A*, 527:567, 2004.

[Ber02] I. Bergström *et al.*: SMILETRAP - a Penning trap facility for precision mass measurements using highly charged ions, *Nucl. Inst. Meth. A*, 487:618, 2002.

[Bla02] K. Blaum *et al.*: Carbon clusters for absolute mass measurements at ISOLTRAP, *Eur. Phys. J. A*, 15:245, 2002.

[Bla03a] K. Blaum *et al.*: Cluster calibration in mass spectrometry: laser desorption/ionisation studies of atomic clusters and application in mass spectrometry, *Anal. Bioanal. Chem.*, 377:1133, 2003.

[Bla03b] K. Blaum *et al.*: Recent developements at ISOLTRAP: towards a relative mass accuracy of exotic nuclei below 10^{-8}, *J. Phys. B*, 36:921, 2003.

[Bla05] K. Blaum *et al.*: ISOLTRAP pins down masses of exotic nuclides, *J. Phys. B*, 36:921, 2005.

[Bla06] K. Blaum: High-accuracy mass spectrometry with stored ions, *Phys. Rep.*, 425:1, 2006.

[Bol90] G. Bollen *et al.*: The accuracy of heavy-ion mass measurements using time of flight-ion cyclotron resonance in a Penning trap, *J. Appl. Phys.*, 68:4355, 1990.

[Bol01] G. Bollen: Mass measurements of short-lived nuclides with ion traps, *Nucl. Phys. A*, 693:3, 2001.

[Bro82] L.S. Brown and G. Gabrielse: Precision spectroscopy of a charged particle in an imperfect Penning trap, *Phys. Rev. Lett. A*, 25:2423, 1982.

[Bro86] L.S. Brown and G. Gabrielse: Geonium theory: Physics of a single electron or ion in a Penning trap, *Rev. Mod. Phys.*, 58:233, 1986.

[Bur07] Burle Industries, Inc.: Channeltron electron multiplier handbook for mass spectrometry applications, http://www.burle.com, 2007.

[Cha07] A. Chaudhuri *et al.*: Carbon-cluster mass calibration at SHIPTRAP, *Eur. Phys. J. D*, 45:47, 2007.

[Dah00] D.A. Dahl: SimIon for the personal computer in reflection, *Int. J. Mass Spectr.*, 200:3, 2000.

[Dah07] D.A. Dahl: SimIon 3D version 8.0 user's manual, 2007.

[Deh90] H. Dehmelt: Experiments with an isolated subatomic particle at rest, *Rev. Mod. Phys.*, 62:525, 1990.

[Ebe04] K. Eberhardt *et al.*: Preparation of targets by electrodeposition for heavy element studies, *Nucl. Inst. Meth. A*, 521:208, 2004.

[Eit07] G. Eitel: *Aufbau eines ortsauflösenden Ionennachweisdetektors für Penningfallenmassenspektrometie*, diploma thesis, Johannes-Gutenberg Universität Mainz, 2007.

[Emi95] C. Emiliani: Redefinition of atomic mass unit, Avogadro constant, and mole, *Geochimica et Cosmochimica Acta*, 59:1205, 2007.

[Fer07] R. Ferrer: *Mass measurements on neutron-deficient nuclides at SHIPTRAP and commissioning of a cryogenic narrow-band FT-ICR mass spectrometer*, PhD thesis, Johannes-Gutenberg Universität Mainz, 2007.

[Geo07] S. George: *Private Communications*, 2007.

[Gho95] P.K. Ghosh: *Ion Traps*, Oxford University Press Inc., New York, 1995.

[Gra80] G. Graeff: A direct determination of the proton electron mass ratio, *Z. Phys. A*, 297:35, 1980.

[Her03] F. Herfurth *et al.*: Mass measurements and nuclear physics - recent results from ISOLTRAP, *J. Phys. B*, 36:931, 2003.

[Kel03] A. Kellerbauer *et al.*: From direct to absolute mass measurements: A study of the accuracy of ISOLTRAP, *Eur. Phys. J. D*, 22:53, 2003.

[Kel04] R. Kelly *et al.*: Laser assisted plasma spectrochemistry: Laser ablation, *J. Anal. At. Spectrom.*, 19:374, 2004.

[Ket06] J. Ketelaer: *Development of a non destructive Fourier Transformation-Ion Cyclotron Resonance detection system for singly charged ions in a cyrogenic trap*, diploma thesis, Johannes-Gutenberg Universität Mainz, 2006.

[Ket09] J. Ketelaer: High-precision mass measurements with the Fourier Transform-Ion Cyclotron Resonance technique at TRIGA-TRAP, PhD thesis, Johannes-Gutenberg Universität Mainz, 2009.

[Kir90] R. Kirchner: On thermoionisation in hot cavities, *Nucl. Instr. Meth. A*, 292:203, 1990.

[Koe95] M. Koenig *et al.*: Quadrupole excitation of stored ion motion at the true cyclotron frequency, *Int. J. Mass Spectr.*, 142:95, 1995.

[Koe02] U. Koester: Resonance ionization laser ion sources, *Nucl. Phys. A*, 701:441c, 2002.

[Kug00] E. Kugler: The ISOLDE facility, *Hyperfine Interactions*, 129:23, 2000.

[Lan25] I. Langmuir and K.H. Kingdon: Thermionic effects caused by vapours of alkali metals, *Proceedings of the Royal Society of London A*, 107:61, 1925.

[Lás96] L. Láska *et al.*: Multiply charged ion generation from NIR and visible laser-produced plasma, *Rev. Sci. Instr.*, 67:950, 1996.

[Mag03] Magnex Scientific: 7.0T/160/AS Ion Trap Magnet System, System Manual, 2003.

[Mau04] J. Maul: *Ortsaufgelöster Nachweis von Elementspuren mittels Laserablation und Resonanzionisations-Massenspektrometrie und Untersuchungen zur Laserablations-Dynamik*, PhD thesis, Johannes-Gutenberg Universität Mainz, 2004.

[Mau05] J. Maul *et al.*: Bimodal velocity distribution of atoms released from nanosecond ultraviolet laser ablation, *Phys. Rev. B*, 71:045428, 2005.

[McD72] E.W. McDaniel and M.R.C. McDowell: *Case Studies in Atomic Physics II*, North Holland, Amsterdam, 1972.

[Mró96] W. Mróz *et al.*: Thomson parabola ion spectrograph with the microchannel plate image converter in investigations of high-z laser plasma ion sources, *Rev. Sci. Instr.*, 67:1272, 1996.

[Muk07] M. Mukherjee *et al*: ISOLTRAP: An on-line Penning trap for mass spectrometry on short-lived nuclides, *Eur. Phys. J. D*, submitted, 2007.

[Nat07] National Nuclear Data Center, Brookhaven National Laboratory: http://www.nndc.bnl.gov, 2007.

[Nei06] D. Neidherr: *Entwicklung einer Pumpsperre für das Penning-Falle-Massenspektrometer SHIPTRAP*, diploma thesis, Johannes-Gutenberg Universität Mainz, 2006.

[Nei07] D. Neidherr *et al.*: Measurements and simulation of the pressure ratio between two traps of double Penning trap mass spectrometers, *Nucl. Instr. Meth. B, submitted*, 2007.

[NIS06] National Institute of Standards and Technology: CODATA value: atomic mass unit, *http://physics.nist.gov*, 2006.

[Ohs06] S. Ohshima *et al*: Development of zeolite ion source for beam probe measurements of high temperature plasma, *Rev. of Sci. Instr.*, 77:03B704, 2006.

[Par62] W. Parker *et al.*: Molecular Plating - a method for the electrolytic formation of thin inorganic films *Nucl. Inst. Meth.*, 16:355, 1962.

[Pau90] W. Paul: Electromagnetic traps for charged and neutral particles, *Rev. Mod. Phys.*, 62:531, 1990.

[Pen36] F.M. Penning: Die Glimmentladung bei niedrigem Druck zwischen koaxialen Zylindern in einem axialen Magnetfeld, *Physica*, 3:873, 1936.

[Rah06] S. Rahaman *et al.*: On-line commissioning of SHIPTRAP, *Int. J. Mass Spectr.*, 251:146, 2006.

[Rai04] S. Rainville *et al.*: An ion balance for ultra-high-precision atomic mass measurements, *Science*, 303:334, 2004.

[Rep07] J. Repp: Aufbau eines Breitband-Fouriertransformation-Ionzyklotron-resonanz Nachweises für Präzisionsmassenmessungen, internal report, 2007.

[Sav91] G. Savard *et al.*: A new cooling technique for heavy ions in a Penning trap, *Phys. Lett. A*, 158:247, 1991.

[Sch91] L. Schweikhard: Theory of quadrupole detection Fourier transformation cyclotron-resonance *Int. J. Mass Spectr.*, 107:281, 1991.

[Shi05] W. Shi *et al.*: Atomic masses of S-32, S-33, Kr-84, Kr-86, and Xe-129, Xe-132 with uncertainties ≤ 0.1 ppb, *Phys. Rev. A*, 72:2, 2005.

[Sie86] A.E. Siegman: *Lasers*, University Science Books, Sausalito, Californien, 1986.

[Smi67] C.J. Smithells: *Metals Reference Book*, Butterwoths, London, 1967.

[Van04] R.S. Van Dyck *et al.*: Ultraprecise atomic mass measurement of the alpha particle and He-4, *Phys. Rev. Lett.*, 92:22, 2004.

[Ver03] J. Verdu: *Ultrapräzise Messung des elektronischen g-Faktors in wasserstoffähnlichem Sauerstoff*, PhD thesis, Johannes-Gutenberg Universität Mainz, 2003.

[Vál77] L. Vályi: *Atom and Ion Sources*, Wiley, London, 1977.

[Web04] C. Weber: *Konzeption eines kryogenen Penningfallenaufbaus für SHIPTRAP und Massenbestimmung von Radionukliden um den Z = 82 Schalenabschluss an ISOLTRAP*, PhD thesis, Ruprecht-Karls Universität Heidelberg, 2004.

[Wit92] H. Wituschek *et al.*: Investigation of extraction systems with low aberation, *Rev. Sci. Instr.*, 63:2785, 1992.

[Wri92] D. Wright *et al.*: Laser beam width, divergence and beam propagation factor - an international standardization approach, *Optical and Quantum Electronics*, 24:993, 1992.

[Wur94] P. Wurz and K.R. Lykke: Kinetics of multiphoton excitation and fragmentation of C_{60}, *Chem. Phys.*, 184:335, 1994.

[Yaz06] C. Yazidjian *et al.*: A new channeltron-detector setup for precision mass measurements at ISOLTRAP, *Hyperfine Interactions*, 173:181, 2006.

[Zha99] H. Zhang: *Ion Sources*, Science Press Beijing and Springer-Verlag Berlin, 1999.

Acknowlegements

The acknowledgements will be given in German.

Im letzten Jahr habe ich in der MATS AG unter der Leitung von Klaus Blaum diese Diplomarbeit angefertigt. Dabei bin ich von sehr vielen Leuten mit hilfreichen Diskussionen und handkräftigen Taten unterstützt worden.

An erster Stelle ist hier mein Betreuer Klaus Blaum zu nennen, der in Vorlesungen und während eines Praktikums mein Interesse für die Präzissionsmassenspektromentie geweckt hat, und mich bei physikalischen und organisatorischen Problemen stets unterstützt hat. Ohne ihn wäre diese Arbeit nicht möglich gewesen.

Weiterhin danke ich den Mitarbeitern an TRIGA-TRAP, Szilard Nagy, Rafael Ferrer Garcia, Sebastian George, Jens Ketelaer, Georg Eitel, Julia Repp, für ihre Hilfe im Labor, bei Messungen und Auswertungen.

Besonderer Dank gebührt auch der meachanischen Werkstatt am Institut für Physik. Hierbei sind Siegbert Felzer, Peter Becker, Heiko Lott, Wolfgang Wann und Matthias Eck hervorzuheben, die die Elektroden für die Laserionenquelle angefertigt haben, bei der Probenherstellung geholfen haben und immer in allen Notfällen ansprechbar waren.

Klaus Eberhardt, Petra Thörle-Pospiech und Dirk Liebe vom Institut für Kernchemie an der Universität Mainz danke ich für ihre Beratung und die Anfertigung der Gadoliniumproben.

Jochen Maul danke ich für hilfreiche Tipps und Diskussionen zur Ablation von Gadolinium, Birgit Schabinger für viele Einsätze zur späten Stunde, und den Arbeitsgruppen von Klaus Wendt, Jochen Walz und Wilfried Nörthershäuser für die geliehene Ausrüstung und ihre Unterstützung.

Außerdem danke ich den Mitgliedern der MATS AG: Susanne Kreim, Stefan Ulmer, Holger Kracke, Cricia de Carvalho Rodegheri, Sven Sturm, Anke Wagner, Marta Ubieto Diaz, Nikita Kotovsky, Dennis Neidherr und Michael Dworschak, und allen anderen, die mich während meines Studiums als Freunde und Kommilitonen begleitet haben.

Ganz besonders möchte ich mich bei meiner Familie bedanken, die mir das Studium der Physik möglich gemacht haben und mich in den vergangenen Jahren immer unterstützt hat.

Erklärung

Hiermit erkläre ich, dass ich die vorliegende Arbeit selbst verfasst habe und keine weiteren außer den angegebenen Quellen und Hilfsmittel verwendet habe.

Mainz, den 22.01.2008

Christian Smorra